UNIVERSITY OF CALIFORNIA,
IRVINE

Deep Brain Signal Transmission in Response to Exogenous Stimulation in Children with Dystonia

DISSERTATION

submitted in partial satisfaction of the requirements
for the degree of

DOCTOR OF PHILOSOPHY

in Biomedical Engineering

by

Jessica Sofie Louise Widmark Hillman

Dissertation Committee:
Professor Terence D. Sanger, Chair
Professor David J. Reinkensmeyer
Assistant Professor Autumn S. Ivy

2023

DEDICATION

To

my family, husband, and friends

for their support and patience,

and to

Becks: I'll have more time

to play with you soon.

An attempt at science

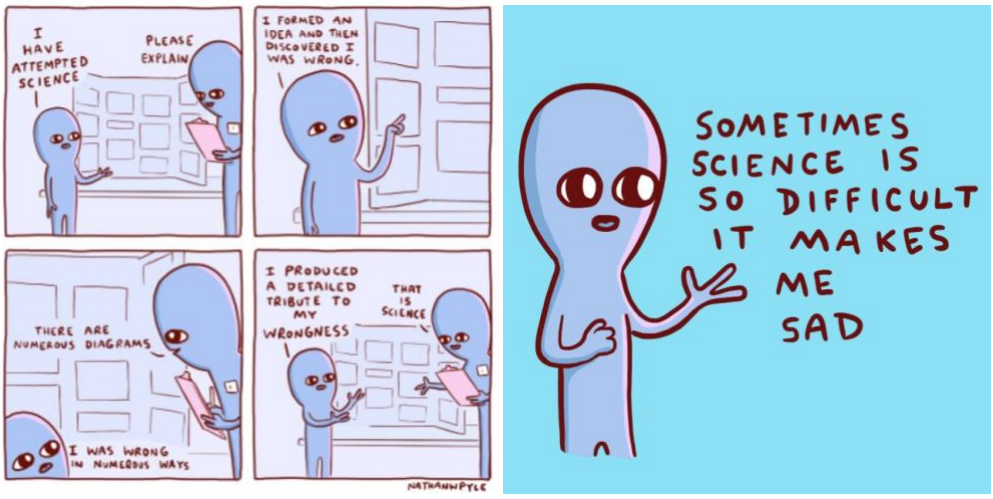

Nathan W. Pyle
Strange Planet

TABLE OF CONTENTS

LIST OF FIGURES

LIST OF TABLES

ABBREVIATIONS

AC	anterior commissure
ADPREP	automated detection of polarity reversed evoked potentials
BZD	benzodiazepine
CEDAM	complex exponential decay artifact model
CHLA	Children's Hospital Los Angeles
CHOC	Children's Health Orange County
CMP	centromedian parafascicular complex
CP	cerebral palsy
CT	computed tomography
DBS	deep brain stimulation
DTI	diffusion tensor imaging
DWI	diffusion-weighted imaging
EEG	electroencephalography
EMG	electromyography
EONR	evoked oscillatory neural response
EP	evoked potential
EPI	echo planar imaging
ET	essential tremor
FA	fractional anisotropy
FFT	fast Fourier transform
FOV	field of view

GoF	goodness of fit
GPe	globus pallidus externus
GPi	globus pallidus internus
HFEP	high-frequency evoked potential
HFO	high-frequency oscillation
ICA	independent component analysis
LFP	local field potential
MRI	magnetic resonance imaging
MWD	multilevel wavelet decomposition
NA	nucleus accumbens
NMU	neuromodulation monitoring unit
P2P	peak-to-peak amplitude
PC	posterior commissure
PD	Parkinson's disease
PPN	pedunculopontine nucleus
PSD	power spectral density
SEDAM	simple exponential decay artifact model
sEEG	stereo-electroencephalography
SNR	signal-to-noise ratio
STN	subthalamic nucleus
T2P	time-to-(first-)peak delay
UCI	University of California, Irvine
USC	University of Southern California

VA	ventral anterior nucleus
VFO	very fast oscillation
VIM	ventral intermediate nucleus
VO	ventral oralis (anterior/posterior) *[see below]*
Voa/Vop	ventral oralis anterior/posterior *[see above]*
VPL	ventral posterolateral nucleus

ACKNOWLEDGEMENTS

I would like to express my sincere appreciation to my committee chair and advisor, Professor Terence D. Sanger, for his ongoing support throughout my entire PhD. His advice was always invaluable, both within academics and in discussions about prospective careers, and I thank him for encouraging me to follow my own research interests among the many focuses made possible by our great bank of neurophysiological data. Without Dr. Sanger's brilliant guidance and generous funding, this PhD and dissertation would not have been possible.

I would also like to thank my dissertation and qualifying exam committee members, Prof. David J. Reinkensmeyer, Dr. Autumn S. Ivy, Prof. Beth A. Lopour, and Prof. Richard M. Leahy for their feedback on my preliminary results and research plans in 2021, which helped guide me and provide me with focus for the last year and a half of my PhD. I thank them for taking the time out of their busy schedules to provide their invaluable support and input during and between my qualifying exam and dissertation defense.

Thanks are also in order to my fellow lab members, current and past, including Dr. Estefanía Hernandez-Martin, Prof. Jonathan Realmuto, Dr. Alireza Mousavi, Enrique Argüelles, Ruta Deshpande, Dr. Sumiko Abe, Jennifer MacLean, Dr. Allison Przekop, Aprille Tongol, Jaya Nataraj, Maral Kasiri, Yun Sun, Rahil Soroushmojdehi, Sina Javadzadeh No, and Mehrnaz Asadi. My lab members have been vital to this dissertation in the gathering of data, assistance with neurological examinations, data analysis, brainstorming, feedback, and so much more. While our interactions around the surgery room were rare, I also greatly appreciate the efforts of Mark Liker and Joffre Olaya in the neurosurgical care of our subjects.

In addition to Dr. Sanger's generous financial support in taking me on as a Research Assistant and Graduate Student Researcher at the University of Southern California (USC) and University of California, Irvine (UCI), respectively, I would like to thank USC for granting me the Viterbi Fellowship during my first year as a PhD student; this allowed me to rotate in three separate labs and determine that the Sanger Lab was where I would academically thrive. Additionally, I thank the Sweden-America Foundation for granting me a fellowship for the 2021-22 academic year, allowing me to focus fully on the last years of my dissertation research.

Finally, I express my sincerest gratitude towards our subjects and their parents for participating in our studies and allowing us to use their data to advance research within the fields of movement disorders, deep brain stimulation, and human neurophysiology. Without your selfless contributions, this dissertation would – quite literally – not have been possible.

I thank you all sincerely.

VITA

Jessica Sofie Louise Widmark Hillman

2015	Moncrief Summer Research Intern, Institute for Computational Engineering and Sciences, University of Texas at Austin, TX
2016	Bachelor of Science in Electrical Engineering, Florida Institute of Technology, Melbourne, FL
2016-17	Patient Safety Assistant, Novartis, Stockholm, Sweden
2017-18	Biomedical Engineer, PSYONIC Inc., Champaign, IL
2018	Master of Science in Medical Engineering, KTH Royal Institute of Technology, Stockholm, Sweden
2019-23	Co-Founder & Biomedical Engineer, MedMxr Inc., Los Angeles, CA
2019-23	Graduate Student Researcher / Research Assistant, Sanger Lab, University of California, Irvine / University of Southern California, Los Angeles, CA
2022-23	Preclinical Research Engineer Intern, iota Biosciences, San Francisco, CA (Remote)
2023	Doctor of Philosophy in Biomedical Engineering, University of California, Irvine, CA

FIELD OF STUDY

Human Neurophysiology of Movement Disorders

PUBLICATIONS

J. S. L. Vidmark, E. Hernandez-Martin, and T. D. Sanger, "Increasing Consistency of Evoked Response in Thalamic Nuclei During Repetitive Burst Stimulation of Peripheral Nerve in Humans," in Medical Image Computing and Computer Assisted Intervention – MICCAI 2021, vol. 12908, M. de Bruijne, P. C. Cattin, S. Cotin, N. Padoy, S. Speidel, Y. Zheng, and C. Essert, Eds. Cham, Switzerland: Springer International Publishing, 2021, pp. 238–247.

J. Realmuto, J. S. L. Vidmark, and T. D. Sanger, "Modeling deep brain stimulation evoked responses with phase oscillator networks (accepted)," in IEEE EMBS International Conference on Neural Engineering (NER), 2023.

ABSTRACT OF THE DISSERTATION

Deep Brain Signal Transmission in Response to Exogenous Stimulation
in Children with Dystonia

by

Jessica Sofie Louise Widmark Hillman

Doctor of Philosophy in Biomedical Engineering

University of California, Irvine, 2023

Professor Terence D. Sanger, Chair

Dystonia is a movement disorder that causes involuntary twisting and repetitive movements, which can impede the patient so much that they are unable to lead independent lives or even communicate clearly with the people around them. In recent decades, exogenous electrical stimulation, including deep brain stimulation (DBS) and peripheral nerve stimulation (PNS), has shown promising results in the treatment of movement disorders caused by abnormal neural activity. However, as with any tool, exogenous electrical stimulation is only as useful as its operator is skilled, and for optimal use, the operator must both know *what* to do, and *how* to do so. By studying the abnormal signal flow that causes dystonia, we can understand *what* needs to be fixed, and by studying the effects of electrical stimulation on the dystonic brain, we can learn *how* to control the response pattern to generate the desired effect for each individual patient.

I aimed to contribute to these topics by studying neural recordings from stereo-electroencephalography (sEEG) electrodes in thalamic nuclei and basal ganglia of pediatric patients with dystonia during intracranial and peripheral electrical stimulation. My results were multifold, highlighting the complexity of the brain's response to exogenous stimulation.

I found that the initial transient neural response to exogenous stimulations differs from long-term steady state responses to constant stimulation, and that DBS evoked potentials (EPs) can be affected, in a highly heterogeneous way, by the intake of medications. I discovered novel, intricate, yet highly consistent EPs, and unearthed trends in how DBS EPs and their delay, amplitude, and even shape depends on the stimulation frequency. I helped generate models to describe the observed neural responses and even discover connections between invasive neurophysiological recordings and non-invasive imaging methods.

These results were made possible by my extensive work put into developing methods to accurately process the data, remove noise and artifacts, and automate processes wherever possible to reduce bias and save time for further analyses. Through these methods alone, I hope to have contributed to the field of engineering for an extended time to come.

While we may still just be scratching the surface, I am confident that my dissertation research has at least made a solid dent in the casing that holds the secret to using exogenous stimulation to elicit the optimal clinical effect for children with dystonia and other movement disorders.

INTRODUCTION

Cerebral palsy, the most common etiology of secondary (non-genetic) dystonia, is the most frequent motor disability among children, with an incidence of two (2) out of every 1,000 live births [1]. Dystonia is a disorder that causes involuntary twisting and repetitive movements [2] that impede these patients' lives to the extent that many are unable to walk on their own, feed themselves, or even communicate clearly. Although many studies have investigated the pathophysiology of dystonia [2]–[8], it is still unclear what in the brain gives rise to these symptoms, and medications to reduce them are not always effective.

When this is the case, an alternative method called deep brain stimulation (DBS) has proven clinically effective, not only for dystonia [6], [9]–[11], but also for other movement disorders [12]. This treatment method delivers electrical pulses to deep brain regions, where they are believed to modulate neural activity and help reduce the pathological activity causing the symptoms. Although DBS has been used for decades, and despite its clinical success, its mechanism of action remains largely unexplained [6]. Similarly, ambiguities exist regarding the mechanism of peripheral nerve stimulation (PNS), a method that electrically stimulates peripheral nerves through the skin and has been proposed as a noninvasive treatment [13] for dystonia [14]–[16] and other movement disorders [17]–[19]. This ambiguity, in combination with the difficulties determining the sources of the movement disorders to be treated, make it challenging to plan the ideal treatment for each patient. Hence, the aim of my research is to create a better understanding of signal flow in the dystonic brain and how it responds to electrical stimulation.

We use DBS and stereo-electroencephalography (sEEG) leads as a tool to not only stimulate, but also record the brain's response as it propagates throughout the brain. Through our

work with dystonic patients that have already been selected for DBS treatment, we gain valuable insight into the human brain directly, rather than through animal studies or computational models alone. Moreover, our innovative procedures provide us with unique opportunities to gather intracranial data from awake and unrestrained subjects over a span of days in our neuromodulation monitoring unit (NMU) – rather than minutes while the patient is temporarily awoken from anesthesia in the operating room, as is an otherwise common procedure [20]. This allows us to perform more and longer experimental protocols, providing insight into the brain's transient (initial) as well as steady state (longer term) responses to both intracranial and peripheral stimulations.

In order to extract useful information from the raw data, a fundamental process is data treatment. Because we have established a new approach that allows us to record and stimulate simultaneously, new signal processing tools needed to be developed, including artifact reduction, segment alignment, and modeling. These are topics that I have personally invested significant time into, to ensure that my final data interpretation is reliable.

While the main focus of this dissertation revolves around neural responses to electrical stimulation, recorded from intracranial sEEG leads, we simultaneously record other data including cortical electroencephalography (EEG) and muscular electromyography (EMG), and also obtain anatomical and functional images including computed tomography (CT), magnetic resonance imaging (MRI), and diffusion tensor imaging (DTI). This multi-approach project provides me with the opportunity to generate even deeper insights into the neurophysiological function of dystonia, through collaborations with my fellow lab members who analyze these experiments and data types.

In the current "golden standard" of DBS therapy, even after the most promising DBS implant location has been selected, tedious programming of the ideal stimulation settings awaits the patient and their neurologist in the weeks and months after surgery. These programming sessions are composed of lengthy trial-and-error testing of different combinations of stimulation contacts, frequencies, voltages, and pulse widths. Furthermore, while thalamic stimulation can lead to improvements in symptoms within minutes, difficulty arises in basal ganglia targets, as DBS in these nuclei may not show beneficial results for the first few weeks or even months of stimulation. [6]

My research aims to make this process of finding the ideal DBS targets and settings more straightforward, structured, and successful. In the future, it is possible that the ideal electrical stimulation treatment plan for each patient will be chosen by first determining what kind of neuromodulation one wants to achieve, and then selecting the stimulation settings that would achieve this desired result. However, in order to reach this ideal treatment approach, we must bridge the knowledge gaps of understanding (1) the mechanism and signal flow of the disorder to be treated and (2) how electrical stimulation modulates this signal flow [12]. While there is still a long way to go to bridge these gaps, my dissertation research has taken steps towards them – especially the latter – by developing improved and novel data processing tools, analytical methods, and models, and using these to gain insight into the dystonic brain and its response to exogenous stimulation. In this manner, my dissertation has the potential to provide significant contributions not only to the field of neuroscience, but also to engineering and medicine alike.

Chapter summaries

The chapters in this dissertation were structured in a natural progression, starting "from the outside" and "moving in", with Chapter 1 discussing the brain's response to bursting peripheral nerve stimulation and introducing an artifact removal method that allows for confident evoked potential (EP) detection. Chapter 2 continues inwards, presenting novel DBS EPs – with higher-frequency components than the "typical" DBS EP – that are only detectable when recording with high-impedance micro-contacts. Chapter 3 proceeds to outline an automated method to detect both these kinds of EPs, which makes use of polarity reversed stimulations and the artifact removal method presented in Chapter 1. The next two chapters investigate how these detected EPs are affected by not only stimulus frequency (Chapter 4), but also medications (Chapter 5). The final two chapters then present models to explain the mechanism that elicits oscillatory EPs in the basal ganglia (Chapter 6) and to relate DBS EPs with non-invasive imaging methods (Chapter 7).

These chapters all build on each other to take several very important steps towards our ultimate goal of developing non-invasive methods to predict the DBS parameters and locations that will elicit the most effective treatment possible for childhood dystonia.

Summary of Chapter 1: Novel decay artifact removal method reveals increasing consistency of thalamic response to repetitive peripheral nerve stimulation

Using a method that I developed to remove stimulus decay artifacts (Figure 1, top), I analyzed thalamic recordings of neural responses to electrical burst stimulation of the median nerve in 12 pediatric patients with dystonia. We found that the peripheral nerve burst stimulation induced increasing consistency of successive evoked responses in the thalamic nuclei for all burst frequencies (Figure 1, bottom), which we propose is due to progressive synchronization of small

populations of thalamic neurons, causing phase locking. Clinical efficacy could thus be due to "synchronization blockade", in which the synchronized response of the population prevents transmission of intrinsic abnormal signals due to tremor or dystonia. Such enhanced understanding will increase the potential for use of peripheral stimulation as a noninvasive alternative or adjunct to deep brain stimulation.

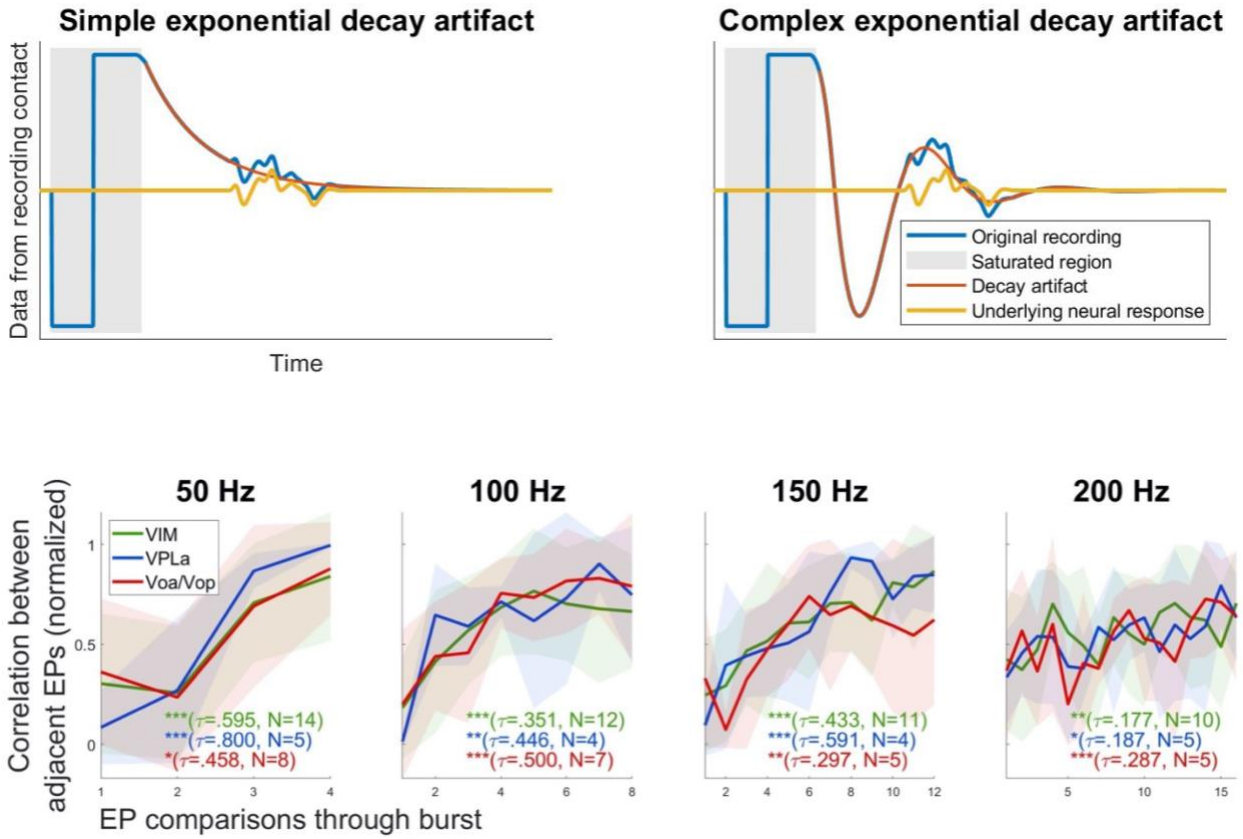

Figure 1. Summary figure for Chapter 1: Novel decay artifact removal method reveals increasing consistency of thalamic response to repetitive peripheral nerve stimulation. Top row: Simulated visualizations of the artifacts that my model can successfully remove: simple (left) and complex (right) exponential decay artifacts. Bottom row: Correlations between adjacent evoked potentials (EPs) increase with time during the stimulation bursts for each stimulus frequency and all studied thalamic nuclei. *See Figure* 1.1 *and Figure* 1.3 *for full figure descriptions.*

Summary of Chapter 2: Deep brain stimulation reveals high-precision temporal coding in basal ganglia and thalamus

Novel high-frequency evoked potentials (HFEPs) consisting of frequency components up to 6 kHz were detected in high-impedance contact recordings from thalamus and/or basal ganglia in all 11 dystonic subjects included in this study (Figure 2). These HFEPs (Figure 2B), which stand in stark contrast to the more common single-oscillation 1-2-kHz DBS EP (Figure 2A,D), are a sign of the complexity of the human brain's response to DBS, and may be the result of local resonant circuits or synchronization of multiple axons. Conventional low-impedance electrodes were unable to record these HFEPs (Figure 2C), which means that high-impedance electrodes are required to accurately probe the human brain's complex response to DBS.

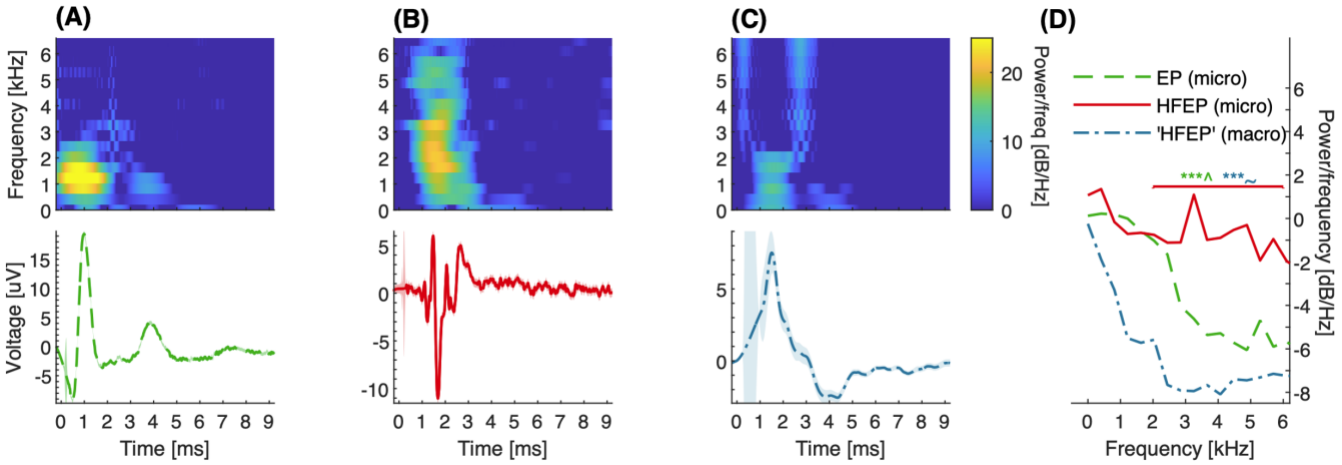

Figure 2. Summary figure for Chapter 2: Deep brain stimulation reveals high-precision temporal coding in basal ganglia and thalamus. Frequency analysis comparison of sample "regular" (A) vs. high-frequency EPs (B), both recorded from micro-contacts, and an equivalent "HFEP" recording from macro-contacts (C); bottom row: time-domain EP examples; top row: corresponding spectrograms. Corresponding PSDs (D) show the statistically higher power of the HFEP in the 2-6-kHz high-frequency band when compared to both the "regular" EP and the macro-contact recording. See Figure 2.2 for full figure description.

Summary of Chapter 3: An algorithm for automated detection of evoked potentials from polarity reversed electrical stimulation

I developed a novel algorithm for automated detection of polarity reversed EPs (ADPREP), which uses the knowledge that switching the polarity of a pair of stimulating contacts reverses the sign of the stimulus artifact, but not the sign of the neural response. This algorithm can distinguish EPs of varying shapes and sizes with a high level of accuracy, as early as 0.35 ms after stimulation, despite large stimulus artifacts – even in same-lead recordings (Figure 3). The algorithm has proven useful in initial tests in hundreds of stimulation/recording combinations within the basal ganglia and thalamic nuclei during stimulation frequencies up to 250 Hz, and has promising applications in other modalities that allow for polarity reversal of the recorded stimulus artifact.

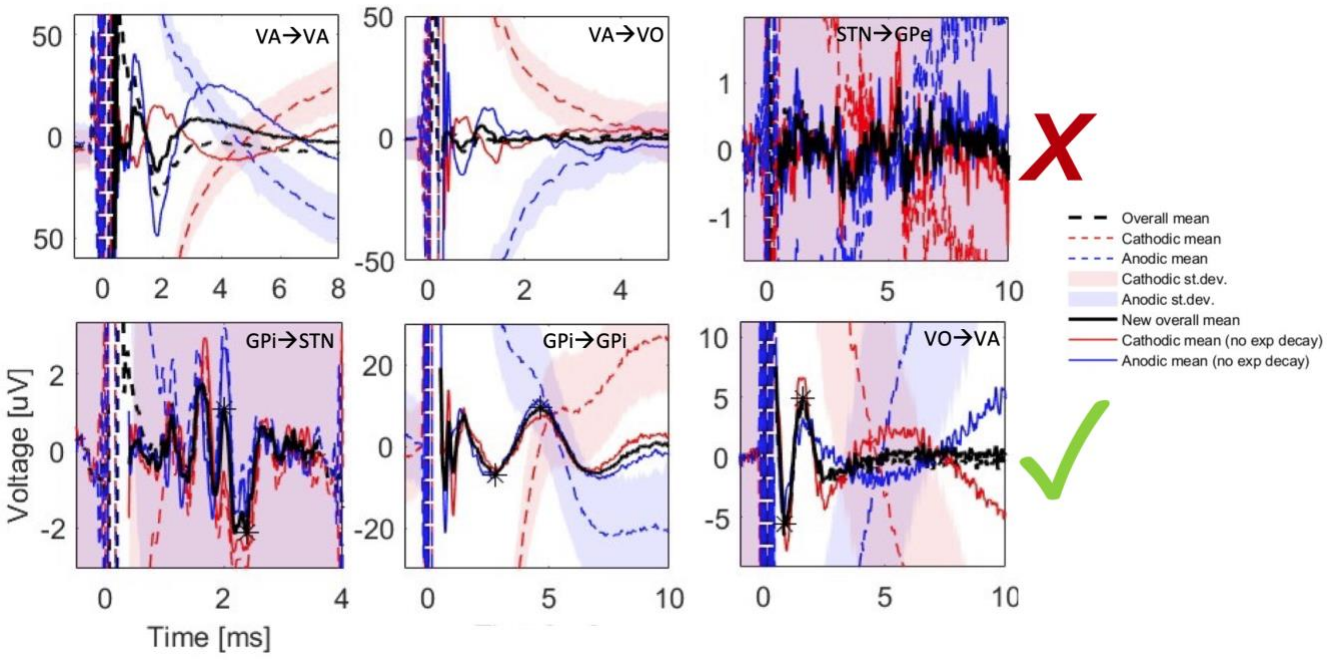

Figure 3. Summary figure for Chapter 3: An algorithm for automated detection of evoked potentials from polarity reversed electrical stimulation. Examples of rejected (top) and detected EPs (bottom) using the ADPREP algorithm. All examples are taken from different subjects and stimulation/recording combinations (see inserts in each subplot). *See Figure* 3.2 *for full figure description.*

Summary of Chapter 4: Increased deep brain stimulation frequency increases delay, decreases amplitude, and reduces high-frequency components in thalamic and basal ganglia evoked potentials

Preliminary results from this study of the effect of DBS stimulation on EPs found stimulation frequency to be negatively correlated with EP amplitude and positively correlated with EP delay; additionally, as stimulation frequency increases, high-frequency components of EPs seem to be suppressed (Figure 4). These trends may be related to refractory periods and oversaturation of neural receptors when stimulations are delivered at shorter intervals. Our findings will help shed light on the dystonic brain's frequency-dependent response to DBS and provide insight into how stimulation frequency can be used to generate wanted neural response patterns, in order to elicit the most effective clinical response to DBS treatment.

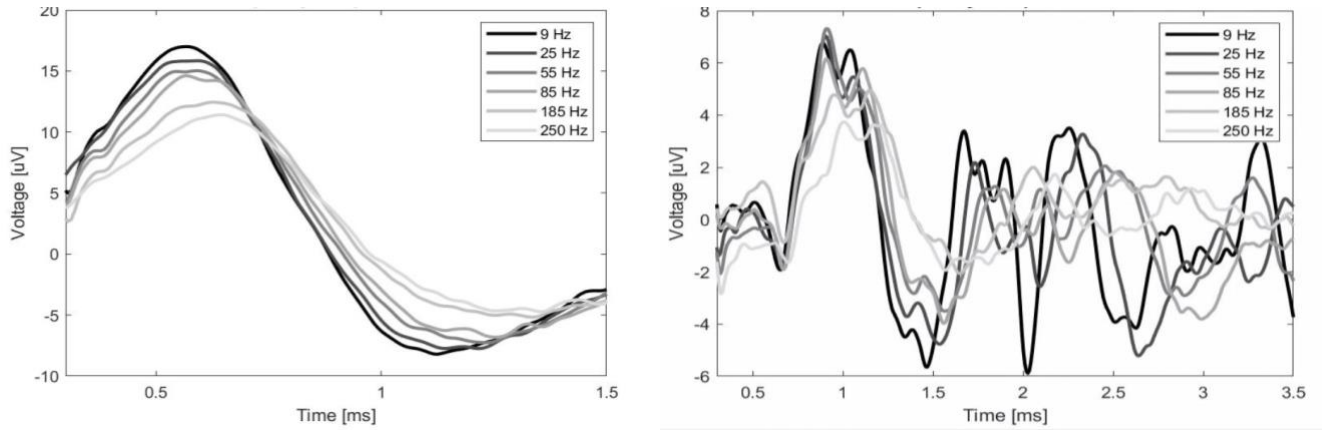

Figure 4. Summary figure for Chapter 4: Increased deep brain stimulation frequency increases delay, decreases amplitude, and reduces high-frequency components in thalamic and basal ganglia evoked potentials. The decreased amplitude and increased delay for higher stimulation frequencies is clear both in the left plot and in the segment prior to 1.5 ms in the right plot. After 1.5 ms, the right plot also exemplifies how higher frequency EP components are sometimes suppressed at higher stimulation frequencies. *See Figure* 4.1 *for full figure description.*

Summary of Chapter 5: Effects of benzodiazepines on deep brain activity and deep brain stimulation evoked potentials

We studied the effect of benzodiazepines (BZD) on deep brain regions both at rest and during DBS in pediatric subjects with dystonia. While the resting activity decreased significantly in all studied brain regions during BZD treatment (Figure 5, top), the effects on DBS EPs were more complex, with EP amplitudes significantly decreasing, increasing, or remaining similar depending on the connection (Figure 5, bottom). Our preliminary results indicate that changes in origin or target excitability due to BZD lead to changes in the effectiveness of communication between the two regions. This could in turn be responsible for changes in the overall pattern of activity, possibly interfering with or attenuating the transmission of the signals responsible for dystonia.

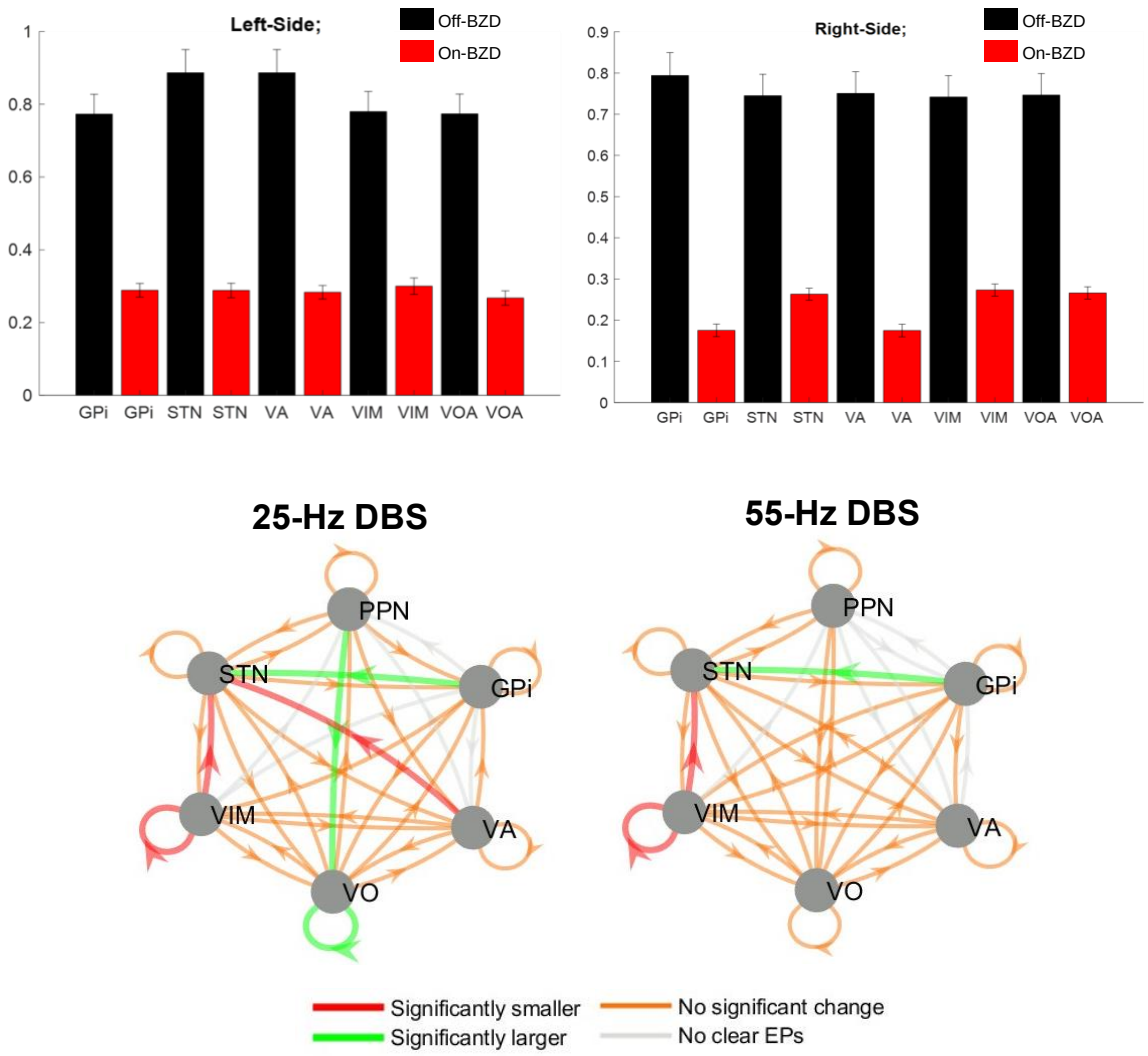

Figure 5. Summary figure for Chapter 5: Effects of benzodiazepines on deep brain activity and deep brain stimulation evoked potentials. Top row: Power spectral density (PSD) analyses for the deep brain nuclei in a sample subject: off benzodiazepines (black) versus on benzodiazepines (red). Activity was significantly reduced in all nuclei. Bottom row: Directed graphs showing the varied group effects of benzodiazepines on EP amplitude during 25-Hz (left) and 55-Hz DBS (right). *See Figure* 5.2 *and Figure* 5.4 *for full figure descriptions.*

Summary of Chapter 6: Modeling oscillatory deep brain stimulation evoked potentials with phase oscillator networks

We developed a network phase oscillator model to describe the mechanism behind DBS evoked oscillatory neural responses (EONRs). The model was trained with data from a pediatric primary dystonia patient during burst stimulation in globus pallidus internus (GPi). Not only did our model provide a good fit to the data (R^2=0.80), but when tested on a contrasting data set with different stimulation parameters, it was able to predict a response similar to the ground truth, suggesting that it captures important features of the network dynamics (Figure 6). Personalized models like these, tuned for each individual, could provide a quantitative method for DBS target localization and stimulation tuning for DBS treatment of dystonic patients.

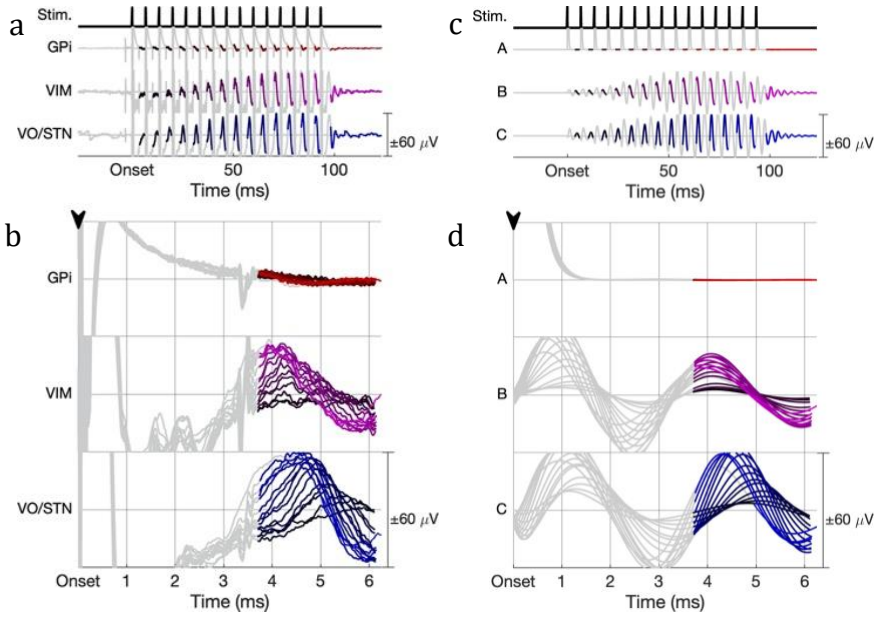

Figure 6. Summary figure for Chapter 6: Modeling oscillatory deep brain stimulation evoked potentials with phase oscillator networks. Comparison of the empirical data (a & b) and simulations using the phase oscillator network model (c & d). The EONRs elicited throughout the bursts shown in a & c are superimposed in b & d (aligned to their stimulations) to emphasize how well our model captures the change in neural responses throughout the burst. *See Figure* 6.3 *for full figure descriptions.*

Summary of Chapter 7: Diffusion tensor imaging coefficients correlate with deep brain stimulation evoked potential amplitudes and delays

Diffusion Tensor Imaging (DTI), a quantitative analysis method for evaluating white matter integrity, was implemented to study the correlation between DBS EP characteristics (amplitude and delay) and DTI coefficients: length, volume, and fractional anisotropy (FA) of fiber tracts (Figure 7). We completed a linear regression to generate a generalized linear model (GLM), the results of which showed that FA, tract length, and tract volume were significantly correlated with DBS EP characteristics. As such, our model validates DTI against ground truth electrophysiology, providing crucial and novel confirmation that EPs are affected by the brain's white matter integrity. Such a mathematical model has the potential to predict DBS EP characteristics using only DTI coefficients, which would open new possibilities for cases when intracranial deep brain recordings are not possible or available. Down the line, such a model may even be able to infer neurophysiological connectivity, and possibly predict optimal DBS lead implant targets.

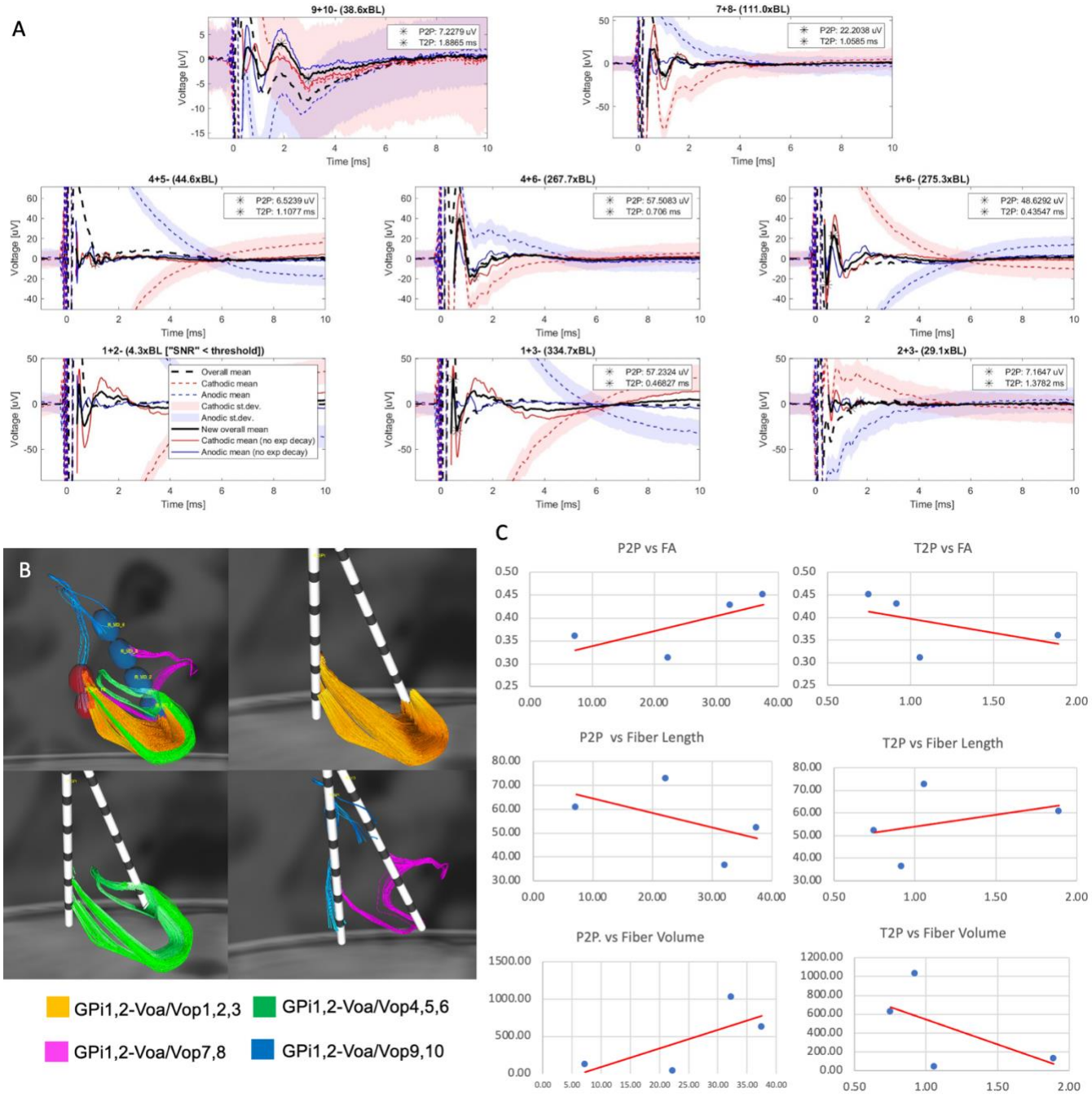

Figure 7. Summary figure for Chapter 7: Diffusion tensor imaging coefficients correlate with deep brain stimulation evoked potential amplitudes and delays. (A) Sample neural recordings from the micro-contacts in ventral oralis anterior/posterior (Voa/Vop) during 25-Hz DBS in globus pallidus internus (GPi). (B) Fiber tracking between macro-contacts in GPi (stimulation) and micro-contact rows in Voa/Vop (recording) in one patient. (C) Scatter plots with trend lines showing correlations between EP characteristics and DTI coefficients. *See Figure* 7.4 *for full figure description.*

Dystonia: etiology

Dystonia is a movement disorder characterized by limb twisting and repetitive movements, abnormal postures, or both, caused by involuntary sustained or intermittent muscle contractions [2] (Figure 8). Dystonia is commonly split into two types, depending on the underlying cause. When dystonia is the patient's main impairment, typically of a genetic origin, the term "primary dystonia" is used. Contrarily, if the impairment is a result of an outside factor, such as hypoxic-ischemic or traumatic brain injury, stroke, or toxins, it can be referred to as "secondary dystonia" [21]. While the signal flow responsible for dystonia is still unknown, theories include imbalances between midbrain dopaminergic and striatal cholinergic signaling, excessive basal ganglia or peripheral loop gain, abnormal patterns of subcortical activity, or a lack of focus of intended patterns of muscle activity [2]–[8]. In short, the motor symptoms of dystonia are thought to arise from abnormal neural activity.

While we treat and study other disorders, our research focuses mainly on pediatric patients with secondary dystonia due to cerebral palsy.

Figure 8. Postures, movement difficulties, and gait abnormalities commonly seen among patients with dystonia. The children depicted above are all current or previous patients of Dr. Sanger and research participants of the Sanger Lab.

Deep brain stimulation: for treatment and insight

While peripheral interventions for dystonia exist, including botulinum toxin, assistive devices, and orthopedic surgery, these interventions do not target the *source* of the impairment. Centrally acting drugs, including benzodiazepines, levodopa, and baclofen, contrarily have the ability to modulate the abnormal neural activity underlying dystonia [6]. However, these medications come with common side effects including drowsiness or anxiety; for example, parents of our patients have previously voiced concerns that their child is "not there" while medicated. Moreover, the medications are not always effective in relieving the symptoms.

In these cases, DBS has shown optimistic results through its past few decades of use [6]. DBS is a treatment method that involves implanting electrodes into carefully selected brain regions, where administered local electrical currents can change the way the brain processes information, without altering brain structure. While the mechanism of DBS is not yet fully understood, the underlying idea is that the electrical stimulations alter local neuron membrane

potentials. Depending on stimulation settings such as location, frequency, voltage, pulse shape, and pattern, the stimulation affects the brain differently, and can reduce or increase brain activity, locally as well as downstream [22].

Due to all these potential settings, benefits of DBS include not only the ability to treat dystonia at its source, but also the *selectivity* of such treatment when stimulating brain region sizes of the order of square centimeters. This high selectivity allows us to narrow in on specific target regions that have shown clinical efficacy in dystonic patients when lesioned or electrically stimulated. Such regions commonly include the basal ganglia and thalamus [23]–[27], two structures involved in sensorimotor control.

Finally, one major added benefit of deep brain electrodes such sEEG leads (also referred to as depth leads) is their ability to, in addition to stimulate, *record* [20]. While long-term implanted DBS electrodes are typically used solely for stimulation, some short-term depth leads, such as those used in our studies, can be externalized by connecting their proximal extension to an amplifier, allowing for both recording and stimulation in the targeted brain region (Figure 9). This provides an invaluable opportunity to probe the deep brain regions postulated to be possible sources of dystonic symptoms, including basal ganglia and thalamic nuclei. For example, since GPi is an input to secondary thalamic nuclei, we can probe transmission of motor signals into these nuclei by recording their response to GPi DBS.

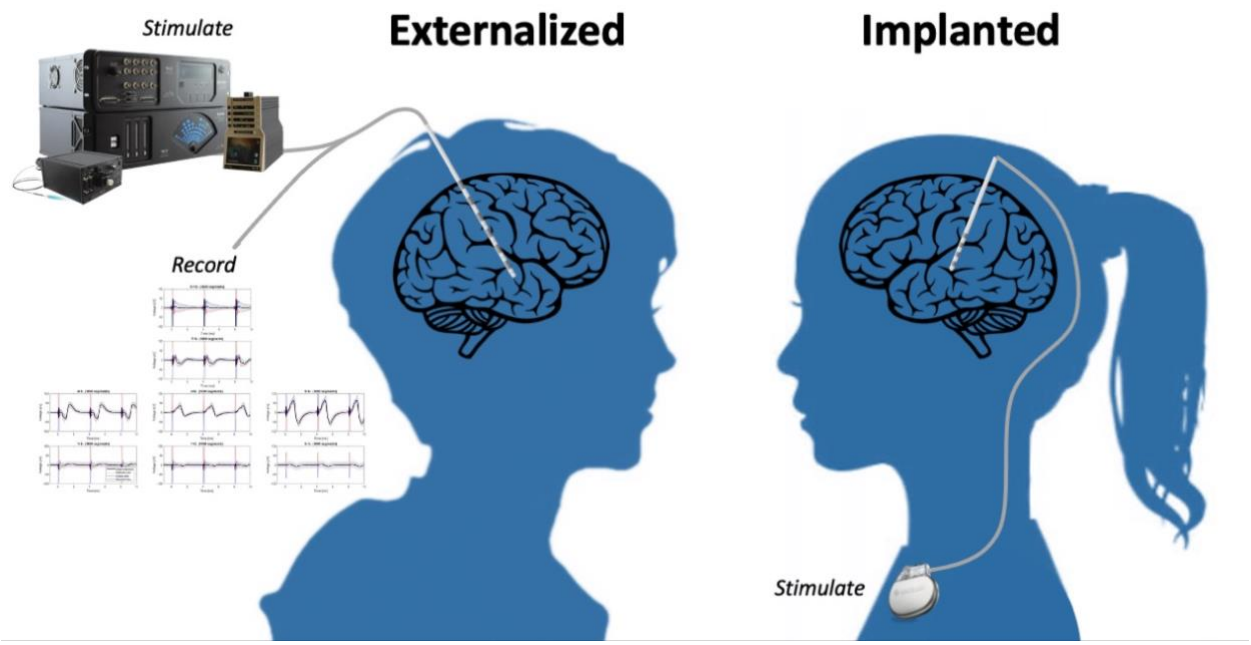

Figure 9. Visualization of the differences between externalized and implanted deep brain stimulation (DBS) systems. While closed-loop implanted DBS systems (using recordings to adjust stimulation settings) exist, most implanted DBS systems are open-loop (only stimulation, no recording). Externalized systems, contrarily, have the benefit of recording and stimulating simultaneously.

While electrical stimulation is very different from the brain's natural activity, exogenous stimulations allow us to gain insight into the brain's hardware and signal flow, its response to electrical stimulation, and the mechanism involved. These insights could, in turn, have a significant impact on how dystonia is treated, and, in the near future, allow us to provide effective DBS treatment at a much greater accuracy than in the current day.

Peripheral nerve stimulation: a non-invasive alternative to DBS

A downside of DBS as a treatment for dystonia is its highly invasive nature, requiring brain surgery to implant the leads in the target brain regions. To avoid both invasive treatments and strong medications, PNS has been proposed as a noninvasive treatment method [13] (Figure 10)

to modulate neural activity at the subcortical level in subjects with movement disorders including essential tremor (ET) [17], [18], Parkinson's disease (PD) [19], and dystonia [14], [15].

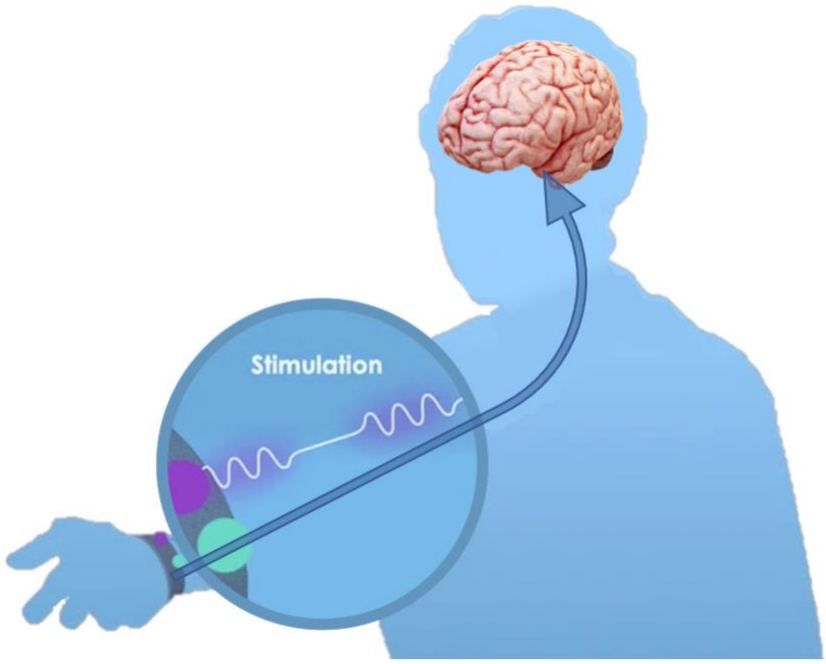

Figure 10. Visualization of peripheral nerve stimulation (PNS). Stimulation is provided over peripheral nerves, e.g. on the wrist (as shown above). Neural responses travel to the brain, where they can have modulatory effects on abnormal neural activity in patients with movement disorders.

Moreover, when used in combination with DBS recordings, PNS allows us to explore the transmission of sensory information to primary nuclei in the brain. Prior work has shown that there is a robust evoked response to PNS in sensory thalamic nuclei, including the ventral intermediate nucleus (VIM) and the ventral posterolateral nucleus (VPL) [16], [28]–[31], likely mediated through cerebello- and spinothalamic pathways. This response has led to the conjecture that PNS could have a similar effect to thalamic DBS, and might thus ameliorate movement disorders where intracranial thalamic stimulation has been effective.

However, similarly to DBS, the mechanism of PNS as a treatment is not yet clear, and as such, insight into its mechanism of action and effect on the nervous system would aid in the development of more effective treatments.

GENERAL METHODS

Patient selection

Subjects for clinical DBS surgery were chosen based on the inclusion criteria of all of the following: presence of movement disorder, significantly limiting or interfering with normal function or care; potential stimulation targets, identifiable with MRI; and low success from symptomatic or etiologic medical therapy. Prior to the study, the subject and parent(s) consented, or assented as applicable, to the research use of electrophysiological data collected during the clinical procedure and completed a Health Insurance Portability and Accountability Act (HIPAA) authorization for the research use of protected health information. All research use of data was approved by the institutional review boards of Children's Hospital Los Angeles (CHLA) and Children's Health Orange County (CHOC).

Data from a total of 36 pediatric patients were available for use in my analyses, with 16 being collected with my help during the course of this dissertation research.

Data collection

The experimental protocol took place in the hospitals' inpatient NMU [20]. During surgery to establish optimal permanent DBS lead placement, up to 10 temporary sEEG leads were implanted into potential deep brain targets, identified prior to surgery through a collaborative consultation between the departments of Neurology and Neurosurgery at CHLA or CHOC. Typical target areas included basal ganglia (e.g., GPi and the subthalamic nucleus, STN) and thalamus, with its sensory (primary) nuclei (e.g., VIM and VPL) and motor (secondary) nuclei (e.g., ventral oralis

anterior/posterior, Voa/Vop, and ventral anterior, VA) (Figure 11). These areas were selected due to prior studies of clinical efficacy in dystonic patients when lesioned or electrically stimulated [23]–[27]. Each implanted and externalized Ad-Tech MM16C sEEG lead (Ad-Tech Medical Instrument Corp., Oak Creek, WI, USA) consisted of 6 low-impedance ring electrodes referred to as "macro-contacts", and 10 small high-impedance circular electrodes referred to as "micro-contacts" (Figure 12). These intracranial leads were linked to the amplifier inputs via Tucker-Davis Technologies Cabrio™ (TDT, Tucker-Davis Technologies Inc., Alachua, FL, USA) connectors modified to include a custom unity-gain preamplifier for each microelectrode to reduce noise and motion artifacts.

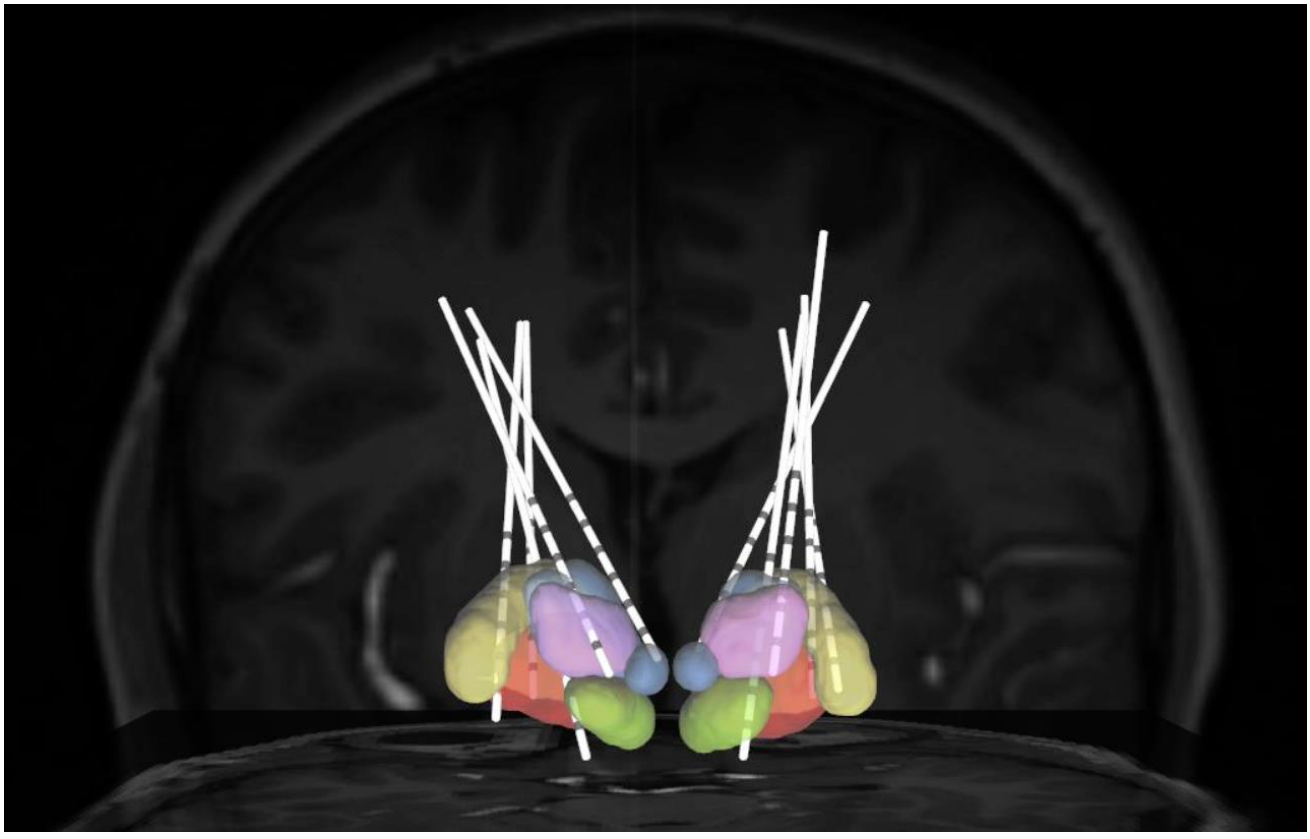

Figure 11. A 3D rendering based on co-registered CT and MRI images from an individual patient. Implanted sEEG electrodes are visualized in common target areas: VIM (pink), Voa/Vop (blue), STN (green), GPi (red), and globus pallidus externus (GPe, yellow).

In the 2-5 days following lead implantation, after allowing the patient to fully recover from the effects of the general anesthesia administered for surgery, clinical and scientific testing and data collection were performed with the patient awake and unrestricted. Data were recorded through micro-contacts, sampled at ~24 kHz and band-pass filtered at 0.3-9 kHz.

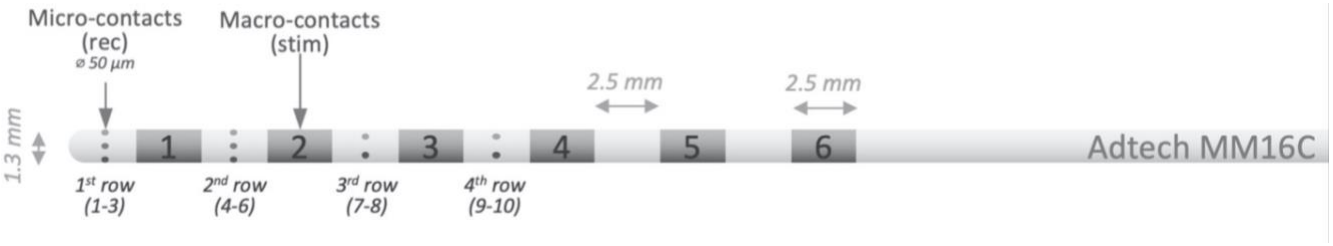

Figure 12. Schematic of the Ad-Tech MM16C externalized sEEG leads used in the NMU. Each lead contains six (6) low-impedance ring electrodes, referred to as "macro-contacts" (large gray squares), and ten (10) small low-impedance circular electrodes (small gray dots), referred to as "micro-contacts". In our studies, macro-contacts were used for stimulation and micro-contacts for recording.

Recordings were gathered using either a system consisting of a PZ5M 256-channel digitizer, an RZ2 processor, and an RS4 high speed data storage (TDT), or a NeuroOmega™ 96-channel system (AlphaOmega Co USA Inc., Alpharetta, GA, USA).

Stimulation protocols

Electrophysiological brain responses to external stimulation, termed evoked potentials (EPs), are commonly classified as either transient or steady state [32]–[35]. This distinction is important because the brain is not a linear system; hence, the study of both immediate and prolonged responses to external stimuli are important to gain a complete view of the brain's function [35]. Because of this, two main stimulation patterns were used in this dissertation research. Repetitive *constant* stimulation allowed us to study the average, i.e., steady state neural response, whereas

stimulation *bursts* separated by brief periods without stimulation let us probe the initial build-up of the brain's response through each burst, i.e., the transient response. The latter is a less commonly used stimulation pattern that allows unique insight into the *dynamics* of the neural response.

Intracranial constant & burst stimulation

The constant intracranial testing protocol consisted of stimulations of 90-us, 3-V charge-balanced pulses at frequencies ranging from 9-250 Hz (9, 25, 55, 85, 185, or 250 Hz), administered through two adjacent macro-contacts (anode and cathode) at a time. Approximately 1200 repetitions or 15 seconds of stimulation (whichever was greatest) were administered per stimulation frequency, after any voltage ramping was complete (relevant only at higher frequencies). Stimulations were typically administered through a total of two to three contact pairs on each sEEG lead.

For artifact cancellation purposes, both "cathodic" and "anodic" stimulations were performed for intracranial stimulation. That is, the two stimulation contacts ("A" and "B") were stimulated as A+B- (A=anode; B=cathode), and then B+A- (B=anode, A=cathode), with the results averaged in the subsequent data analysis. This polarity reversal technique takes advantage of the nonlinearity of the neural response by inverting the polarity of the stimulation artifact, while preserving the polarity of the evoked potential. Therefore, the inverted cathodic and anodic stimulation artifacts not only help distinguish artifacts from neural responses, but also cancel each other out to reduce artifact contamination in the average response – which is especially helpful in

recordings with short latency EPs.[1] Intracranial constant stimulation data were available from 36 patients.

The intracranial burst stimulations were instead provided in 100-ms bursts, separated by 100 ms *without* stimulation, with within-burst frequencies ranging between 50-250 Hz, either in multiples of 50 Hz (Figure 13), or at frequencies matching constant stimulations (e.g. 55, 85, or 185 Hz). The repetitive bursts separated by off-stim periods allowed us to study the brain's transient (initial) response to DBS. Intracranial burst stimulation data were available from 12 patients.

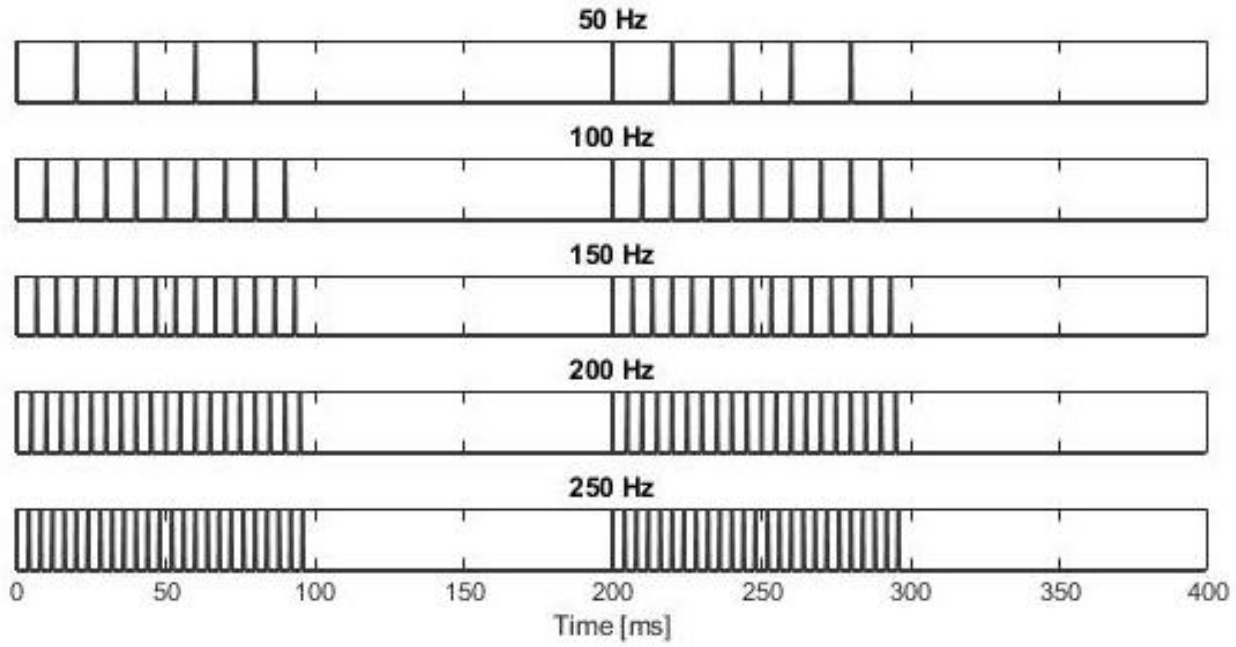

Figure 13. Visualization of burst stimulations. 100-ms bursts of stimulation were separated by 100 ms without stimulation. The above examples show within-burst frequencies of 50, 100, 150, 200, and 250 Hz (from the top down).

[1] It should be noted that because the cathode acts as the active electrode, and the anode as the returning electrode, this polarity reversal technique effectively leads to a slight shift in stimulation location (5 mm, the distance between the stimulated macro electrode pairs). Therefore, the final averaged response of the two stimulation types is, in fact, an average of stimulations at two different locations, which may lead to slight timing or amplitude differences between the two.

Peripheral constant & burst stimulation

Peripheral stimulation was applied to the median nerve at the wrist through 1-cm adhesive disk electrodes, with the cathodic electrode placed proximally. Current-controlled stimulations were provided through a STMISOLA isolated stimulator (Biopac Systems Inc., Goleta, CA, USA), driven by a pulse train generated by a Power1401 digital to analog converter (Cambridge Electronic Design Inc., Cambridge, UK).

Peripheral stimulations consisted of biphasic stimulation pulses, provided both at a constant frequency of 5 Hz and in stimulation bursts equivalent to the intracranial burst protocol (50-250 Hz; 100 ms on, 100 ms off; Figure 13). For each stimulation frequency and type, the amplitude of the stimulus was slowly increased until a palpable twitch was evoked in the subject's thenar muscles, unless the subject experienced discomfort before this motor threshold; in this case, the highest amplitude without patient discomfort was used. Thereafter, four minutes of stimulation were performed for each frequency and on each wrist, generating approximately 1200 stimulation bursts per condition.

PNS allowed us to study neural transmission from peripheral nerves to sensory thalamic motor nuclei, and was available from 26 patients.

Data treatment

All data treatment was performed in MATLAB (The MathWorks, Inc., Natick, MA, USA). The recorded neural activity was defined as the relative response between two nearby contacts (i.e., local bipolar recordings) and was time-averaged and time-locked to a stimulus artifact. To ensure accuracy and avoid time delays in synchronization pulses between different equipment, the

stimulus time was identified by looking for the occurrence of stimulus artifacts in the recorded data.

The raw data were upsampled, searched for stimulus artifacts, and split into segments (200 ms wide for burst data, and 11 ms for constant stim data). All ~1000 segments not flagged as outliers were then aligned to each other through cross-correlation of an artifact, defined as time "0", and finally averaged. This stimulus-triggered averaging procedure greatly increased the signal-to-noise ratio (SNR) of the final average response.

If both cathodic and anodic stimulations were administered, the above process was repeated for both stimulation types, the results of which were finally averaged to obtain a stimulus artifact-reduced neural recording.

Parameters of interest

After data treatment, neural responses to electrical stimulation could be clearly identified by their substantial deviation from baseline neural activity. These EPs were then characterized by their peak-to-peak amplitude (P2P), time-to-(first-)peak delay (T2P), and shape (Figure 14). This provided quantitative measurements of EPs, which I used in my analyses to investigate how the basal ganglia and thalamic neural response to exogenous electrical stimulation differed based on stimulation patterns and frequencies, between different stimulation and recording regions, in different conditions, and over time.

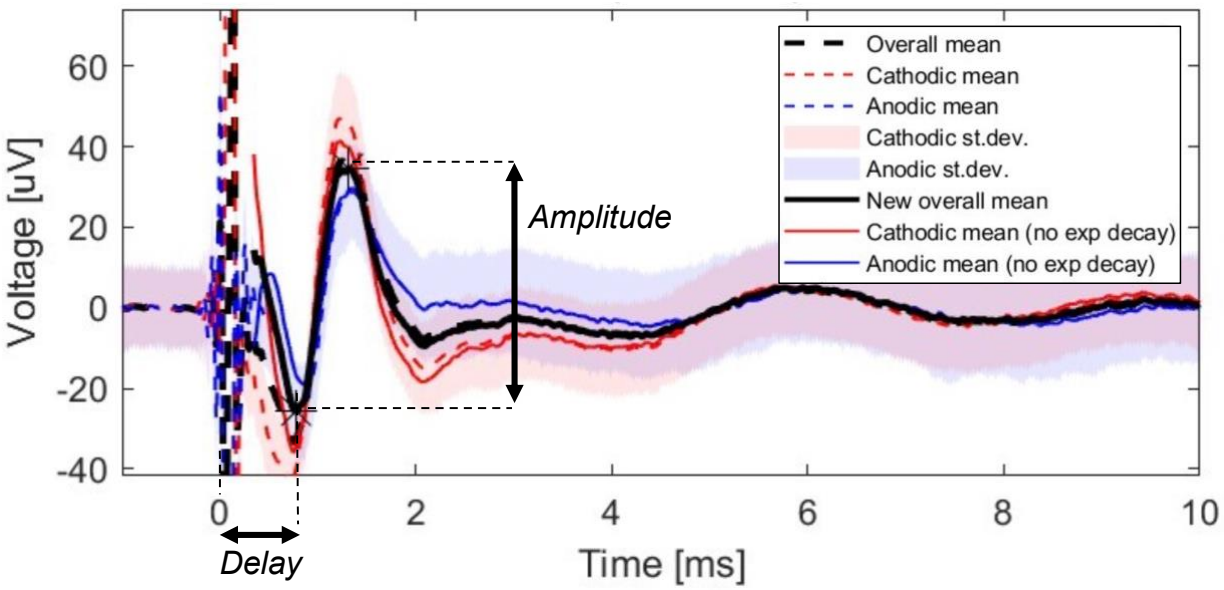

Figure 14. Example of an evoked potential, denoting its delay and amplitude. The T2P delay is measured as the time from start of stimulation (time 0) to the (first) EP peak, while the P2P amplitude is measured from peak to peak. This EP example is from intracranial stimulation, hence the rapid delay of <1 ms. Median nerve PNS EP delays typically range from ~10-20 ms due to the transmission time required from the wrist to the brain. *Dashed red and blue lines are stimulus-triggered averages of the cathodic and anodic stimulation types, respectively, with shaded standard deviations; solid red and blue lines are the signals after removal of decay artifacts (see Chapters 1 & 3 for more details on the decay artifact removal method); solid black lines are the average between the decay artifact-reduced cathodic and anodic signals. Stars denote the detected positive and negative peaks of the labeled evoked potentials.*

CHAPTER 1: NOVEL DECAY ARTIFACT REMOVAL METHOD REVEALS INCREASING CONSISTENCY OF THALAMIC RESPONSE TO REPETITIVE PERIPHERAL NERVE STIMULATION

I here introduce an artifact removal method that enabled us to detect an increasing consistency of thalamic neural responses during bursting PNS. This chapter is a reprint of the text and figures from my first-author publication "Increasing consistency of thalamic response to repetitive peripheral nerve stimulation" from 2021 [36]. My contributions to this paper included investigation, data curation, software, formal analysis, validation, writing (original draft as well as review and editing), and visualization [37]. Some text and figures have been rearranged or omitted to preserve the flow of this dissertation.

1.1 Abstract

Objective. Peripheral nerve stimulation has been proposed as a noninvasive treatment for patients with movement disorders such as essential tremor, Parkinson's disease, and dystonia. While the outcomes have shown clinical effect, the mechanism behind the effect is not yet clear. The goal of this work was to study the brain's responses to peripheral stimulation bursts and explain the therapeutic results. *Approach.* We performed peripheral stimulation of the median nerve(s) in 12 pediatric patients undergoing deep brain stimulation for dystonia. Stimulation was given in bursts (50-200 Hz stimulation in blocks of 100 ms, separated by 100 ms without stimulation) while intracranial activity was simultaneously recorded from stereo-electroencephalography leads implanted in thalamic nuclei. After using a novel method to remove stimulus decay artifacts, sequences of neural responses during and after the bursts could be analyzed. *Results.* Peripheral

burst stimulation induced increasing consistency of successive evoked responses in thalamic nuclei. *Significance.* We propose that this phenomenon is due to progressive synchronization of small populations of thalamic neurons, so that over time there is phase locking of the response in an increasing number of neurons in the population. Clinical efficacy could thus be due to "synchronization blockade", in which the synchronized response of the population prevents transmission of intrinsic abnormal signals due to tremor or dystonia. Further studies are necessary to confirm this model of clinical effect. Enhanced understanding will increase the potential for use of peripheral stimulation as a noninvasive alternative or adjunct to deep brain stimulation.

1.2 Introduction

Neural responses generated by electrical stimulation are commonly mixed with stimulus artifacts [38], [39]. While these artifacts can serve as a marker to aid in alignment of neural responses with their respective trigger, electrical stimulations often cause problems, not only by saturating the recording contacts, but also because the capacitive components in the contacts give rise to a capacitive discharge phase, prolonging the time required for the recording contact to return to baseline [39]. This complexity of stimulus artifacts may explain why many PNS studies use low-frequency stimulation (<10 Hz), allowing for ample time between stimuli [31], [40]–[43].

However, while the saturation period typically leads to a complete loss of neural recordings, neural responses generally *can* be recorded during the capacitive discharge phase after the saturation period. The concern here is instead separating the neural activity from this "decay artifact". Decaying exponential models have been previously implemented to remove decay artifacts [44], [45], and have proven more successful at removing artifacts than other common

methods, including independent component analysis (ICA).[2] Expanding on these models, we here present a novel method that incorporates complex exponentials to fit to and accurately remove oscillating decay artifacts.[3] This method allows us to reduce the stimulus artifact influence and avoid noise distorting the recorded neural response.

The robustness and reliability of the method were tested on sEEG recordings from thalamic nuclei during high frequency peripheral stimulation in pediatric patients with movement disorders, including generalized dystonia and hemidystonia. The results promote the method's ability to extract clear neural responses, not only *after* the last pulse in the burst, but also *between* pulses, in studies with high-frequency stimulations. Furthermore, results show a new phenomenon of progressive increase in consistency, consistent with a model of neural population synchronization in response to repetitive stimulation.

1.3 Materials & methods

1.3.1 Patient selection

Data from 12 pediatric patients (7 male, 5 female, 6-20 years old, median age: 16) were used in this study (Table 1.1).

[2] The stimulus artifact and the evoked potential always correlate, since one causes the other. Hence, ICA is inherently not an applicable approach for stimulus artifact removal.

[3] The decay artifact shape is affected by factors including stimulation and recording contacts, and may also vary between subjects.

Table 1.1. Demographic characteristics of the 12 subjects included in the PNS study.

Subject	Etiology	Characteristics	Gender	Age [Years]	Stimulated wrist(s)
1	Kernicterus	Dystonia	F	19	L, R
2	Stroke, secondary to Hemolytic Uremic Syndrome	Dystonia	F	6	L, R
3	Cerebral Palsy	Dystonia	M	20	L, R
4	Cerebral Folate Deficiency (diagnosed Cerebral Palsy)	Dystonia	M	8	L
5	Primary Dystonia (ADCY5)	Dystonia	M	10	L, R
6	Unknown (possibly Vasculitis)	Left hemidystonia	M	15	R
7	Cerebral Palsy	Dystonia	F	15	L, R
8	Cerebral Palsy	Dystonia	M	20	L, R
9	Cerebral Palsy	Dystonia	M	18	L, R
10	Kernicterus	Dystonia	M	19	R
11	Cerebral Palsy	Dystonia	F	16	L, R
12	Primary Dystonia (DYT1)	Dystonia	F	16	L, R

Abbreviations: F, female; M, male; L, left; R, right.

1.3.2 Peripheral burst stimulation

Peripheral stimulation was applied to the median nerve at the wrist in the manner described previously in the General Methods: biphasic pulse stimulations were administered in frequencies of approximately 50, 100, 150, and 200 Hz, active in 100-ms bursts, separated by 100 ms without stimulation (Figure 13, General Methods).

1.3.3 Data treatment

The data were upsampled, searched for stimulus artifacts, and split into ~1000 segments, which were finally stimulus-triggered averaged to increase the SNR of the final average response.

1.3.4 Artifact removal

After data treatment, decay artifacts were removed. For non-oscillatory "simple" exponential decay artifacts (Figure 1.1A), we concur with [45] that the addition of *two* separate exponential decays is necessary to accurately model the capacitive discharge. Hence, the following simple exponential decay artifact model (SEDAM) was used to fit to and remove these types of decay artifacts:

$$\text{SEDAM} := A_1 e^{\lambda_1 t} + A_2 e^{\lambda_2 t} + C \tag{1.1}$$

where A_1 and A_2 denote the amplitudes and λ_1 and λ_2 the decay constants of the two exponential components, and C denotes the baseline offset.

However, for oscillating decay artifacts (Figure 1.1B), the simple exponential does not suffice to model and remove the artifact. Hence, we here present a novel artifact removal method, which uses the complex exponential $\alpha e^{\beta t}$ [46], where α and β are complex numbers, and the magnitude of α is denoted as A:

$$\alpha = |\alpha| e^{i\theta} = A e^{i\theta} \tag{1.2}$$

$$\beta = \lambda + i\omega_0 \tag{1.3}$$

Expanding the exponential using Euler's formula,

$$e^{i\varphi} = \cos(\varphi) + i \sin(\varphi), \tag{1.4}$$

and using the definitions from Equations 1.2 and 1.3, the complex exponential can be separated into real and imaginary components:

$$\alpha e^{\beta t} = A e^{i\theta} e^{(\lambda + i\omega_0)t} = A e^{\lambda t} e^{i(\omega_0 t + \theta)} = A e^{\lambda t} (\cos(\omega_0 t + \theta) + i \sin(\omega_0 t + \theta)) =$$

$$\underbrace{Ae^{\lambda t}\cos(\omega_0 t+\theta)}_{\mathrm{Re}(\alpha e^{\beta t})} + i\underbrace{Ae^{\lambda t}\sin(\omega_0 t+\theta)}_{\mathrm{Im}(\alpha e^{\beta t})} \tag{1.5}$$

For our purposes, only the real component of the complex exponential, corresponding to a damped oscillator, is relevant for the modeling of the decay artifact. Similar to the simple exponential model, a combination of *two* real complex exponentials was necessary to accurately model all oscillatory decay artifacts in our data, leading to the final definition of the complex exponential decay artifact model (CEDAM):

$$\mathrm{CEDAM} := A_1 e^{\lambda_1 t}\cos(\omega_{01} t+\theta_1) + A_2 e^{\lambda_2 t}\cos(\omega_{02} t+\theta_2) + C \tag{1.6}$$

where, similar to the simple exponentials, A_1 and A_2 denote the amplitudes of the two complex exponentials, λ_1 and λ_2 the decay constants of the respective exponential components, ω_{01} and ω_{02} the angular frequencies of the respective sinusoidal components, and θ_1 and θ_2 their angular offsets. C denotes the baseline offset.

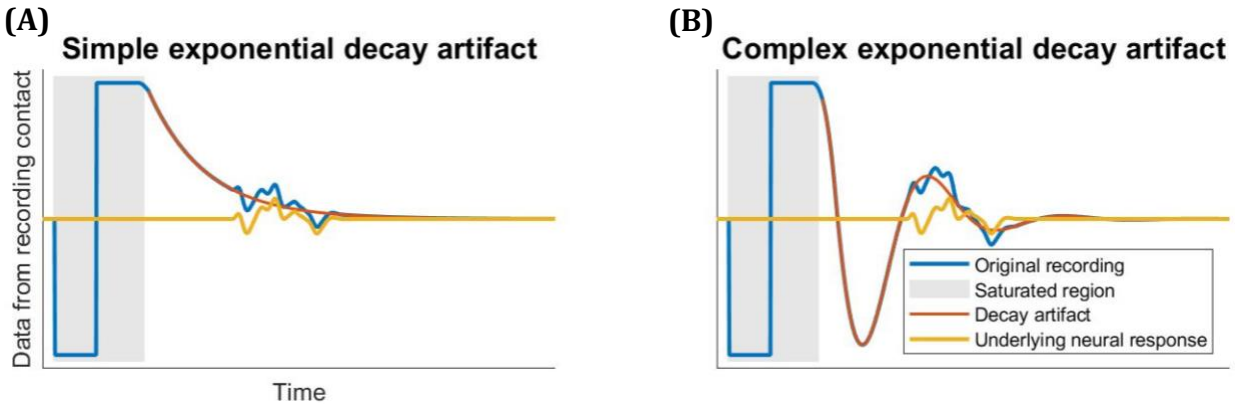

Figure 1.1. Simulated visualizations of simple and complex exponential decay artifacts, and how they can corrupt the underlying neural response. Common types of decay artifacts (orange traces) can complicate the detection of the underlying neural response (yellow) from the raw recording (blue). Plot (A) portrays a recording with a simple exponential decay artifact, while (B) shows a complex exponential decay artifact. The gray box highlights the region where the stimulus artifact saturates the recording contact, during which the contact is unable to record neural activity.

Note that in order to prevent overfitting to the neural response, rather than fitting to just the decay artifact, the fit should ideally only be based on the segment *before* the first EP. Using this first fit to remove all stimulus artifacts in the burst ensures that the fit is only based on, and hence will only remove, components due to the stimulus artifact.[4]

Hence, the appropriate decay artifact removal model (simple or complex exponential) was fit to the data segment that extended from the end of the first stimulus artifact's saturated region until the (expected) EP or the next stimulation, whichever came first. This fit was then used to remove the decay artifacts throughout the whole burst, when suitable.[5] After removal of the decay artifacts, the saturated regions of the stimulus artifacts (from 0.3 ms before to 2.8 ms after the start of the stimulation) were interpolated, and the average segment was high-pass filtered with a cutoff of 50 Hz. The saturated regions were thereafter blanked for visualization purposes. R^2 values were calculated between the decay artifact fit and the data segment used for fitting to determine goodness of fit (GoF).

1.3.5 Evoked potential characterization

Due to differences in impedance and target region accuracy[6] between the contacts on each DBS lead, some contact recordings displayed clearer EPs than others. Hence, for each subject, hemisphere, and recording region, if multiple EPs were visually detected, the contact combination with the clearest response was used in the subsequent analysis.

---

[4] This assumes that the decay artifacts of all stimulations in the burst are identical. This is, however, generally a fair assumption, considering that they are generated by stimulations of the same shape and size, originating from the same contacts, and recorded from the same contacts.

[5] In the rare cases that the first fit was not a good approximation of the subsequent decay artifacts, individual fits were implemented and removed.

[6] The length of the DBS lead is typically larger than the target brain region, which may cause some contacts to be outside the target region.

After visual inspection, an SNR threshold of 0.8 was empirically selected to automate the process of including only clear data samples: only those recordings containing at least one EP above this threshold after detrending were included in the analysis.

1.3.6 Analysis methods

The synchronization change throughout each burst was investigated by calculating the cross-correlation between each adjacent EP[7]. The trend of cross-correlation between adjacent EPs throughout each burst frequency was determined and tested for a monotonic trend in a population analysis using the seasonal Kendall test [47].

The analysis above was also repeated after adding white noise to higher-amplitude EPs to make all EP SNRs in each burst equal (or equal to 1, whichever was greatest). This allowed us to test if any of the observed correlation trends were merely attributed to differences in SNR between EPs, and would hence disappear when SNR was equal.

1.4 Results

The dual exponential fit methods (SEDAM and CEDAM) successfully modeled and removed the decay artifacts of both simple and complex exponential shapes (Figure 1.2), with R^2 measures up to and greater than 0.99, allowing for clear analysis of the underlying within-burst EPs.

[7] To ensure equivalent comparisons, only data regions containing EPs after stimulations (and of equal overlap, if applicable) were included in the analysis.

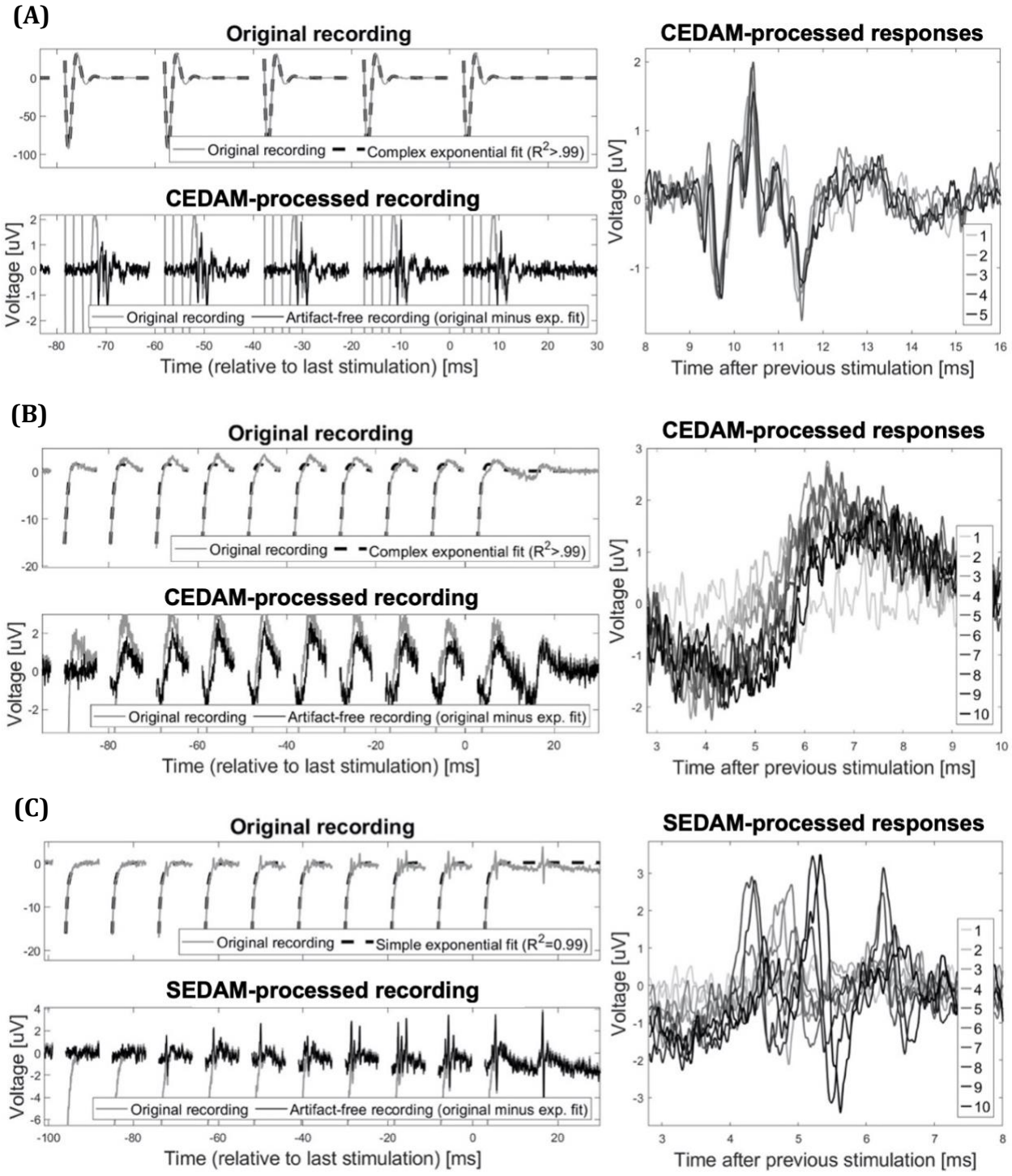

Figure 1.2. Removal of simple and complex exponential decay artifacts. Complex (A, B) and simple (C) exponential decay artifacts can be accurately removed with the methods described in this paper (left plots), to unveil the underlying neural responses (right plots). In each group of plots (A, B & C, respectively), the top left plot shows the underdamped oscillatory decay artifact fit (black dashes) under the original data (gray), from 50-Hz (A) and 100-Hz (B & C)

stimulation bursts. When the decay artifact is removed, the underlying neural responses can be seen (bottom left plots, black tracings). The right-most plots show the EPs from each stimulation in the burst overlayed to highlight their strong correlation. The example in (B) in particular demonstrates how basing the fit on the data before the first EP avoids overfitting to EPs, removing only decay artifacts and leaving EPs intact. *Note: stimulus artifact saturated regions have been blanked. Abbreviations: CEDAM/SEDAM, complex/simple exponential decay artifact model.*

For all investigated frequencies and recording regions, significant monotonic increases in cross-correlation throughout the burst were detected (Figure 1.3, top), indicating progressively increasing consistency in EP shape. Even after adding noise to even out the SNRs of the EPs within each burst, significant monotonic increases in consistency were seen for all recorded regions and frequencies, with only one exception[8] (Figure 1.3, bottom).

[8] This exception displayed a p-value of .0532, just above the significance threshold of 0.05.

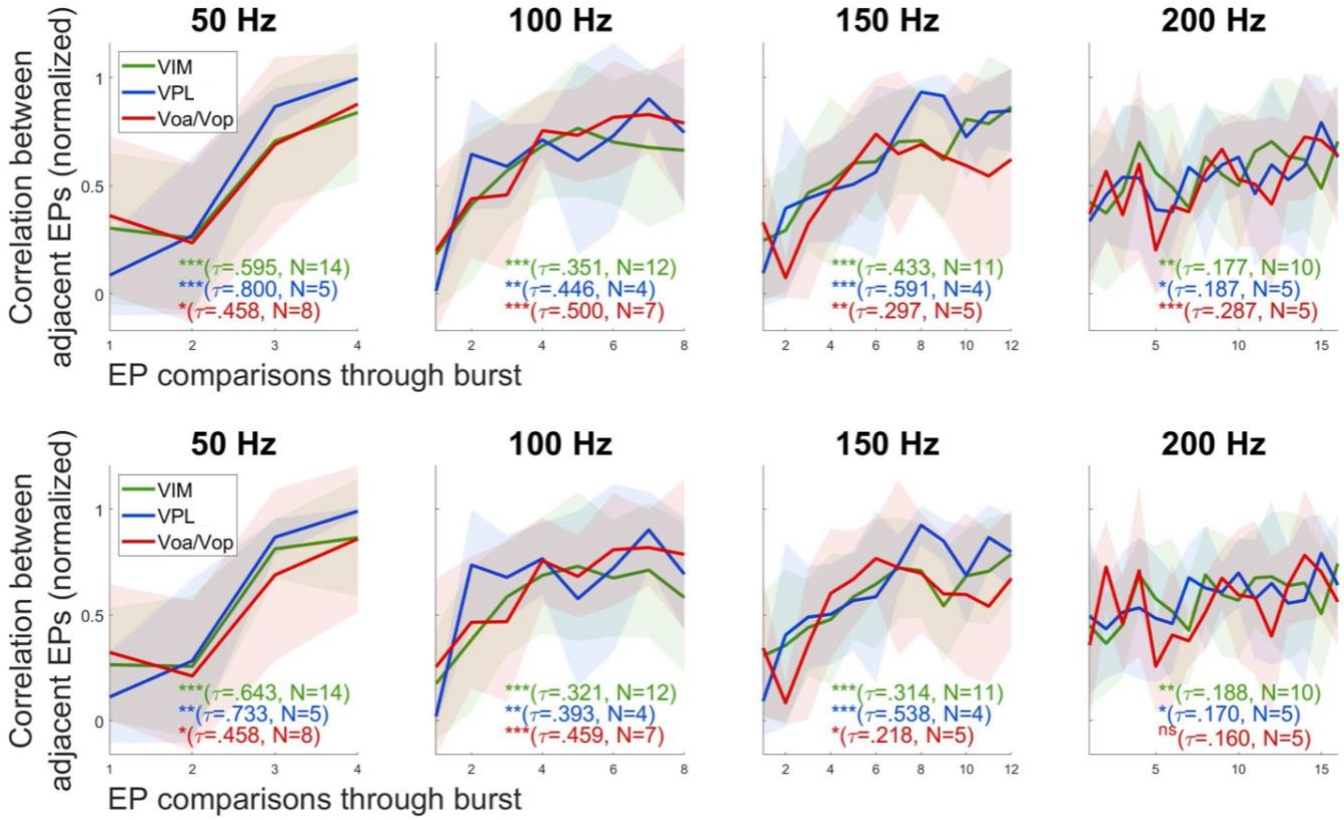

Figure 1.3. Correlations between adjacent evoked potentials (EPs) increase with time during the stimulation bursts. Correlation trends from all subjects & hemispheres were normalized before calculating mean (lines) and standard deviation (shadings) for each stimulation frequency group (subplot titles). In addition to studying the original data (top), white gaussian noise was thereafter added to make EP SNRs equal through each burst (bottom). Statistical monotonic increases in correlation were seen in all recording locations (VIM, green; VPL, blue; Voa/Vop, red) and over all stimulation frequencies, except in the highest frequency of noise-added Voa/Vop results (p=.0532). The significant increases in correlation are shown by the positive and significant tau value results from the seasonal Kendall test (listed in the bottom of each subplot). The consistent results, even after adding gaussian noise, insinuate that mere increased EP amplitude (and hence, SNR) is not the sole reason for the observed correlation increases. *Symbols: τ, Kendall's tau (measure of monotonic strength); *, p<0.05; **, p<0.01; ***, p<0.001; N, number of samples (subjects and hemispheres) with clear EPs.*

1.5 Discussion

Many studies display difficulties in removing decay artifacts [28], [40]–[43], [48], generating unusable data portions that our novel method could greatly reduce. Our results show the reliability and accuracy of the presented decay artifact removal method, which allows us to detect EPs during high-frequency stimulation. In addition to the very high GoF measures, the similarities of the EPs to previous studies (e.g. [40]–[43]) along with the electrical basis of the artifact model, differing from typical EP shapes and models, provide even stronger proof of success. We also highlight the importance of fitting to the decay artifact portion *before* the first EP whenever possible (Figure 1.2C), which ensures that the fit is only based on, and hence will only remove, artifactual components of recordings.

Using this new method for stimulus artifact removal, we have shown that there is a consistent pattern of evoked responses, with increasing consistency in subsequent responses within a burst. This phenomenon has not previously been reported for centrally recorded EPs, and suggests that the evoked response to short bursts of stimulation may be substantially different from the steady state response to prolonged stimulation. While our data do not provide a mechanism for this effect, the results are strongly reminiscent of what would be expected by progressive synchronization of a population of independent neural responses [40]. In other words, subsequent pulses may progressively recruit and align the phases of otherwise independent neural oscillators, and the increasing phase-locking with each stimulus would lead to increased consistency of the total evoked response.

Thus, the increasing correlation of the EPs throughout the burst may be a sign of the peripheral stimulations inducing progressive synchronization in thalamic nuclei. This phenomenon would be expected to cause a “synchronization blockade” in which the induced

regular firing of neural populations at high frequency would prevent propagation of the intrinsic pathological signals normally present in that population. Hence, while synchronized neural activity has been detected in movement disorders [49], [50], it is possible that artificial synchronization helps by "fighting fire with fire". For example, in the context of ET, artificially enhanced synchronization could prevent the tremor frequency from propagating, and could as such be responsible for the observed benefit of peripheral stimulation in recent studies [17], [18].

Regardless of the underlying mechanism, the synchronization of neural firing due to peripheral stimulation could at least partially mimic the synchronization of neural firing due to local DBS. This suggests potential efficacy of peripheral stimulation as a noninvasive treatment for movement disorders such as ET, Parkinson's disease, and dystonia, which would function at least in part by activation of the same treatment mechanism activated by invasive DBS.

1.6 Conclusion

Our novel decay artifact removal method has allowed us to demonstrate a previously unreported phenomenon: the progressive increase in consistency of thalamic evoked potentials in response to peripheral stimulation. While the understanding of this phenomenon may be important for elucidating network dynamics within the thalamus, it also provides a potentially noninvasive alternative to DBS for disorders that respond to electrical stimulation of thalamic nuclei.

CHAPTER 2: DEEP BRAIN STIMULATION REVEALS HIGH-PRECISION TEMPORAL CODING IN BASAL GANGLIA AND THALAMUS

This chapter presents my novel findings of high-frequency evoked potentials (HFEPs; including components with frequencies in the multiple kHz range) in the human brain, lists the numerous methods that were conducted to confirm the neural basis of these HFEPs, and explains why these findings highlight the importance of using high-impedance electrodes to record high-fidelity neural activity. My contributions to this project included investigation, data curation, software, formal analysis, validation, writing (original draft as well as review and editing), and visualization [37].

2.1 Abstract

Background: Deep brain stimulation (DBS) is an emerging treatment for movement disorders, including dystonia. However, the mechanism of DBS, like that of dystonia itself, remains largely unexplained. *Objective:* The objective of this study was to investigate neural responses to DBS in patients with movement disorders by characterizing the frequency components recorded from both low- and high-impedance contacts. The latter provide significantly greater bandwidth than conventional low-impedance DBS contacts, presenting a unique opportunity to record high-frequency brain activity. *Methods:* Externalized depth electrodes consisting of both low- (1-5 kOhm) and high-impedance (70-90 kOhm) contacts were implanted bilaterally in thalamic nuclei and basal ganglia in 11 pediatric patients with movement disorders. Stimulations consisting of 90-us, 3-V pulses were delivered at frequencies ranging from 9-250 Hz through conventional low-impedance DBS contacts while simultaneously recording from all other contacts. Evoked

potentials (EPs) from low- and high-impedance contacts were analyzed and compared in the frequency domain. *Results:* Novel high-frequency evoked potentials (HFEPs), consisting of frequency components up to 6 kHz, were detected in high-impedance contact recordings from thalamus and/or basal ganglia in all subjects. Conventional low-impedance contacts were unable to record these HFEPs, which stand in stark contrast to the more common 1-2-kHz DBS EPs. *Conclusions:* High-impedance recordings are required to detect high-frequency neural activity, which may be the result of local resonant circuits or synchronization of multiple axons. Regardless of the underlying mechanism, this work shows a level of complexity of the human brain's response to DBS that has not yet been reported elsewhere.

2.2 Introduction

While many different designs exist [12], DBS leads are typically made up of large cylindrical contacts (on the order of millimeters) distributed along a lead with diameter of 1 mm or more. The use of depth electrodes designed for sEEG allows for greater variation in the type and location of contacts for recording, including not only large cylindrical contacts, but also smaller microwire contacts at multiple locations around the lead. The larger, low-impedance "macro-contacts" on DBS and sEEG leads are used for stimulation, whereas both sizes, including the smaller, high-impedance "micro-contacts", can be used for recording. While computational studies have elucidated the effect of contact size and shape on neural selectivity [51], [52], the differences in in-vivo neural recordings as a function of depth electrode characteristics have not been widely investigated.

Since electrode contact area is directly proportional to capacitance but inversely proportional to resistance, larger contacts exhibit lower resistance and higher capacitance at the

electrode-tissue interface, creating low-pass filter properties [53]. In contrast, smaller contacts exhibit a higher low-pass cut-off frequency and can, as such, record higher frequency components of neural activity. This is similar to the expansion of usable bandwidth when small contact sizes are used for cortical surface recording [53].

Since larger contacts on the order of millimeters are conventional for DBS stimulation and recording [44], [48], [54], [55], potentially vital high-frequency neural information may be lost in many deep brain recording applications. Hence, the aim of this study was not only to investigate the neural responses to DBS in children with dystonia, but also to analyze and compare the frequency components of evoked potentials (EPs) recorded from high-impedance and conventional low-impedance DBS electrode contacts through frequency domain analysis.

2.3 Materials & methods

2.3.1 Patient selection

Study data were collected from 11 pediatric patients (8 male, 3 female, 10-16 years old, median age: 13) with movement disorders, predominantly dystonia (Table 2.1).

Table 2.1. Demographic characteristics of the 11 subjects included in the HFEP study. Unless otherwise noted, leads were implanted bilaterally.

Subject	Etiology	Characteristics	Gender	Age [yrs]	Implanted regions
1	Unknown (possibly vasculitic)	Left hemidystonia	M	15	Left: GPi, Voa/Vop, VIM, VPL
2	Cerebral Palsy	Dystonia	F	16	GPi, Voa/Vop, VIM, VA
3	Lesch Nyhan	Dystonia	M	14	GPi, Voa/Vop, VIM, STN, CMP, NA
4	Tourette	Motor and verbal tics	M	15	GPi, Voa/Vop, VIM, STN, CMP, NA
5	Huntington's disease	Dystonia	M	12	GPi, Voa/Vop, VIM, VA, STN
6	Cerebral palsy	Dystonia	F	12	GPi, Voa/Vop, VIM, VA
7	DYT1 (genetic)	Dystonia	F	16	VIM, Voa/Vop, STN, VA; Right: GPi
8	H-ABC (genetic)	Dystonia, weakness, ataxia	M	13	GPi, Voa/Vop, VIM, STN
9	Dyskinetic cerebral palsy	Hyperkinetic dystonia	M	12	GPi, Voa/Vop, VIM, VA, STN
10	GA1 (genetic)	Hypertonic dystonia	M	13	GPi, Voa/Vop, VIM, VA, STN
11	MEPAN (genetic)	Hyperkinetic (some hypertonic) dystonia, dyskinesia, spasticity	M	10	GPi, Voa/Vop, VIM, VA, STN

Abbreviations: F, female; M, male; yrs, years; CMP, centromedian parafascicular complex; GPi, globus pallidus internus; NA, nucleus accumbens; STN, subthalamic nucleus; VA, ventral anterior; VIM, ventral intermediate; Voa/Vop, ventral oralis anterior/posterior; VPL, ventral posterolateral.

2.3.2 Stimulation protocol

Stimulation frequencies ranged from 9-250 Hz through leads implanted in the basal ganglia and thalamic nuclei, as described prior under General Methods.

2.3.3 Data analysis

Both cathodic and anodic stimulations were used to generate a “polarity-reversed average” with reduced stimulus and decay artifacts (Figure 2.1) [56]. Neural activity was measured as the

relative response between two nearby micro- or macro-contacts, with each local bipolar recording on each lead visually investigated for the existence of an EP.

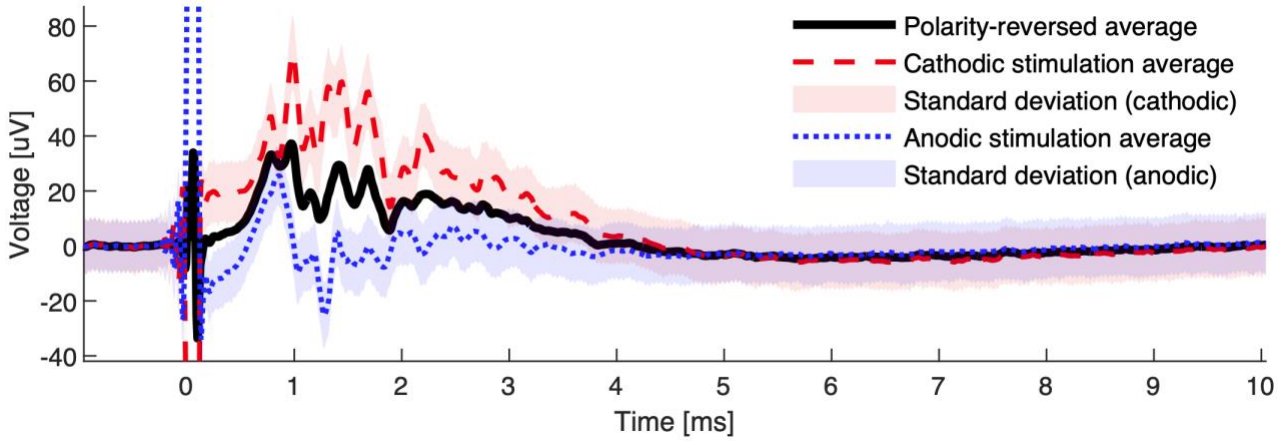

Figure 2.1. Representative image of polarity reversal from a bipolar micro-contact recording in Voa/Vop during GPi stimulation. Reversing the polarity of the pair of stimulating contacts by performing both "cathodic" (dashed red line) and "anodic" (dotted blue line) stimulation allows for off-line artifact reduction through averaging of the two signals (thick black line). Such a polarity reversal reverses the sign of the stimulus artifact, but not the neural response. This technique reduces the stimulus artifact (peaking around 0 ms, but decaying through approximately the 5-ms mark) while leaving the EP (between 0.5-4 ms in this example) intact, which in turn increases confidence that the observed EP is of neural origin, and not artifactual.

2.3.4 Analytical methods

Spectrogram time-frequency analyses of the polarity-reversed averages were generated using a short-time Fourier transform with frequency resolution of 400 Hz, normalized by the baseline power in each frequency bin. The power in each frequency bin was then averaged over all time points to obtain the overall power spectral density (PSD) of the recording. Statistical analyses comparing band powers between EPs were conducted using the non-parametric Wilcoxon signed-

rank test (after failing the normality assumption based on the Lilliefors test). The significance threshold was set to 0.05.

A peak analysis was also conducted to investigate the consistency of EP peaks across individual recordings. The MATLAB function *findpeaks* detected peaks within each of the 1000 individual stimulation segments with a minimum prominence equal to half the standard deviation of each segment. Indices where peaks were frequently detected – more often than twice the standard deviation of the peak occurrences at all indices – were noted and compared to the peaks of the stimulus-averaged response.

2.4 Results

2.4.1 High-frequency evoked potentials

Neural responses were recorded in all 11 subjects. While some consisted of the commonly observed 1-2-kHz DBS EPs, other novel *high-frequency evoked potentials (HFEPs)* were detected as well. In contrast to common DBS EPs, HFEPs consisted of multiple higher-frequency oscillations, with examples displaying significantly higher band power in the 2-6-kHz range (Figure 2.2). HFEPs were detected in all patients from at least one of the recorded regions: Voa/Vop, VA, VPL, VIM, GPi, and STN.

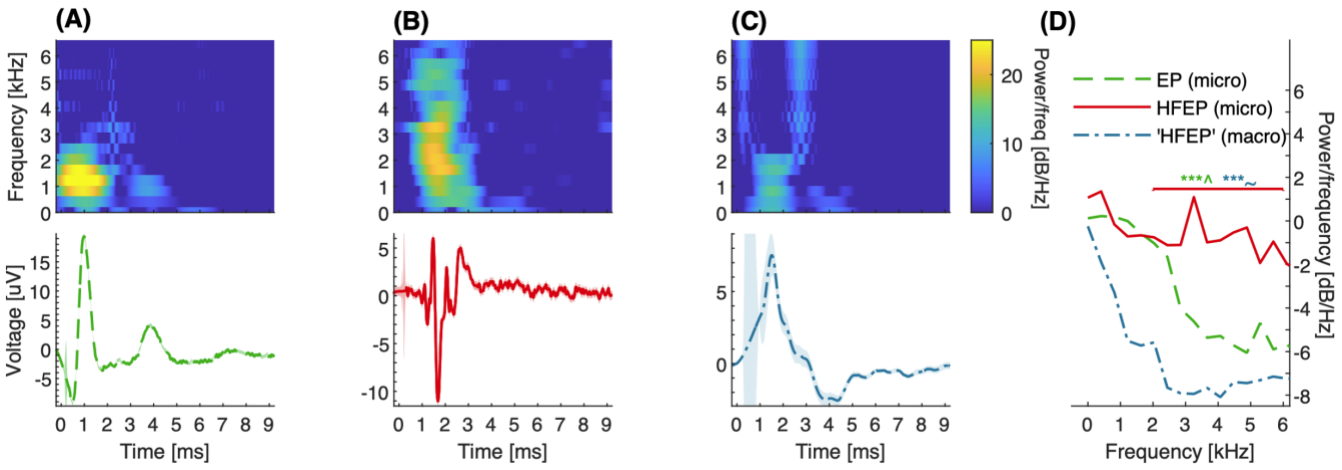

Figure 2.2. Frequency analysis comparison of low- vs. high-frequency EPs, recorded from micro-contacts, and an equivalent "HFEP" recording from macro-contacts. Spectrograms (top row) display the frequency components in the polarity-reversed averages (bottom row) of three EP examples, gathered simultaneously from one subject during STN stimulation: (A) a "regular" low-frequency EP, detected through micro-contacts in GPi; (B) a novel HFEP, detected through micro-contacts in VIM, and (C) a corresponding macro-contact recording from the same VIM lead, unable to detect the high-frequency components of the HFEP displayed in part B. The resultant PSDs are shown in plot D, additionally denoting the statistically higher power in the 2-6-kHz high-frequency band (solid red line) of the HFEP, when compared to both the regular EP (^, green dashed line) and the macro-contact recording (~, blue dash-dotted line); ***, $p < .001$. Spectrograms and PSDs denote power relative to baseline at each measured frequency band. Shading displays standard error of the mean of the segments averaged to generate the solid lines in the bottom row of plots A-C. Stimulation artifacts around 0 ms have been blanked and interpolated for visualization purposes.

2.4.2 Neural basis of high-frequency evoked potentials

Experimental artifact reduction and analytical checks highlighted the strong likelihood of a neural basis for the observed HFEPs. First, the experimental polarity reversal successfully reduced stimulus artifacts, while leaving the EP intact, as expected for a neural response (Figure 2.1). Second, stimulations at different frequencies as well as stimulations and recordings through different contacts generated similar but slightly varying responses, conforming to the inherent

neural variability expected of EPs and differing from the anticipated replicability of artificial electrical stimulus artifacts (Figure 2.3). Finally, the high-frequency peaks seen in the average response were also consistent in individual recordings (Figure 2.4A). This alignment of common peak indices over the peaks of the average response emphasizes the consistency of the characteristic HFEP shape across individual recordings, ruling out the possibility that the stimulation-averaged EP shape was merely generated by noisy samples. In contrast, the regular low-frequency EPs were not found to have such consistent peaks in the individual recordings (Figure 2.4B).

In addition to these checks, the timing of the EPs, with most peaking between 0.5 and 2 ms, met the expected timing for neural responses and was much later than the main stimulus artifact, which typically only lasted 0.3 ms or less in the micro-contact recordings.

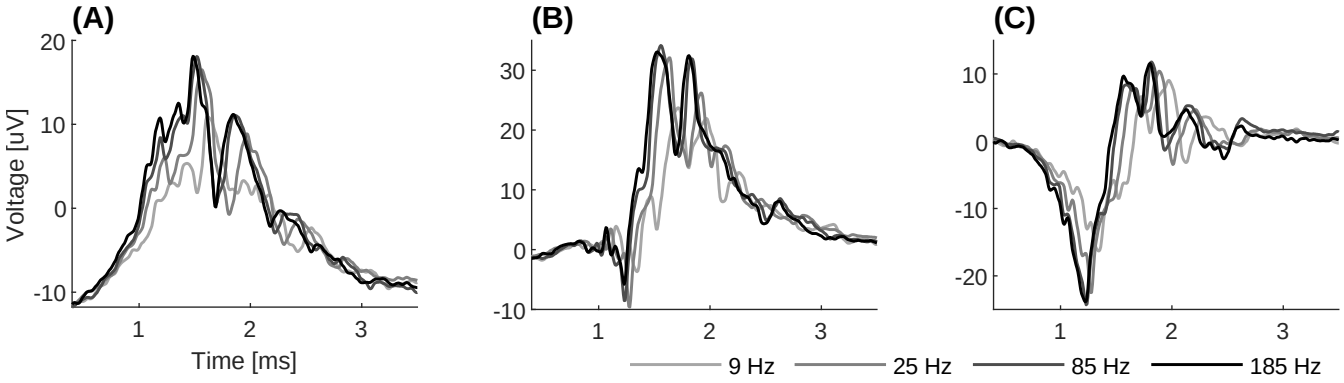

Figure 2.3. Comparisons of high-frequency evoked potentials (HFEPs) recorded from nearby micro-contacts. These example recordings are from three different contact pairs (A, B, C) recording from GPi during stimulation in Voa/Vop at varying frequencies (gray tracings), in one subject. Note that the HFEPs are consistent between stimulation frequencies, with only subtle differences, and exist in multiple nearby bipolar micro-contact recordings. This corroborates that the HFEPs are not artifactual, but rather generated by highly consistent neural activity.

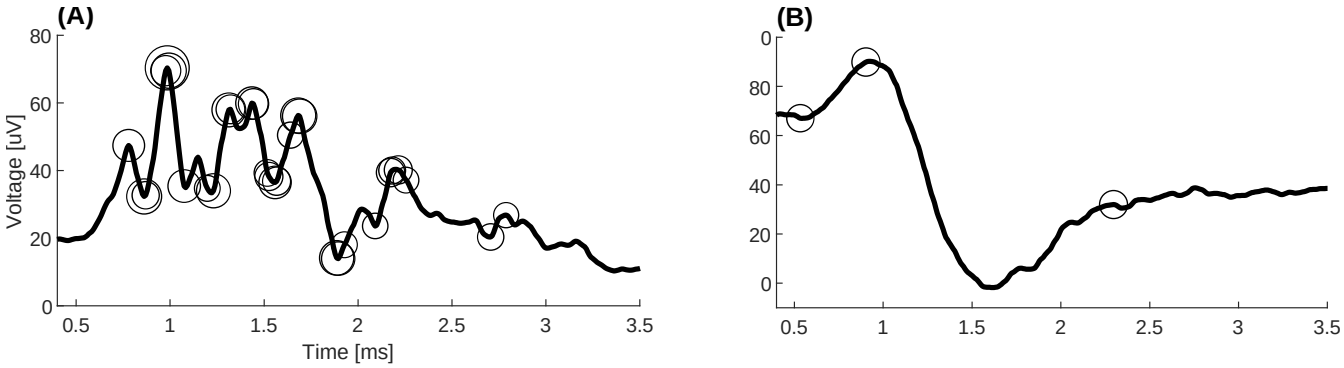

Figure 2.4. Representative peak analysis of individual recordings compared to overall stimulus-averaged response. Examples show an HFEP in Voa/Vop (A) and a "regular" EP in VIM (B), simultaneously recorded from micro-contacts during cathodic GPi stimulation. Circles mark indices where peaks were commonly detected, over the time-locked average response (line). The size of each circle corresponds to the number of times a peak was found at this index out of the 1000 segments that were averaged to create the above traces.

2.4.3 High- vs. low-impedance contact recordings

Comparisons of recordings from the high-impedance micro-contacts and low-impedance macro-contacts confirmed our hypothesis that macro-contacts are unable to record the HFEPs seen in micro-contact recordings. The frequency analysis highlighted the variation in frequency components, particularly in the high-frequency band (2-6 kHz), in which a representative macro-contact example had significantly lower power than the corresponding micro-contact recording (Figure 2.2). Moreover, the macro-contact recordings were found to contain significantly longer stimulus artifacts and artifact tails, further distorting any underlying neural activity (Figure 2.5).

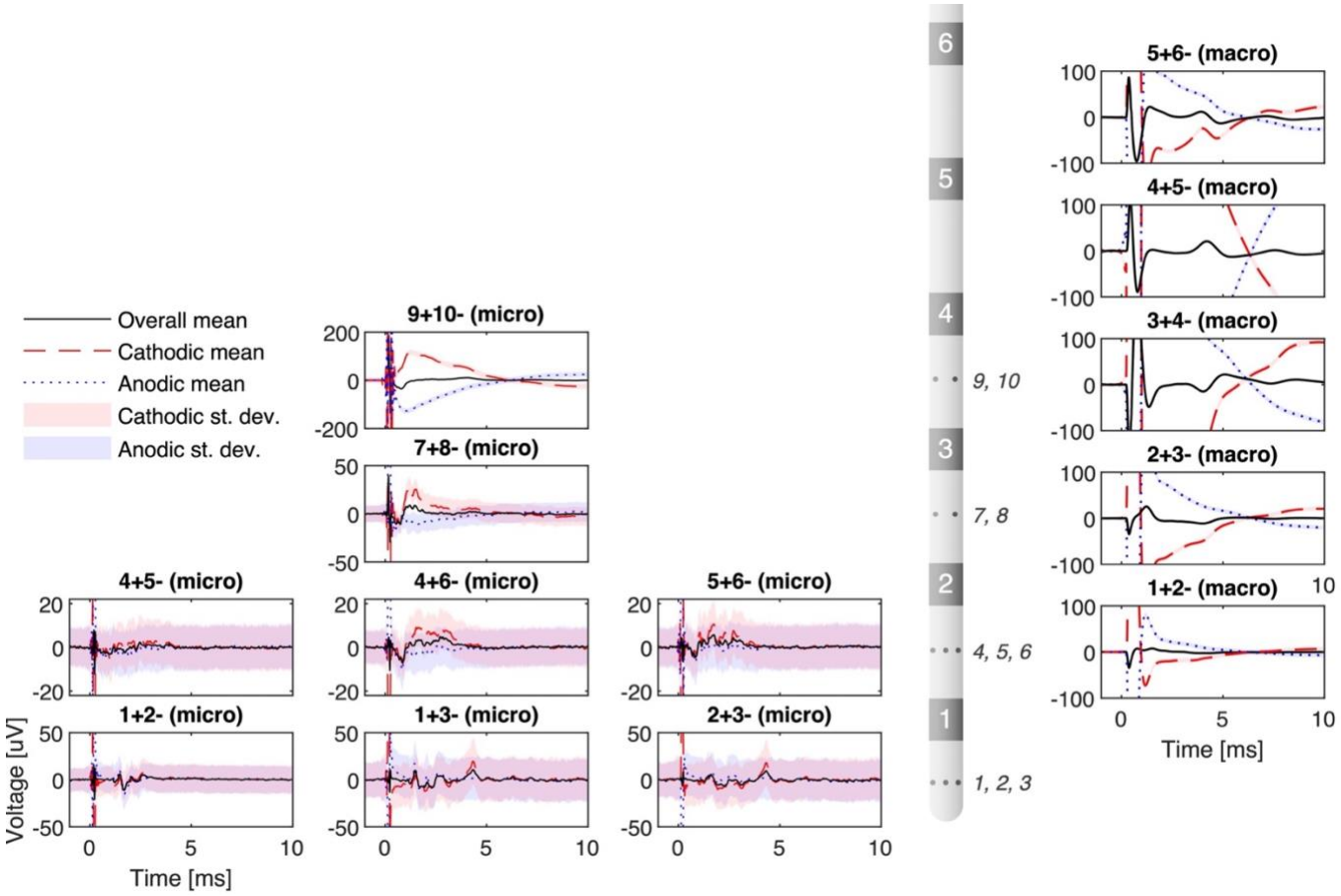

Figure 2.5. Representative comparison of micro-contact (left) and macro-contact recordings (right) in VIM during STN stimulation. The plots to the left of the lead diagram display bipolar recordings from high-impedance micro-contacts (small circles on lead, numbered to the side), while the plots to the right display bipolar recordings from low-impedance macro-contacts (numbered rectangles on lead). The location of the plots in the figure relate to their recording location with respect to the lead diagram, i.e., each row shows recordings from approximately the same region. *Black solid lines: polarity-reversed average; red dashed lines: cathodic stimulation average; blue dotted lines: anodic stimulation average; shadings: standard deviation.*

2.5 Discussion

While DBS EPs with frequencies up to 1-2 kHz are common and have been published elsewhere [55], the HFEPs presented in this paper, with clear frequency components up to 6 kHz, have not

previously been reported. Other reports of "high-frequency oscillations" (HFOs) in deep brain nuclei during DBS have rather referred to frequencies in the range of *hundreds* of Hz [57]. While the shape and extended duration of some of the HFEPs resemble "very fast oscillations" (VFOs) recorded in deep brain regions during peripheral nerve stimulation (Figure 1.2 A & C, Chapter 1), the frequencies of such responses have only been reported up to 1.5 kHz [36], [40], which is still lower than the frequency components of the HFEPs described here.

While further studies are required to determine the origin of the observed HFEPs, plausible mechanisms for such high-precision temporal neural coding include local resonant circuits or multiple axons firing with different yet precise delays. The presence of HFEPs is surprising, because high-frequency components of the response would be expected to "average out", due to temporal variation when averaging the response to multiple stimuli, as well as the staggered timing of responses among a large neuronal population. Preservation of these components hence demonstrates highly consistent temporal patterns of responses and neural synchronization. Future work would involve incorporating an automatic method for the detection of HFEPs, which would allow for precise group analyses to determine any potential associations between HFEPs and variables such as stimulus frequency and voltage, stimulation and recording region, movement disorder etiology, and clinical efficacy.

Since electrode contact area is directly proportional to capacitance but inversely proportional to resistance [53], the macro-contacts' lower resistance (1-5 kOhm) and higher capacitance at the electrode-tissue interface create low-pass filter properties [53] that provide usable data only up to a few hundred Hz. In contrast, the micro-contacts on the Ad-Tech MM16C depth electrodes (50-μm microwires with 70-90-kOhm resistance) exhibited a higher cut-off frequency, which allowed us to record usable data up to at least 6 kHz. Similarly, the higher

capacitance at the macro-contact tissue interface could also explain the longer stimulus and decay artifacts that distorted the macro-contact recordings.

Our findings not only show the complexity of DBS-induced neural activity, but also emphasize the importance of using high-impedance contacts to detect this full range of evoked brain activity.

2.6 Conclusion

The HFEPs identified in this study may inform conceptualization of the response to DBS, which is typically understood in terms of the magnitude of the effect on the target. Our use of low- as well as high-impedance electrode contacts allowed for precise analysis of the DBS response pattern. The results indicate that temporal factors could also contribute to the clinical response to DBS. Further investigation is warranted, in order to determine the origin of this high-precision temporal neural coding as well as its potential association with stimulus frequency, location, voltage, and clinical efficacy.

Ultimately, the existence of the observed HFEPs emphasizes the complexity of the brain's response to repetitive DBS, and aids in elucidating the mechanisms of DBS as well as the underlying movement disorder. Our results provide further support for the importance of high-impedance sEEG depth electrode recordings in understanding and improving the clinical efficacy of DBS treatment for childhood dystonia and other movement disorders.

CHAPTER 3: AN ALGORITHM FOR AUTOMATED DETECTION OF EVOKED POTENTIALS FROM POLARITY REVERSED ELECTRICAL STIMULATION

This chapter outlines the algorithm I developed to automate the detection of evoked potentials when polarity-reversed electrical stimulation can be incorporated. It uses correlation to separate neural responses from artifacts and noise, thereby reducing human bias and saving substantial time for the researcher. My contributions to this project included conceptualization, methodology, investigation, data curation, software, formal analysis, validation, writing (original draft as well as review and editing), and visualization [37].

3.1 Abstract

Background. In neurophysiological research involving neural responses to electrical stimuli, each recording must be searched for evoked potentials (EPs) prior to further analysis. Conducting this process manually is time consuming for the researcher, and also inserts bias. However, automated detection methods often struggle to distinguish between artifacts and neural responses, which can have highly complex and varying shapes. *Methods.* I have developed a novel algorithm for automated detection of polarity reversed EPs (ADPREP), which uses the knowledge that reversing the polarity of a pair of stimulating contacts reverses the sign of the stimulus artifact, but not the sign of the neural response. Hence, our algorithm searches for any positive correlation between the recordings from two polarity reversed stimulations, after removing any stimulus decay artifacts. If the peak-to-peak amplitude (P2P) in a positively correlated region surpasses a user-defined threshold, the recording is labeled as an EP; otherwise, it is not. Neural recordings from deep brain nuclei and cortical regions during deep brain stimulation (DBS) in 28 pediatric patients

with dystonia were used to test and prove the validity of the method. *Results.* The ADPREP algorithm is able to distinguish EPs of varying shapes and sizes with a high level of accuracy, as early as 0.35 ms after stimulation, despite large stimulus artifacts. The algorithm has proven useful in initial tests with DBS data in hundreds of stimulation/recording combinations within the basal ganglia and thalamic nuclei, during stimulation frequencies up to 250 Hz. *Conclusion.* Our automated EP detection algorithm can accurately detect DBS EPs in deep brain nuclei, and has promising applications in other stimulation and recording modalities that allow for polarity reversal of the recorded stimulus artifact. The algorithm successfully labels EPs of varying shapes and sizes, as early as a fraction of a millisecond after stimulation, in a range of stimulus frequencies and stimulation-recording pairs – even under large stimulus decay artifacts and in same-lead recordings. As such, it has the ability to improve efficacy and minimize human bias, setting up for more reliable conclusions to be drawn from the data.

3.2 Introduction

When DBS is used in combination with externalized depth electrodes, which can both stimulate and record, valuable insight can be obtained into the EPs that represent the brain's neural responses to electrical stimulation [20], [58], [59]. However, with the numerous combinations of possible stimulation and recording locations, stimulation pattern and frequency, and other parameters, thousands of connections and conditions can be studied – all of which must be searched for EPs prior to further analysis and conclusions. Conducting this process manually is time consuming for the researcher, and also inserts bias. Automated detection methods often struggle to distinguish between artifacts and neural responses, which can have highly complex and varying shapes (as shown in Chapter 2).

One experimental approach to distinguishing stimulus artifacts from neural responses is the use of polarity-reversed stimulations, wherein electrical stimulation is performed through a pair of contacts (A & B) in both polarities: with A as the cathode and B as the anode ("cathodic stimulation"), and vice versa ("anodic stimulation") [59], [60]. The method is useful because flipping the cathodic and anodic stimulation contacts reverses the sign of the stimulus artifact, but not the neural response [60]; hence, neural responses are expected to positively correlate between the cathodic and anodic recordings, while artifactual components would correlate negatively, or not at all.

I have developed a novel algorithm for automated detection of polarity reversed EPs (ADPREP). This method uses the prior knowledge that in a pair of recordings during polarity reversed (cathodic and anodic) stimulations, neural responses would show up as positive correlations between the cathodic and anodic recordings, after removal of stimulus artifacts. Hence, the ADPREP method starts by detecting and removing decay artifacts after the main stimulus artifact by fitting a sum of two exponential decays to each of the recordings during the two polarity-reversed stimulation types. If a significantly positive correlation is found between the resulting artifact-reduced cathodic and anodic recordings, and the amplitude of the resulting average response in this correlated region is greater than a user-defined threshold, the recording is labeled as an EP; otherwise, it is not. The EPs can thereafter be characterized by features such as their peak-to-peak amplitude (P2P), time-to-(first-)peak delay (T2P), frequency components, and more.

Initial results are promising, proving the ADPREP algorithm's ability to distinguish EPs of many varying shapes and sizes from stimulus artifacts and other noise in the recordings, saving time for the user and minimizing human bias. One of the benefits of this method is that it does not

require the shape of the EP to be predefined; because of this, the algorithm does not discriminate towards or against any EP shapes. Another benefit is the user-defined variables, which can be adjusted to match the need of the researcher or project; e.g., the amplitude threshold can be lowered or raised to reduce the false negative or false positive rates of EP detection, respectively.

3.3 Materials & methods

The main inputs to the ADPREP method are recordings obtained during polarity reversed stimulations, from electrodes situated close enough to the stimulating electrode pair to experience a reversal of the stimulus artifact between the two stimulation types (cathodic and anodic). The algorithm, which is outlined in Figure 3.1, starts by removing any decay artifact after the stimulus artifact in each of the two recordings. Next, the correlation between the resulting artifact-reduced cathodic and anodic recordings is evaluated using moving correlation windows. If a significantly positive correlation is detected above a user-defined threshold, the average response between the cathodic & anodic recordings is obtained, and the highest P2P amplitude within the significantly positive correlation regions is determined. Finally, if this P2P amplitude surpasses an empirically chosen threshold, the average recording is labeled as an EP; otherwise, it is not.

For a full list of the parameter values, initial conditions, and other restrictions used in our dataset, see Table 3.1 & Table 3.2.

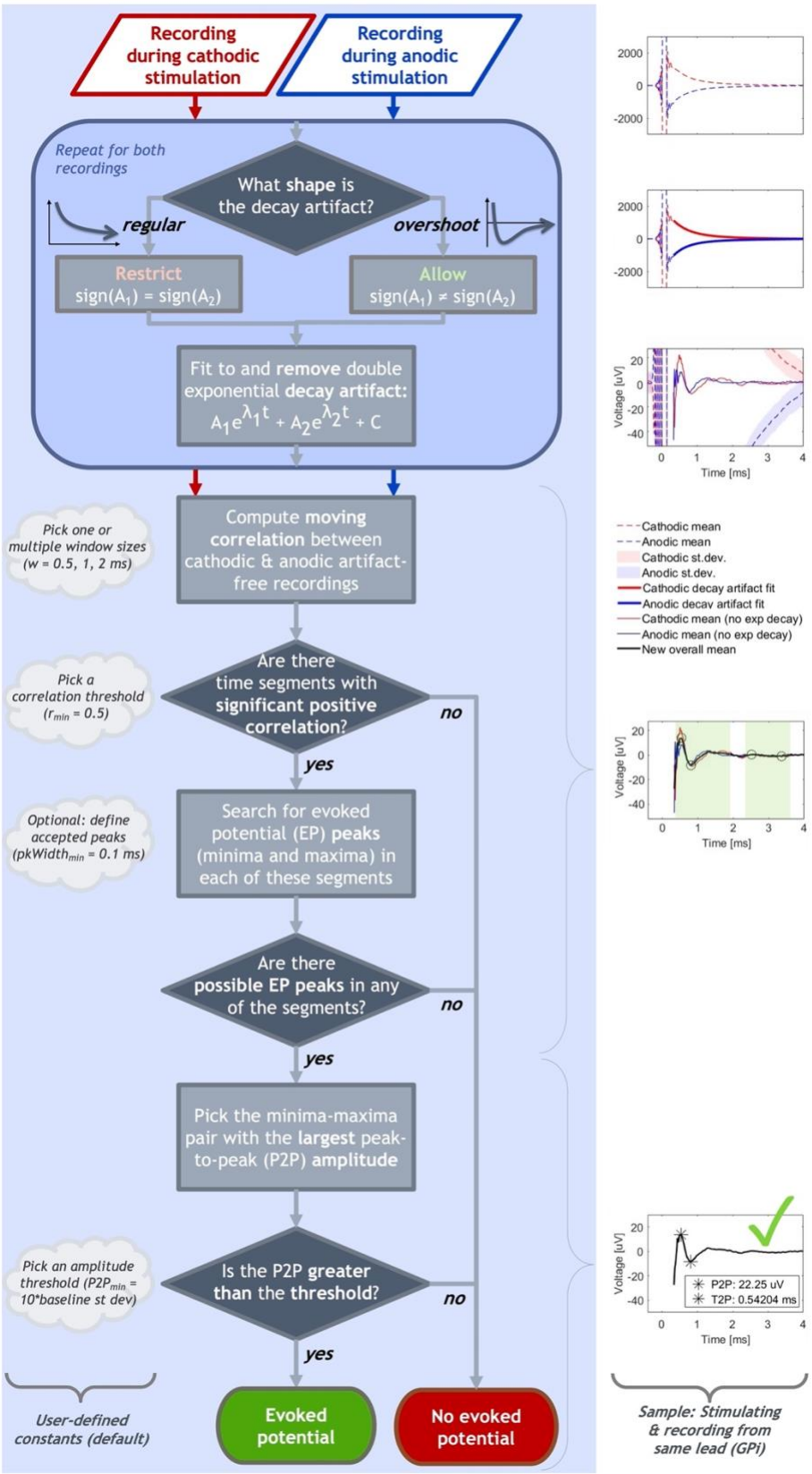

Figure 3.1. Flowchart of the ADPREP algorithm (left) with examples visualizing the main steps (right).

Table 3.1. ADPREP parameter values used for the dataset presented in this chapter.

Parameter	Description	Unit	Our value(s)
w	Moving correlation window size(s)	ms	[0.5, 1, 2]
r_{min}	Correlation threshold (minimum)	-	0.5
A_{min}	Amplitude threshold (minimum)	μV	10x baselineStd*

**We defined our "baseline standard deviation" (baselineStd) as the standard deviation of the detrended average signal of the cathodic & anodic stimulus-triggered averages from 1.4 to 0.3 ms before the stimulus artifact.*

Table 3.2. SEDAM parameter initial values, lower bounds, and upper bounds used for the dataset presented in this chapter. Italicized brackets contain the values when the decay artifact fit is forced to be a "simple" exponential, by making the amplitudes of the exponential decays have the same sign (note that $sign(A_1)$ is multiplied by A_2 in this restricted case to force this relationship). Otherwise, the values chosen are the same for both the restricted (forced "simple" exponential decay model) and unrestricted cases (both "simple" and "overshoot" exponential decays allowed).

Para-meter	Description	Unit	Initial value	Lower bound	Upper bound
A_1	Amplitude of exponential decay 1	μV	AMDS*sign(dataSeg(ind_{ADMS}))	-4*AMDS *[-2*AMDS]*	4*AMDS *[2*AMDS]*
A_2	Amplitude of exponential decay 2	μV	-AMDS*sign(dataSeg(ind_{ADMS})) *[AMDS]*	-4*AMDS *[0]*	4*AMDS *[2*AMDS]*
λ_1	Time constant of exponential decay 1	1/ms	-5	-12	-0.01
λ_2	Time constant of exponential decay 2	1/ms	-1	-12	-0.01
C	Baseline offset	μV	dataSeg(end)	-abs(dataSeg(end))	abs(dataSeg(end))

Abbreviations & variables: abs, absolute value; AMDS, absolute max of the data segment (dataSeg); dataSeg, data segment used to fit (and remove) decay artifact and subsequently search for an EP; end, last index in segment; ind_{ADMS}, index where AMDS occurs.

3.3.1 Data validity

To ensure the validity of the assumptions of the polarity reversal approach used in this algorithm, the neurophysiological recordings must be obtained from electrodes situated close enough to the stimulating electrode pair to experience a reversal of the stimulus artifact between the two stimulation types (cathodic and anodic). Examples of such valid recording & stimulation combinations include recording from deep brain nuclei (e.g., using sEEG) or cortical regions (e.g., using electroencephalography, EEG) during simultaneous deep brain stimulation. Examples from the former are presented in this chapter.

Note that if the recorded data's signal-to-noise ratio is acceptable, single trial recordings may be used. Otherwise, stimulus-triggered averaging can be implemented to increase SNR prior to using the ADPREP algorithm.

3.3.2 Decay artifact removal

The polarity reversal approach builds on the assumption that when the polarity of the stimulating contact pair is switched, the polarity of the stimulus artifact is reversed, whereas that of the neural response is not. While the main stimulus artifact can be relatively brief and return to baseline prior to the start of the evoked response, so-called decay artifacts may extend for a longer period, distorting the neural response [36], [45], [61]. Just like the main stimulus artifact, the polarity of the decay artifact depends on the polarity of the stimulation. Because of these opposing polarities of the decay artifacts from the polarity reversed stimulations, they can make the correlation between the cathodic and anodic recordings seem non-significant or negative, even if there is an underlying neural response that is common to both recordings. Therefore, these decay artifacts must be removed prior to the ADPREP algorithm's correlation analysis.

The decay artifact removal is based on an approach that fits the data to the sum of two double exponentials (as previously presented in Chapter 1) [36]:

$$A_1 e^{\lambda_1 t} + A_2 e^{\lambda_2 t} + C \tag{3.1}$$

where A_1 and A_2 are the amplitudes and λ_1 and λ_2 the decay constants of the two exponential components, and C is the baseline offset.

In our data, we have encountered not only "regular" exponential decay artifacts, which decay towards 0 without crossing the x-axis, but also decay artifacts that "overshoot" the x-axis before stabilizing back to baseline (Figure 3.1, top). The SEDAM model (Equation 3.1) can model both these types of decay artifacts: when $sign(A_1) = sign(A_2)$, the resulting SEDAM decay artifact is "regular", whereas when $sign(A_1) \neq sign(A_2)$, an "overshoot" decay artifact is modeled. However, due to the regression's high sensitivity to the initial values of A_1 and A_2, two separate iterations of the regression are run. First, the initial values of A_1 and A_2 have the same sign, and the upper and lower boundaries of the coefficients are chosen to force $sign(A_1) = sign(A_2)$. In the second iteration, the initial values of A_1 and A_2 are of opposite signs, and the relation between the signs of A_1 and A_2 is not restricted (i.e., $sign(A_1) \neq sign(A_2)$ and $sign(A_1) = sign(A_2)$ are both allowed). The parameters from the regression that generated the best fit (defined by the R^2 value) are used to model the decay artifact and subtract it from the recording.

This process is repeated for both the cathodic and anodic signals, to generate artifact-reduced recordings for use in the subsequent steps of the ADPREP algorithm.

3.3.3 Moving correlation

After decay artifact removal, the artifact-reduced post-stimulation recordings are used to determine the correlation between the cathodic and anodic signals. This main part of the ADPREP algorithm is built on the assumption that a neural response evoked by a stimulation of a pair of nearby contacts would be similarly elicited if the polarity of the stimulating contact pair was reversed (i.e., cathodic vs anodic stimulation). Hence, any neural response to the stimulation should display a significant positive correlation between the artifact-reduced polarity reversed recordings.

Since neural responses can be brief and may not span the whole recording, *moving* correlation is required (as opposed to determining the correlation between the signals over the entire recording). We use the MATLAB File Exchange function *movcorr* [62] to calculate the correlation between the artifact-reduced cathodic and anodic recordings over time; in a similar manner to moving average, it calculates the Pearson correlation in a user-defined window at each point as it moves over the x-axis, one sample at a time. This allows us to find local correlations that may be representative of neural responses evoked by the electrical stimulation.

As neural responses can have varying frequencies, the width of the moving correlation window should be adjusted accordingly. The ADPREP algorithm allows for multiple user-defined window sizes, which should be selected based on expected frequency and duration of the neural response. The moving correlation is calculated over the recording after the stimulation, for each of the window sizes. The time regions that display significant positive correlation above a user-defined threshold of Pearson's *r* – using any or all of the window sizes – will be searched for possible EPs.

3.3.4 Peak detection and amplitude threshold

The possible EP regions located using the above methods are checked for EPs using the MATLAB *findpeaks* function. In the ADPREP algorithm, the function is simply used to find the positive and negative peaks with the largest and smallest values, respectively, in each potential EP region. Further *findpeaks* restrictions, such as *minPeakWidth* or *minPeakHeight*, are optional.

After finding the peaks in each possible EP region, the region with the greatest P2P amplitude is assumed to contain the (main) neural response. In the final step, the P2P amplitude is compared to a user-defined minimum amplitude threshold, which can be set to a firm value (e.g., 10 μV) or require a certain SNR (as in our sample dataset, Table 3.1). If the P2P surpasses the amplitude threshold, the located peaks are labeled as representative of an EP. However, if any of the above thresholds were not met, the recording is labeled as *not* containing an EP.

3.3.5 Sample data

The data used to develop the ADPREP algorithm and generate sample results for this chapter are bipolar recordings from sEEG micro-electrodes in deep brain structures (thalamus and basal ganglia) during DBS of thalamic or basal ganglia nuclei, from a total of 28 subjects.

3.4 Results

The ADPREP algorithm can distinguish EPs of varying shapes and sizes with a high level of accuracy, as early as 0.35 ms after stimulation, despite large stimulus artifacts (even in same-lead stimulation & recordings). The algorithm has proven useful in its initial tests during DBS in hundreds of stimulation/recording combinations within the basal ganglia and thalamic nuclei (sEEG recordings), during stimulation frequencies up to 250 Hz, in 28 subjects to date. Sample

results are displayed in Figure 3.2, selected to show the wide range of EPs that the algorithm can detect (even under large decay artifacts) and exemplify rejected recordings that may have been labeled as EPs by methods that only use the cathodic and anodic signals independently, or the average between them.

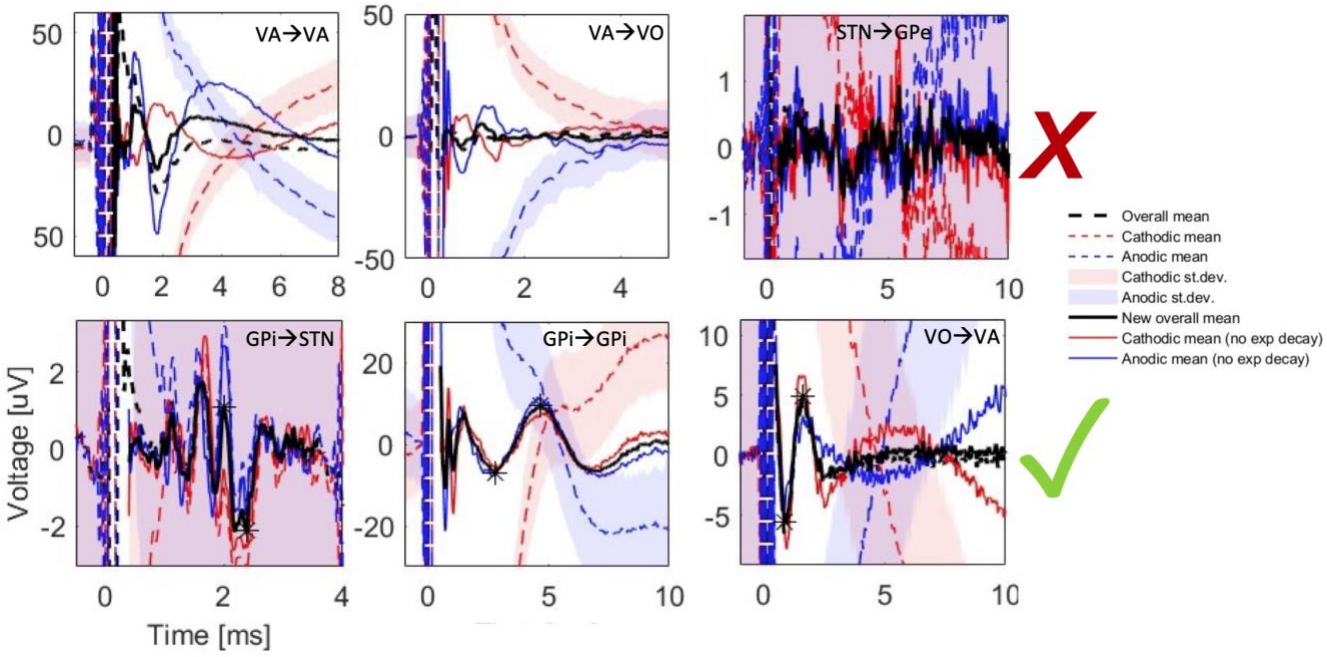

Figure 3.2. Examples of rejected and detected EPs using the ADPREP algorithm. The top and bottom rows show sample rejected and detected EPs, respectively, using the user-defined variables listed in Table 3.1 & Table 3.2. Dashed red and blue lines are stimulus-triggered averages of the cathodic and anodic stimulation types, respectively, with shaded standard deviations; dashed black lines are the average between the original cathodic and anodic signals. Similarly, solid red and blue lines are the signals after removal of decay artifacts, and solid black lines are the average between the decay artifact-reduced cathodic and anodic signals. Stars denote the detected positive and negative peaks of the labeled evoked potentials. All examples are taken from different subjects and stimulation/recording combinations, as denoted in the annotation in each subplot (stimulation→recording region). Y-axis: recorded voltage [μV]; x-axis: time after stimulation [ms].

3.5 Discussion

The benefits of the ADPREP algorithm compared to other EP detection methods are multifold. Firstly, the algorithm does not assume a specific EP waveform, which means it does not discriminate towards or against any particular shapes – any neural response that is common to both stimulation polarities can be labeled as an EP. Secondly, since the algorithm is simply based on correlation, it is potentially applicable to any kind of bipolar stimulation that allows for polarity reversal, when the recording electrodes are close enough to the stimulation electrodes to register the polarity reversal of the stimulus artifact (i.e., the ADPREP algorithm is not restricted deep brain recordings during DBS, the setup tested in this chapter). Thirdly, the user-defined constants and thresholds allow the user to tailor the algorithm to their particular application, e.g., by selecting the moving correlation window size(s) to match the frequency and duration of the expected EPs, or lowering or raising the amplitude threshold to reduce the false negative or false positive rates, respectively. Finally, the automated algorithm vastly improves efficacy and minimizes human bias by reducing the influence of the user, which sets each study up for more reliable further analysis.

As with any method, the ADPREP algorithm also comes with limitations. Firstly, because the cathode acts as the active electrode in the stimulating pair, and the anode as the returning electrode, the polarity reversal technique effectively leads to a slight shift in stimulation location, corresponding to the distance between the stimulated electrode pairs (5 mm, in our case of using the macro-contacts of the Ad-Tech MM16C sEEG leads). Therefore, the final averaged response of the two stimulation types is, in fact, an average of stimulations at two slightly different locations, which may lead to timing or amplitude differences between the two recordings. Furthermore, in its current version, the algorithm is designed to detect one EP per recording and stimulation, and

in the case of multiple possible EPs, the one with the largest P2P amplitude is selected. These assumptions could be addressed in future versions, e.g. by redefining how the algorithm should select between multiple possible EPs, and/or allowing for the labeling of more than one EP per recording. Moreover, while the method should work for any set of stimulating electrodes that allow for polarity reversal and with recording electrodes that are proximal enough to experience a reversed polarity of the stimulus artifact, it has so far only been tested in deep brain sEEG recordings during DBS. Tests with other stimulating and recording modalities, such as EEG, must be conducted before it can be conclusively stated which applications the ADPREP algorithm is compatible with.

3.6 Conclusion

Our algorithm for automated detection of polarity reversed evoked potentials (ADPREP) utilizes polarity reversal of the stimulating electrode pair to distinguish neural responses from stimulus artifacts and other noise. It has proven useful in detecting DBS EPs in deep brain nuclei (basal ganglia and thalamus) and has promising applications in other stimulation and recording modalities that allow for polarity reversal of the recorded stimulus artifact. While the algorithm can be further developed, e.g. to allow for detection of multiple EPs per recording, it has already proven successful in labeling EPs of varying shapes and sizes, as early as a fraction of a millisecond after stimulation, in a range of stimulus frequencies and stimulation-recording pairs in deep brain nuclei, in more than two dozen pediatric patients with dystonia – even under large stimulus decay artifacts and in same-lead recordings. As such, it is a valid option to improve efficacy and minimize human bias, setting up for more reliable analyses and conclusions from the datasets.

CHAPTER 4: INCREASED DEEP BRAIN STIMULATION FREQUENCY INCREASES DELAY, DECREASES AMPLITUDE, AND REDUCES HIGH-FREQUENCY COMPONENTS IN THALAMIC AND BASAL GANGLIA EVOKED POTENTIALS

This chapter presents preliminary findings of the effects of DBS frequency on EP delay, amplitude, and frequency components. My contributions to this project included investigation, data curation, software, formal analysis, validation, writing (original draft as well as review and editing), and visualization [37].

4.1 Abstract

Background. This study aimed to shed light on the mechanism of action of DBS as a treatment for dystonia by investigating the effect of DBS frequency on EPs recorded in deep brain structures of dystonic patients. *Methods.* Externalized sEEG leads were implanted bilaterally in 10 pediatric patients with dystonia selected for DBS treatment, with up to 6 leads per hemisphere placed in target areas in the thalamus and basal ganglia. Stimulations were administered at frequencies ranging from 9-250 Hz, while simultaneously recording from high-impedance micro-contacts, allowing us to detect high-frequency neural components in the kHz range. Each EP was characterized by its amplitude, delay, and frequency components, which were then compared between stimulation frequencies. *Results.* Preliminary results found stimulation frequency to be negatively correlated with EP amplitude and positively correlated with EP delay. Additionally, as stimulation frequency increased, high-frequency components of EPs seemed to reduce. *Discussion.* These trends of decreased amplitude, increased delay, and "low-pass filtering" of EPs at higher DBS frequencies may be related to refractory periods and oversaturation of neural receptors when

stimulations are delivered at shorter intervals. Group analyses should be conducted to confirm these preliminary results, along with developing qualitative and/or computational models to explain the neural mechanism behind these frequency dependencies. *Conclusion.* These findings will help shed light on the dystonic brain's frequency-dependent response to DBS and provide insight into how stimulation frequency can be used to generate wanted neural response patterns, to in turn elicit the most effective clinical response to DBS treatment.

4.2 Methods

Externalized sEEG leads were implanted bilaterally in 10 pediatric patients with dystonia selected for DBS treatment. Up to 6 leads per hemisphere were placed in target areas including the thalamus and basal ganglia. Stimulations ranging between 9 and 250 Hz were delivered through macro-contacts while simultaneously gathering neural recordings through high-impedance micro-contacts from all leads.

Each recording was visually investigated for the existence of an EP, which, if found, was characterized by its amplitude, delay, and frequency components. These characteristics were then compared between stimulation frequencies.

4.3 Results

Preliminary results alluded to a clear effect of stimulation frequency on EP delay, amplitude, and frequency components (Figure 4.1). Stimulation frequency was found to be negatively correlated with peak-to-peak EP amplitude, but positively correlated with delay (time to first peak) – that is, higher stimulation frequencies typically evoked smaller and more delayed neural responses.

Moreover, for high-frequency EPs (HFEPs), the higher-frequency components seemed to reduce at higher stimulation frequencies, inferring a possible cerebral "low-pass filtering" effect.

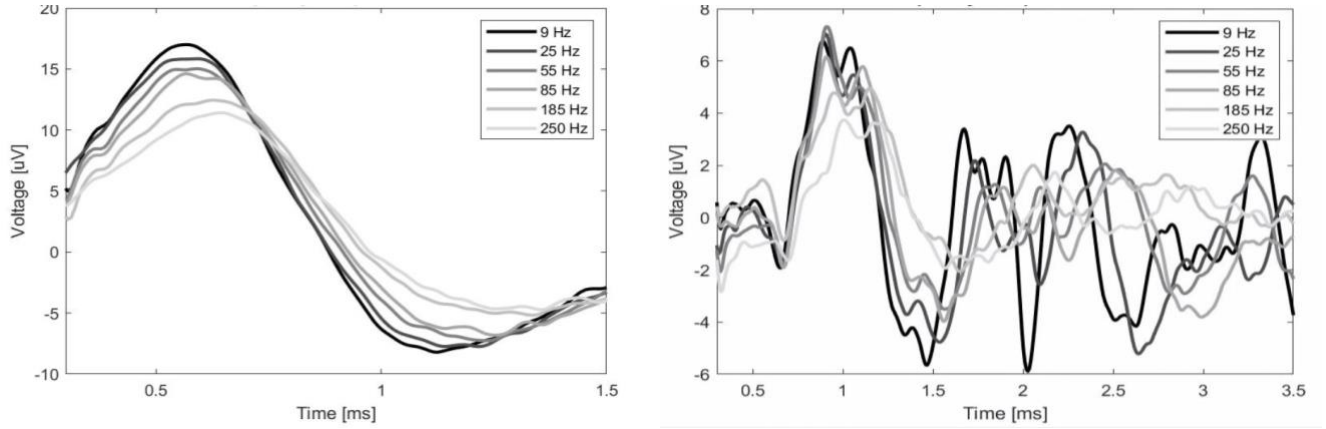

Figure 4.1. Example of the impact of stimulation frequency on EP delay and amplitude (left) and shape (right). The above figures show neural responses evoked by DBS at frequencies varying from 9-250 Hz (darker to lighter traces) in two different recording locations (left & right). The left plot is a clear example of the amplitude of the neural response decreasing, and the delay increasing, for higher stimulation frequencies. The right plot portrays the reduced EP amplitude and increased delay in the segment before 1.5 ms, but thereafter also exemplifies how higher-frequency EP components are sometimes suppressed at higher stimulation frequencies. *Y-axis: voltage [μV]; x-axis: time [ms] after stimulation (not shown).*

4.4 Discussion

This chapter reports novel findings in the relationship between DBS frequency and neural responses in patients being treated for movement disorders. Such an analysis has, to our knowledge, not been conducted previously.

These trends of decreased amplitude, increased delay, and "low-pass filtering" of EPs at higher DBS frequencies may be related to refractory periods and oversaturation of neural receptors when stimulations are delivered at shorter intervals. However, group analyses with

statistical tests must be conducted to confirm these preliminary results. Moreover, a multivariate regression study would be beneficial to determine whether these trends are more prominent in e.g. particular stimulation and/or recording regions, anti- or orthodromic connections, or certain subjects. Future work could also involve developing qualitative and/or computational models with the aim to explain the neural mechanism behind this frequency dependency. Another study of interest would involve comparing these frequency effects to our clinical stimulation data, to determine if there is any correlation between the DBS EPs at different frequencies and the most effective clinical frequency for each subject. This could be a potential first step in implementing neurophysiological findings to provide optimal DBS treatments for patients with movement disorders.

4.5 Summary & conclusion

We studied the effects of deep brain stimulation (DBS) frequency on evoked potential (EP) amplitude, delay, and frequency components in thalamus and basal ganglia in 10 pediatric patients with dystonia. Preliminary results show that increased stimulation frequency evokes smaller and more delayed neural responses, with diminished high-frequency components. These findings provide novel insight into how DBS pulse patterns affect the neural response, and will help improve our understanding of how to use stimulation frequency to generate wanted neural response patterns and elicit the most effective clinical response to DBS treatment.

CHAPTER 5: EFFECTS OF BENZODIAZEPINES ON DEEP BRAIN ACTIVITY AND DEEP BRAIN STIMULATION EVOKED POTENTIALS

This chapter presents preliminary findings of the effects of benzodiazepines on deep brain regions. It is based on a draft for a co-first-author publication, in which the contributions between us two first-authors were evenly split. My focus was on the effects of benzodiazepines on DBS EPs, while my co-author analyzed the local field potentials (LFPs) and wrote the parts of the paper not pertaining to the DBS EPs. My particular contributions included investigation, data curation, software, formal analysis, writing (part of the original draft as well as review and editing), and visualization [37].

5.1 Abstract

Background. Dystonia is a movement disorder in which intermittent or sustained muscle contractions cause repetitive movements and abnormal postures. Benzodiazepines (BZD) are commonly used to treat these symptoms in combination with other pharmacotherapy by increasing inhibition at GABA receptors. When medications alone do not reach the desired clinical effect, DBS is another treatment method that delivers electrical pulses into regions in the motor pathways. While many studies have investigated the effects of benzodiazepines on cortical activity, no data is currently available on its effects on deep brain regions, nor on these regions' responses to DBS. Hence, we asked: Do benzodiazepines have a significant impact on deep brain regions? *Methods.* Neural data were recorded from deep brain nuclei in three male pediatric subjects with dystonia, undergoing a previously described procedure to clinically assess possible targets for deep brain stimulation, in two conditions: "on-BZD" versus "off-BZD" (baseline).

Recordings were gathered through pairs of externalized sEEG electrodes in basal ganglia, thalamus, and the pedunculopontine nucleus (PPN), both during rest and during DBS. Local field potentials (LFPs) during rest were characterized through power spectral density (PSD) analyses. EPs were compared in amplitude between the "on-BZD" and "off-BZD" conditions through paired tests. *Results.* PSDs showed consistent reductions in activity during benzodiazepine treatment, over all studied brain regions and for all three subjects. The benzodiazepine effects on DBS EPs were more complex, but common themes were seen between the two stimulation frequencies, including larger STN EPs during GPi DBS, and smaller VIM EPs and STN EPs during VIM DBS. *Discussion & conclusion:* Our preliminary results from 3 subjects indicate that changes in origin or target excitability due to benzodiazepines lead to changes in the effectiveness of communication between the two regions. This could, in turn, be responsible for changes in the overall pattern of activity, possibly interfering with or attenuating the transmission of the signals responsible for dystonia.

5.2 Introduction

Benzodiazepines (sometimes shortened BZD) are a class of medications frequently used in the treatment of hyperkinetic movement disorders, including the hyperkinetic components of dystonia. The mechanism of benzodiazepine action is not known, but the medication seems to act at pharmacologically specific binding sites by linking to GABA receptors, which have a heterogeneous distribution in the human central nervous system. In this chapter, we show changes in DBS EPs linked to when patients are on benzodiazepine treatment, versus not. The use of temporary sEEG electrodes for evaluation of DBS targets gives us the opportunity to examine the transfer of activity between different deep brain regions. We report changes in DBS EPs in

three subjects who received DBS both while they were *on* prescribed benzodiazepine treatment, and when they had been *off* the medication for at least 24 hours.

The management of dystonia is complex, and clinicians are currently challenged by a paucity or, at best, inconsistency of evidence to inform management strategies. In control conditions, one could hypothesize that the benzodiazepines would link to GABA receptors contained in GPi and therefore increase the inhibitory GPi output to thalamus. Consequently, the thalamic output to the cortex would be reduced, and thus, the motor neurons would reduce the activity at the muscle level. However, while many studies have investigated the effects of benzodiazepines on cortical activity, such as increased beta band power [63]–[65], no data is currently available on its effects on deep brain regions, nor on how these regions' responses to DBS are affected. As such, the effects of benzodiazepines on dystonic patients are still unknown, but are likely to affect the entire motor pathway, especially the abnormal GPi output activity in these patients.

We seek to describe the effects of benzodiazepines on multiple deep brain structures involved in motor control, and do so by recording from basal ganglia (STN and GPi), thalamic nuclei (Voa/Vop, VIM and VA), and the pedunculopontine nucleus (PPN) in three awake dystonic subjects at rest, comparing between conditions of on-benzodiazepines (on-BZD) and off-benzodiazepines (off-BZD, baseline).

5.3 Materials & methods

5.3.1 Patient selection

Retrospective analysis of data from three pediatric subjects, undergoing staged procedure to determine optimal area for implantation of DBS leads for the treatment of dystonia, were utilized in this case study (Table 5.1).

Table 5.1. Demographic characteristics of the 3 subjects included in the benzodiazepine study.

Subject	*Etiology*	*Charac-teristics*	*Gender*	*Age (yrs)*	*Implanted regions (bilateral)*	*"On-BZD" DBS times*	*Benzodiazepine doses*
1	Glutaric Aciduria Type I	Hypertonic dystonia	M	13	GPi*, STN, VA*, VIM, Voa/Vop	Day A: 12-1pm	Day A: 8:43am & 12:08 (2 mg diazepam, IV)
						Day B: 4pm	Day B: 2:34pm (1.5 mg diazepam, IV)
						Day C: 10:30am	Day C: 9:08am (1.5 mg diazepam, IV)
2	KMT2B (genetic)	Chorea, dystonia	M	10	GPi, STN, VA, VIM, Voa/Vop, PPN	3-4:30pm	7:20am (5 mg diazepam, IV)
							6:44am (3 mg diazepam, enteral)
3	Cerebral palsy	Tremor, dystonia	M	14	GPi, STN, VA, VIM, Voa/Vop, PPN	6pm	3:20pm, 4:32pm & 9:11pm (0.5 mg clonazepam, enteral)

** For subject 1, one lead in GPi and another in VA (both in the right hemisphere) were dislocated between the benzodiazepine and baseline conditions. Hence, they were excluded from the analysis.*
Abbreviations: BZD, benzodiazepines; M, male; IV, intravenous; GPi, globus pallidus internus; STN, subthalamic nucleus; VA, ventral anterior; VIM, ventral intermediate; Voa/Vop, ventral oralis anterior/posterior; PPN, pedunculopontine nucleus.

5.3.2 Surgical procedure

For each subject, up to 6 temporary sEEG leads were implanted in each hemisphere into target regions including VA, Voa/Vop, VIM, STN, GPi, and PPN (Table 5.1).

5.3.3 Electrophysiological recording

All passive data were recorded from micro-contacts during two intervals of five minutes in the NMU. One of the intervals was the baseline condition, corresponding to a resting period without benzodiazepine treatment (off-BZD) after having been off benzodiazepines for at least 24 hours prior. The other interval was the on-BZD condition, corresponding to a resting period after the patient had been treated with benzodiazepines.

Data were also recorded during DBS in both conditions (see details below). Table 5.1 describes the patient etiologies, symptoms, genders, ages, implanted regions, and administered benzodiazepine doses in relation to the on-BZD DBS times.

5.3.4 Stimulation protocol

DBS was administered through pairs of macro-contacts at 25 and 55 Hz, and the stimulation protocol was typically repeated through multiple contact pairs on each DBS lead.

5.3.5 Data analysis

5.3.5.1Power spectral density

The unavoidable realities of mechanical, physical, and thermal noise decrease the SNR of raw data recordings, making it difficult to detect neural activity. Therefore, prior to power spectral density (PSD) analysis of the passive recordings, we used orthogonal multilevel wavelet decomposition (MWD) [66] for signal filtering. Before analysis, data portions that held obvious electrical artifacts were rejected, based on visual inspection. Data recorded from micro-contacts within deep brain targets (visually confirmed through neuroimaging) were used for the analysis in the frequency

domain, using fast Fourier transform (FFT) based methods [67]. The power spectra were normalized with respect to their standard deviations (z-score).

Finally, PSD grand averages were taken of the 300 seconds of passive recordings across all micro-contacts within brain targets, in both conditions (on-BZD and off-BZD). The nonparametric Wilcoxon signed-rank test was used to compare the spectral features between the two conditions. A frequency band of 1-50 Hz was chosen to include the alpha and beta frequencies (8-35 Hz), which have been found to be associated with movement in Parkinson's disease and dystonia patients. The significance threshold was set to 0.05, with Bonferroni correction for multiple comparisons.

5.3.5.2Evoked potential and connectivity analysis

My automated EP detection method (ADPREP) was implemented to detect any evoked potentials in the recordings during DBS. When an EP was detected in both conditions, on-BZD and off-BZD, the sample pair of EP P2P amplitude values was included in the final statistical comparison of EP amplitudes between the two conditions. Non-normal difference distributions were tested for significant differences using the Wilcoxon signed-rank test, while normal difference distributions were analyzed using the paired t-test. The significance threshold was set to 0.05.

5.4 Results

Both the power spectra and the EPs from 25 and 55 Hz DBS showed differences between the two conditions (on-BZD vs off-BZD), throughout multiple deep brain regions in thalamus, basal ganglia, and the striatum (PPN).

5.4.1 Frequency band analysis from basal ganglia and thalamic nuclei recordings

In order to identify the effects of benzodiazepines on the brain's activity during rest, power spectral density (PSD) analyses were conducted to compare the differences between the two conditions for each hemisphere. The power spectra show the grand average across all microelectrode recordings for basal ganglia and thalamic nuclei recordings during 5 minutes for both conditions. A strong reduction of the power in the benzodiazepine condition (on-BZD) compared to baseline (off-BZD), *$p<0.05$, was seen in all targeted deep brain structures, for all three subjects in the alpha and beta bands. Figure 5.1, Figure 5.2, and Figure 5.3 show the PSDs of brain signals from the GPi, VA, Voa/Vop, VIM, STN and (for two of the subjects) PPN. Only frequencies from 1 to 50 Hz are displayed, as no significant differences were seen at higher frequencies.

Figure 5.1 shows the PSDs for subject 1 based on sEEG recordings from GPi, STN, VA, VIM and Voa/Vop, bilaterally. These data show a strong reduction of the amplitude during the on-BZD condition compared to baseline (off-BZD). The greatest power drop is seen around 8 Hz, whereas the power recovers over 20 Hz. This is true for both conditions, although the on-BZD condition contains less power (lower amplitude) than the off-BZD condition – for both hemispheres and for all deep brain structures. The bar graphs show the clear differences in power between off-BZD (black bars) and on-BZD (red bars); *$p<0.05$ (Bonferroni-corrected). For this subject, in both hemispheres, the max reduction from off-BZD to on-BZD was seen in STN.

Similar results were seen in subject 2 (Figure 5.2). There is a strong reduction of the power (*$p<0.05$, Bonferroni-corrected) within on-BZD compared to baseline (off-BZD). However, in contrast to subject 1, all deep brain structures in subject 2 were decreased at the same level; power values around 0.8 are reached in the off-BZD (baseline) condition, and around 0.2 in the on-

BZD condition. Another contrast to subject 1 is the frequency with the largest power drop, which is around 25 Hz; moreover, no ripples or waves are seen in the PSD in the surrounding frequencies.

Finally, subject 3 showed an overall reduction in the on-BZD condition as well (Figure 5.3). The largest power drop was noted at approximately 25 Hz, without recovering waves – similar to subject 2, but in contrast to subject 1. For subject 3, there were significant reductions in power in GPi, VA and Voa/Vop during the on-BZD condition (*$p<0.05$, Bonferroni-corrected). For STN and VIM, there were instead slight *increases* of power, but these were non-significant ($p>0.05$).

5.4.2 Effects of benzodiazepines on deep brain stimulation evoked potentials

While we saw some variability in the DBS EP amplitude results between stimulation frequencies, subjects, and hemispheres, there were also common trends between the whole-brain group analyses at 25 & 55 Hz (Figure 5.4, left & right, respectively). These common themes included larger STN EPs during GPi DBS, and smaller VIM EPs and STN EPs during VIM DBS. In addition, 25 Hz (but not 55 Hz) DBS elicited larger EPs in Voa/Vop during Voa/Vop stimulation and PPN stimulation, and smaller EPs in STN during VA stimulation, while the subjects were on benzodiazepines.

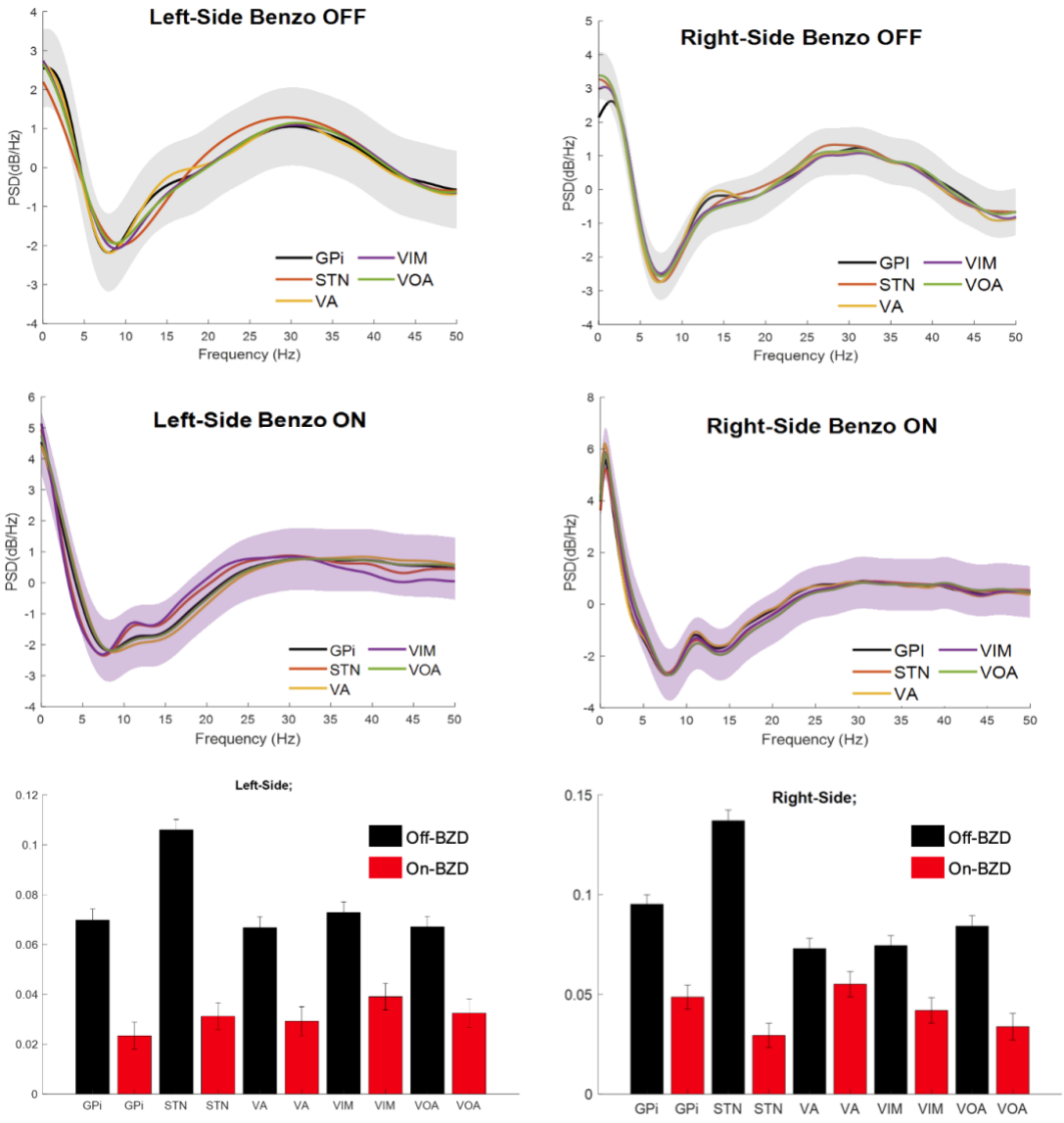

Figure 5.1. Power spectral density (PSD) analyses for basal ganglia and thalamic nuclei while the subject was on benzodiazepines (on-BZD) versus the baseline condition (off-BZD): Subject 1. Both hemispheres are shown (left column: left hemisphere; right column: right hemisphere). Top two rows: The PSDs show the average and standard deviation for all microelectrodes, placed bilaterally in GPi (black traces and shading), STN (orange), VA (yellow), VIM (purple), and Voa/Vop (green). Off-BZD results are displayed on the top row; on-BZD on the middle row. Vertical axis: power (dB/Hz). Horizontal axis: frequency (Hz). Bottom row: Bar graphs depict the averages and standard deviations of the PSD amplitudes between the two conditions, on-BZD (red bars) versus off-BZD (black bars), for each brain region, from 1 to 50 Hz. There is a significant difference between the two conditions (*p<0.05) in all targeted deep brain regions. Vertical axis: normalized power difference (dB/Hz). Horizontal axis: targeted deep brain structure.

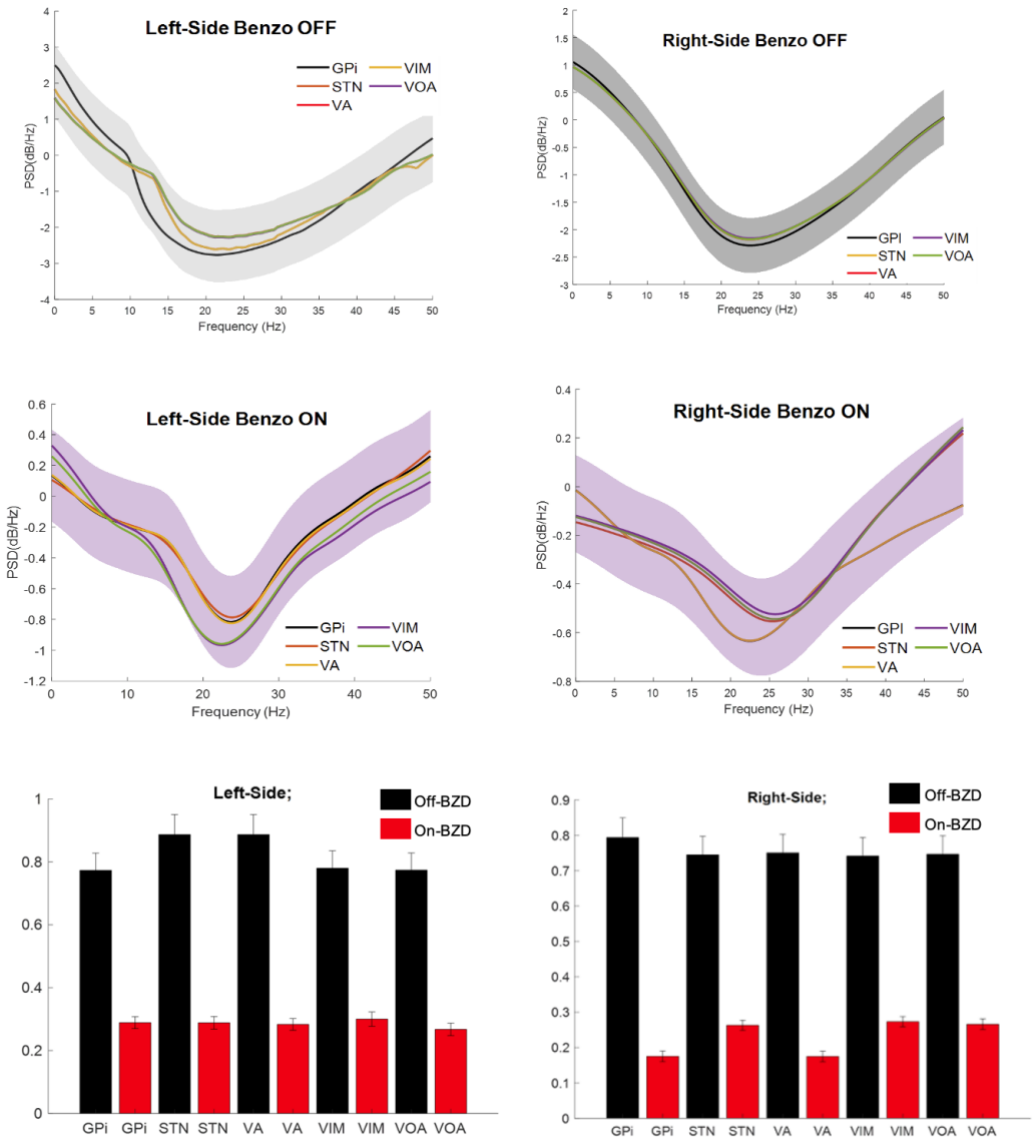

Figure 5.2. Power spectral density (PSD) analyses for basal ganglia and thalamic nuclei while the subject was on benzodiazepines (on-BZD) versus the baseline condition (off-BZD): Subject 2. There is a significant difference between the two conditions (*p<0.05) in all targeted deep brain regions. *(Same description as Figure* 5.1*.)*

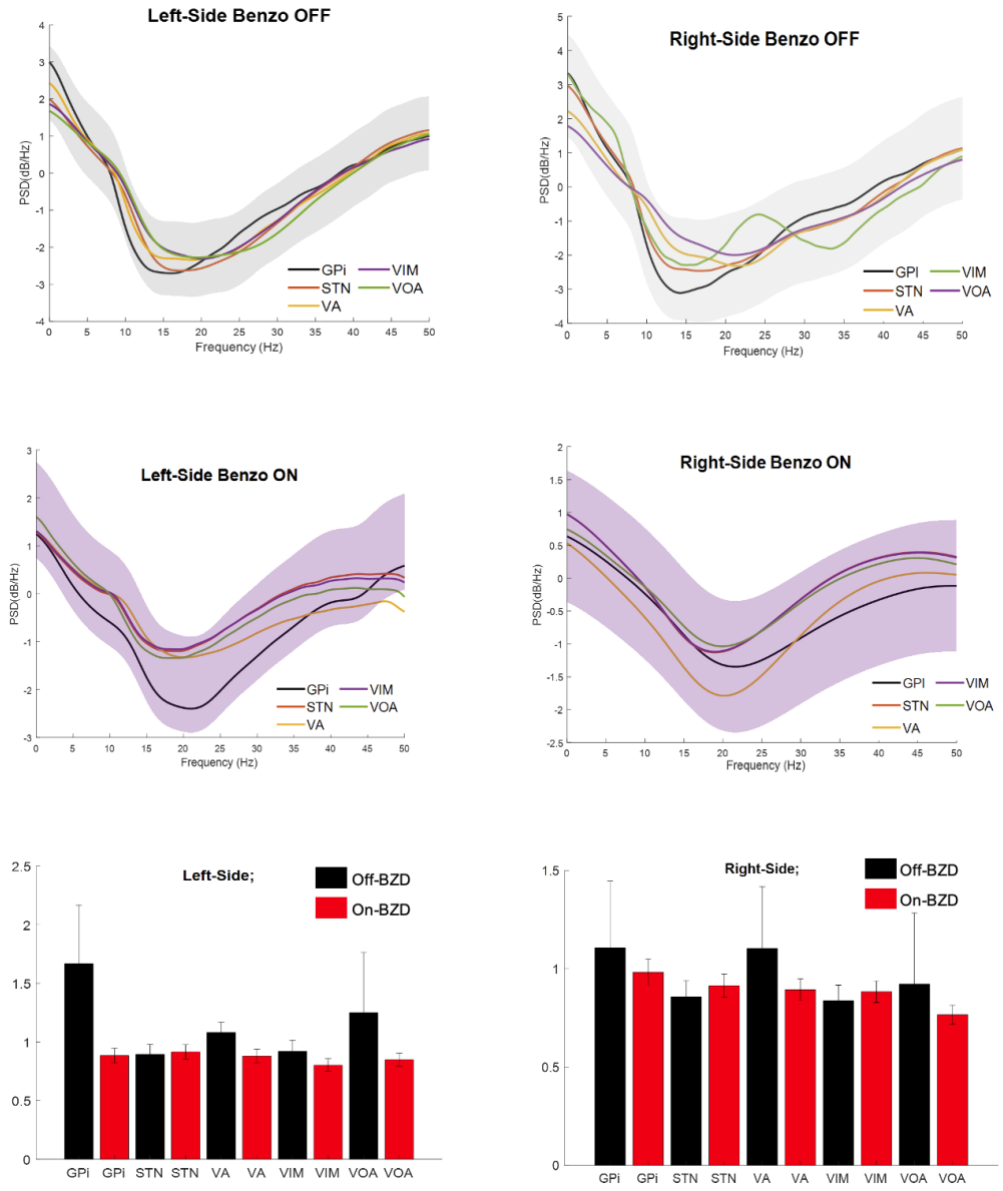

Figure 5.3. Power spectral density (PSD) analyses for basal ganglia and thalamic nuclei while the subject was on benzodiazepines (on-BZD) versus the baseline condition (off-BZD): Subject 3. There is a significant difference between the two conditions (*p<0.05) in all targeted deep brain regions, except right VIM and left & right STN. *(Same description as Figure* 5.1*.)*

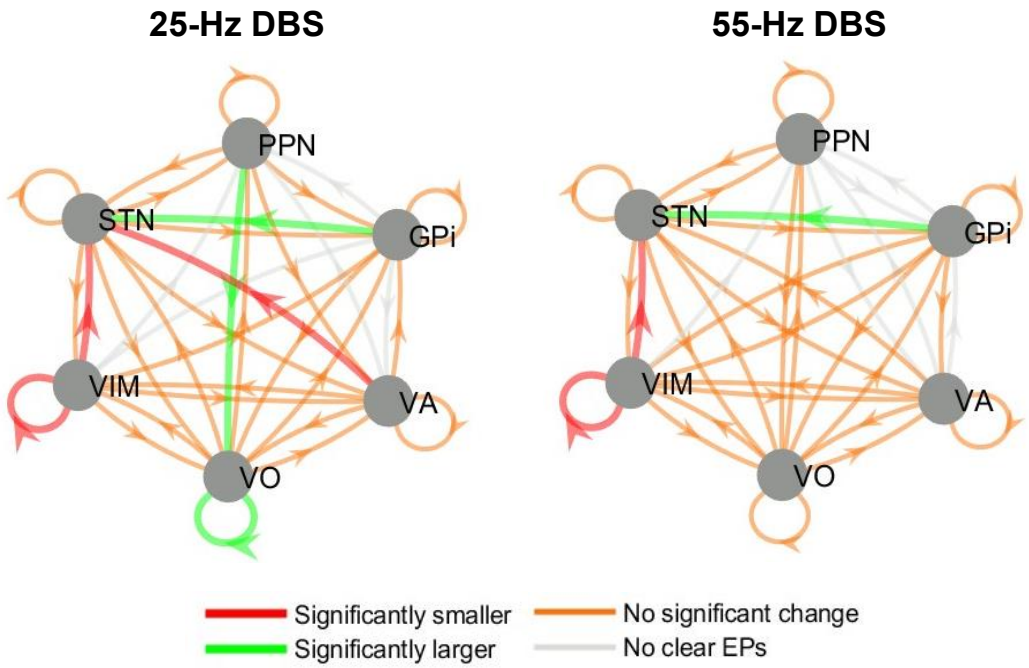

Figure 5.4. Directed graphs showing the group effects of benzodiazepines on EP amplitude during 25 & 55-Hz stimulation. Results are from the group analysis of all three subjects; left: 25-Hz DBS, right: 55-Hz DBS. The arrows point from each nucleus where DBS was administered, to each nucleus where recordings were available (and an EP may have been elicited). Red/green arrows denote connections where the amplitudes of the EPs significantly decreased/increased when benzodiazepines were administered; orange/gray arrows symbolize connections where EP amplitudes were not significantly affected/no clear EPs were seen.

5.5 Discussion

In contrast to protocols published to date, our procedure allows for simultaneous recording from multiple targets in awake patients without the influence of anesthesia [20]. Therefore, it allows us to describe the effects from benzodiazepines on targeted deep brain regions at rest, as well as during electrical stimulation of deep brain nuclei.

The basal ganglia compose a complex system that sends and receives feedback to the cortex through thalamus and striatum. STN and the striatum receive cortical inputs, while GPi

sends information to the thalamus, which modulates cortical activity. The "rate model" of basal ganglia function suggests that high activity in GPi is required in order to inhibit movement at rest [68]. How alterations of this circuit result in dystonic muscle contractions is still not understood, nor how the treatments are affecting the deep motor pathways in dystonia.

Previous publications have studied frequency patterns in pallidum, in dystonic patients with clinically successful outcomes, and presented findings that have tried to elucidate the pathophysiology underlying dystonia [10]. Such mechanisms include pathological firing rates in the GPi [69] as well as theta and beta band activity in GPi [70] and the STN [71]. Although the action mechanism of pallidum in the pathophysiology of dystonia is under debate, the presence of peaks in alpha and beta bands in basal ganglia is likely to be a sign of the pathophysiology underlying dystonia. In alignment with prior studies, our results display peaks in these frequency bands in all subjects.

Overall, the PSD analysis unveiled a strong reduction in amplitude in the on-BZD condition for all subjects. Based on the benzodiazepine binding site (e.g., presynaptic GABA receptors), we could expect a decrease of GPi output, and consequently, an increase of motor thalamic nuclei output (Voa/Vop and VA) to the cortex. However, if the benzodiazepine binding site is on receptor nuclei (e.g., postsynaptic GABA receptors linked to thalamic nuclei), we could expect a decrease of thalamic nuclei output due to hyperpolarization, while the GPi output remains unaltered. Here, our results show a *decrease* of GPi and thalamic activity under the influence of benzodiazepines, leading us to believe that the effects of benzodiazepines are mixed over both pre- & postsynaptic GABA receptors. This would strongly reduce activity in both basal ganglia and thalamic nuclei, since these receptors have a heterogeneous distribution along the motor pathway.

However, one of our most interesting findings is that the reduction of amplitude is even greater in STN than in GPi. This contrasts with our expectations, based on the multitude of GABA receptors in the pallidum. Here, we could postulate that on one hand, there is reduced thalamic excitation to the cortex and downstream reduced excitation of STN via the hyperdirect pathway, and therefore, we see a decrease in STN activity. On the other hand, recordings from nonhuman primates [72] and Parkinson's disease [73] are consistent with the hypothesis of high GPi activity at rest; this large GPi output to thalamus (through the orthodromic pathway) is reduced by the benzodiazepines, as our results show. However, an alteration in the function and connectivity of GPi could depolarize alternative pathways, such as antidromic connections (e.g., GPi to STN), sending a larger inhibitory signal to STN, as shown in Figure 5.4 (green arrow). Therefore, this could provide a plausible explanation about a larger reduction of STN activity than GPi activity in the on-BZD condition. These hypotheses all suggest a mechanism for effectiveness of GPi DBS to treat dystonia.

Based on the PSD analysis, we initially expected to find a general decrease in DBS EP amplitude in the on-BZD condition. However, what we saw was more complex than that, with EPs that increased, decreased, or showed no significant change in size, depending on the connection (Figure 5.4). However, after further consideration of the complexity of the brain's connectivity, and the multitude of combined excitatory and inhibitory connections, a varied response should perhaps have been expected. The mechanism of benzodiazepines is not entirely straightforward either: while benzodiazepines have a generally inhibitory effect, certain kinds of benzodiazepines target GABAa receptors, which are post-synaptic, whereas others target GABAb receptors, which are presynaptic. This is of importance when studying anti- vs. orthodromic connections, since DBS

seems to be able to elicit antidromic EPs, possibly by depolarizing the presynaptic axons coming in from other areas into the region that is being stimulated.

Regardless, studying the effects of benzodiazepines on DBS EPs can provide important information, since the EP amplitude can be considered a measure of the neurological (but not necessarily clinical) effect of DBS on a region (increased or decreased excitation or inhibition). I.e., increased amplitudes would signify an increased response to DBS, and vice versa. Benzodiazepines are not expected to alter brain structure and physical connectivity during the timescale associated with the results reported here; therefore, changes in DBS EPs are likely to be due to changes in excitability at either the DBS stimulation site, or at the EP site. Interestingly, despite the widespread expected effects of BZD on deep brain circuitry, in many cases there is no change in DBS EPs size, indicating either that these areas are unaffected by BZD, or that changes in the connectivity as measured by DBS EPs are not the mechanism responsible for changes in information processing due to benzodiazepines.

Contrary to the increased amplitude of EPs in STN during GPi DBS, we saw a reduction in EP amplitudes stemming from VIM DBS, in both VIM and STN. These changes could both be related to inhibition of thalamus: e.g., if the benzodiazepines hyperpolarize VIM neurons and increase inhibition of the nucleus, this could make depolarization in VIM from DBS more difficult, leading to a smaller response in VIM during VIM DBS. Consequentially – despite the fact that there is no known direct neurological pathway between VIM and STN – any EPs elicited in STN during VIM DBS would be expected to follow a trend similar to that of the VIM "self-EPs", as less excitability in the source nucleus would translate to less information being transmitted to other regions.

Regarding the source of the increased GPi-STN EP amplitudes: the reduced STN EP amplitudes during VIM DBS, contrasting the increased STN EP amplitudes during GPi stimulation, allude to STN not being the common source of change. Namely, it seems more likely that STN EPs are impacted differently from different stimulation locations due to the change in excitability in those source nuclei, rather than experiencing a general change in excitation in STN itself. Similar logics could also postulate explanations for the significant benzodiazepine effects that were seen solely during the 25-Hz DBS (Figure 5.4, left).

The common trends found from the group analyses of the two different DBS frequencies are a promising sign of the reliability of our results. Nevertheless, a larger pool of subjects would be necessary to generate more significant and trustworthy results. Moreover, additional EP measurements such as delay and/or frequency components may also help generate a clearer understanding of the impact of benzodiazepines on DBS EPs. Similar studies in other subject demographics would also be insightful to understand which, if any, of these trends are unique to dystonic subjects, and which others may be a good representation of healthy brain activity.

Limitations in this study include the different underlying diseases and areas of brain injury among our subjects, as well as the inconsistency of medication types, dosages, and timings (Table 5.1). Our data are also limited by recordings from electrodes that are placed solely in potential DBS targets – full understanding may require additional recordings from striatum, cortex, and other brainstem targets. However, while these would help the data interpretation, they may not be feasible in humans.

5.6 Conclusion

Benzodiazepines have widespread effects throughout the brain, potentially acting at GABA receptors co-localized on many cells with inhibitory (hyperpolarizing) inputs. The effects of benzodiazepines on ameliorating hyperkinetic movement disorders are likely multifactorial. Our results suggest that in some cases, changes in effective connectivity between deep brain regions could contribute to the mechanism of benzodiazepine action. In particular, we conjecture that changes in origin or target excitability will lead to changes in the effectiveness of communication between the two regions that could be responsible for changes in the overall pattern of activity, possibly interfering with or attenuating the transmission of the signals responsible for dystonia. Further research will be needed to confirm this finding in additional subjects, and to determine the relative importance of this effect compared to other mechanisms of benzodiazepine action.

CHAPTER 6: MODELING OSCILLATORY DEEP BRAIN STIMULATION EVOKED POTENTIALS WITH PHASE OSCILLATOR NETWORKS

This chapter is a reprint of my co-first-author publication with the same name, accepted for publication in the 11th International IEEE EMBS Conference on Neural Engineering (NER 2023) proceedings [74]. It presents a phase oscillator network model to describe oscillatory DBS EPs detected in the basal ganglia (and thalamus) during GPi DBS. Project contributions were split evenly with my co-first author Dr. Jonathan Realmuto: I focused on data collection and curation, while Dr. Realmuto developed the computational model. My particular contributions included investigation, data curation, software, formal analysis, and writing (part of the original draft, as well as review and editing) [37]. Some text from the original publication has been rearranged or omitted to preserve the flow of this dissertation.

6.1 Abstract

Deep brain stimulation is a highly effective therapy for an increasing number of neurological and psychiatric disorders. However, the optimal electrode placement and stimulation parameters are not the same for each individual; thus, careful planning and tuning is required. This process can be time-consuming and is usually heuristically guided by clinician experience. Personalized models tuned for each individual, which capture important features of the underlying network dynamics, would provide a quantitative method for target localization and stimulation tuning. Towards this, we present a preliminary investigation on modeling deep brain evoked responses with a network phase oscillator model. The model provides a forward dynamic simulation with the stimulation signal as input and average response of each subpopulation as output. The parameters of the

model include the coupling strength within and between subpopulations, and the topology of the network. We train the model using averaged data from a pediatric primary dystonia patient during a burst stimulation protocol in the pallidum. Our model provides a good fit to the data with an R-squared of 0.80. Using a contrasting data set with different stimulation parameters, we show that our model also provides a similar response to data it has not been trained on, suggesting it captures important features of the network dynamics.

6.2 Introduction

Deep brain stimulation (DBS) has emerged as an important treatment paradigm for a variety of neurological and psychiatric disorders, including Parkinson's disease, essential tremor, dystonia, obsessive-compulsive disorder, depression, and epilepsy [75]. A typical intervention requires analysis of the patient's physiology and etiology, planning of the DBS targets, and, after implantation, careful tuning of the stimulation parameters. Predicting the responses to different stimulation targets and parameters would aid clinicians in target selection and parameter optimization, and is therefore of critical clinical significance.

Evoked oscillatory neural responses (EONR) have recently been observed in Parkinson's disease (PD) in STN and globus pallidus (GP) during STN stimulation [44], [48], [57], [76]. The mechanism responsible for this behavior remains unclear, with some proposed theories involving patterns of inhibition and excitation [77] and interactions between STN and connected structures, such as the pallidum [78], [79]. The EONR is a promising biomarker that could guide in electrode implantation surgery, locate the most effective stimulation contacts post-implantation, and provide a feedback signal for closed-loop DBS [44], [57].

We have observed a similar phenomenon in a primary dystonic patient, localized around STN and Voa/Vop, with a smaller response observed in VIM during GPi stimulation. These responses share many of features as previously reported EONRs in PD patients, including the stereotyped "resonant" response (where the amplitude increases and sharpens across consecutive pulses), the amplitude range, and the latency until the peak of the response.

Our aim was to explore a network phase oscillator model for use in forward dynamic simulations of DBS. Phase oscillator models, typically abstracted in the form of the famed Kuramoto oscillator [80], provide the mathematical framework for collective synchronization and phase transitions [81], and have been used to describe feedback loops between excitation and inhibition in large neuronal networks [82], explain neuronal inhibition [83] and phase-locking mechanisms in DBS [84], and replicate empirical relationships of cortical oscillations [85]. We introduce a new multi-population phase oscillator network, trained on empirical EONRs, to realize a forward dynamic simulation of the underlying network and subsequently probe the model with a different set of stimulation parameters.

6.3 Computational methods

6.3.1 Model overview

Our model is a variation of the Kuramoto phase oscillator [80], including positive and negative coupling [86] and interactions between subpopulations [87]. The coupling strength parameter models excitatory (positive values) and inhibitory (negative values) interactions. Excitatory interactions tend to synchronize, while inhibitory interactions tend to desynchronize. We partition the network into distinct subpopulations, each one modeling a specific target in the deep

brain, and each consisting of an equal number of phase oscillators. Each subpopulation influences the other subpopulations through network interactions (projections), i.e., directed connections between the oscillators of one subpopulation to the oscillators of another subpopulation. We restrict the coupling strength to be the same for the connections within each subpopulation and for all subpopulation-to-subpopulation connections. Lastly, in order to model the DBS stimulation, we allow for coupling with the stimulation pulses through a final coupling parameter. A summary of the multi-scale model is provided in Figure 6.1. The phase dynamics of the n^{th} node within subpopulations σ is:

$$\dot{\phi_n^\sigma} = \omega^\sigma - k^\sigma \sum_{m=1}^{N} A_{nm}^\sigma \sin(\phi_n^\sigma - \phi_m^\sigma) - \sum_{\gamma \in \mathcal{N}_\sigma} k^{\sigma\gamma} \sum_{m=1}^{N} A_{nm}^{\sigma\gamma} \sin\left(\phi_n^\sigma - \phi_m^\gamma + \varphi^{\sigma\gamma}\right) - k_u^\sigma \sin(\phi_n^\sigma + \varphi^\sigma)\, u \tag{6.1}$$

where φ^σ is the phase of the n^{th} oscillator within the subpopulation σ, ω^σ is subpopulation σ's natural frequency, k^σ is the local coupling strength within the subpopulation, N is the number of oscillators in the subpopulation, A^σ is the local network adjacency matrix, N_σ is the set of subpopulations that have projections onto subpopulation σ, $k^{\sigma\gamma}$ is the projection coupling strength of subpopulation γ onto subpopulation σ, $A^{\sigma\gamma}$ is the network adjacency matrix of subpopulation γ onto subpopulation σ, $\phi^{\sigma\gamma}$ is the constant phase shift between the oscillator in subpopulation σ and the oscillators in subpopulation γ, k^σ is the coupling strength between the subpopulation σ and the DBS stimulation, ϕ^σ is the constant phase shift between the DBS stimulation and the oscillators in subpopulation σ, and u is the stimulation signal, which in practice is a binary signal

encoding the stimulation pulses. The connectivity within and between each subpopulation is encoded using directed adjacency matrices whose elements are $A_{nm} = 1$ for a connection (interaction) from oscillators m to n, and 0 otherwise. The output of each oscillator is sinusoidal, and the response of each subpopulation is the average response over all subpopulation oscillators:

$$y^{\sigma} = \frac{1}{N}\sum_{n=1}^{N} Re\{K\, e^{i\phi_n^{\sigma}}\} \tag{6.2}$$

with $i = \sqrt{-1}$, K the amplitude, and Re{ · } the real part.

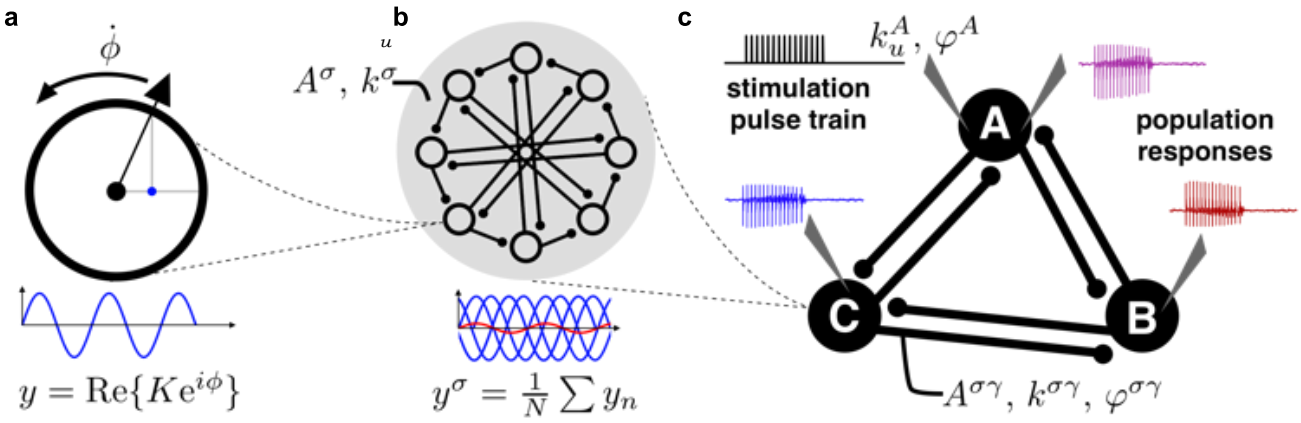

Figure 6.1. Details of the proposed phase oscillator network model. (a) Each oscillator emits a sinusoidal response y with phase ϕ and amplitude K. The phase dynamics $\dot{\phi}$ evolve according to Equation 6.1. (b) Each subpopulation σ consists of N oscillators interacting according to the adjacency matrix A^{σ} with coupling strength k^{σ}. The total response y^{σ} of subpopulation σ is the average oscillator response over all oscillators within the subpopulation. (c) We consider three subpopulations (A, B, and C) influencing each other with subpopulation-to-subpopulation adjacency matrices $A^{\sigma\gamma}$, coupling strength $k^{\sigma\gamma}$, and phase shift $\phi^{\sigma\gamma}$ (for subpopulation γ onto subpopulation σ). The oscillators in subpopulation A are coupled to the stimulation with coupling strength k^{A} and phase φ^{A}.

6.3.2 Network topology

The network topology was designed through preliminary investigations. We sought a responsive and highly coupled network without all-to-all connections, which are computationally expensive. Starting with a directed ring network, where the oscillators of each subpopulation are arranged in a ring and each project to one neighbor (e.g., counterclockwise neighbor), we found that this often resulted in chimera states [88], where clusters of oscillators will synchronize together, even if the local coupling parameter is negative (desynchronizing), but out of phase with other clusters. To avoid this behavior, we added a second projection from each oscillator to its farthest neighbor. The final network design can be seen in 6.1b and is described by:

$$\overline{\mathrm{A}}_{\mathrm{nm}} = \begin{cases} 1, & \text{if } m = (n+1) \bmod N \quad \text{or} \quad m = \frac{n+N}{2} \bmod N \\ 0, & \text{otherwise} \end{cases} \tag{6.3}$$

In this work, the network connections all take this form: $A^{\sigma} = A^{\sigma\gamma} = \overline{A}$, $\forall \gamma \in N_{\sigma}$, for each subpopulation σ.

6.3.3 Model setup and optimization

The number of subpopulations were chosen to replicate the empirical recordings, which are described in detail in the next section, and thus includes three subpopulations (σ ∈ {A, B, C}), corresponding to the target structures GPi, VIM, and VO/STN (Figure 6.1a). Each subpopulation had N = 8 oscillators. Only subpopulation A (GPi) is allowed stimulation coupling with strength parameter k^{A}. The constant phase delays were assumed to be symmetric, so that $\phi^{\sigma\gamma} = \phi^{\gamma\sigma}$. Given these assumptions, there were 18 parameters to fit to the empirical data. The parameters were optimized by minimizing the following cost function:

$$J = \sum_{t\in\mathcal{T}} \left(y^{\mathrm{GPi}}(t) - y^{A}(t)\right)^2 + \left(y^{\mathrm{VIM}}(t) - y^{B}(t)\right)^2 + \left(y^{\mathrm{VO/STN}}(t) - y^{C}(t)\right)^2 \qquad (6.4)$$

which is the squared error taken only during the EONR activity, parameterized by the set T, e.g., an index mask that identifies the regions of interests. Since the problem is nonconvex, with many local minima, we alternated between a gradient based solver (*fmincon* in Matlab) and a derivative free search (*patternsearch* in Matlab). All simulations are numerically integrated using a first order Euler method with a time step matching the sampling frequency of the processed data.

6.4 Experimental methods

6.4.1 Patient selection

Data from 1 pediatric patient (female, 16 years old) with primary dystonia (DYT1) was used in this case study.

6.4.2 Electrode placement

Seven (7) temporary Ad-Tech MM16C depth electrodes (Ad-Tech Medical Instrument Corp., Oak Creek, WI, USA; Figure 6.2b, top), consisting of 6 low-impedance macro-contacts, and 10 high-impedance micro-contacts, were implanted temporarily into potential DBS targets in the thalamus (VIM, VA, and Voa/Vop, also denoted as "VO") and basal ganglia (GPi and STN). The patient in this study also had previously implanted permanent leads bilaterally in GPi, consisting of 4 macro-contacts (Medtronic 3387, Figure 6.2b, bottom).

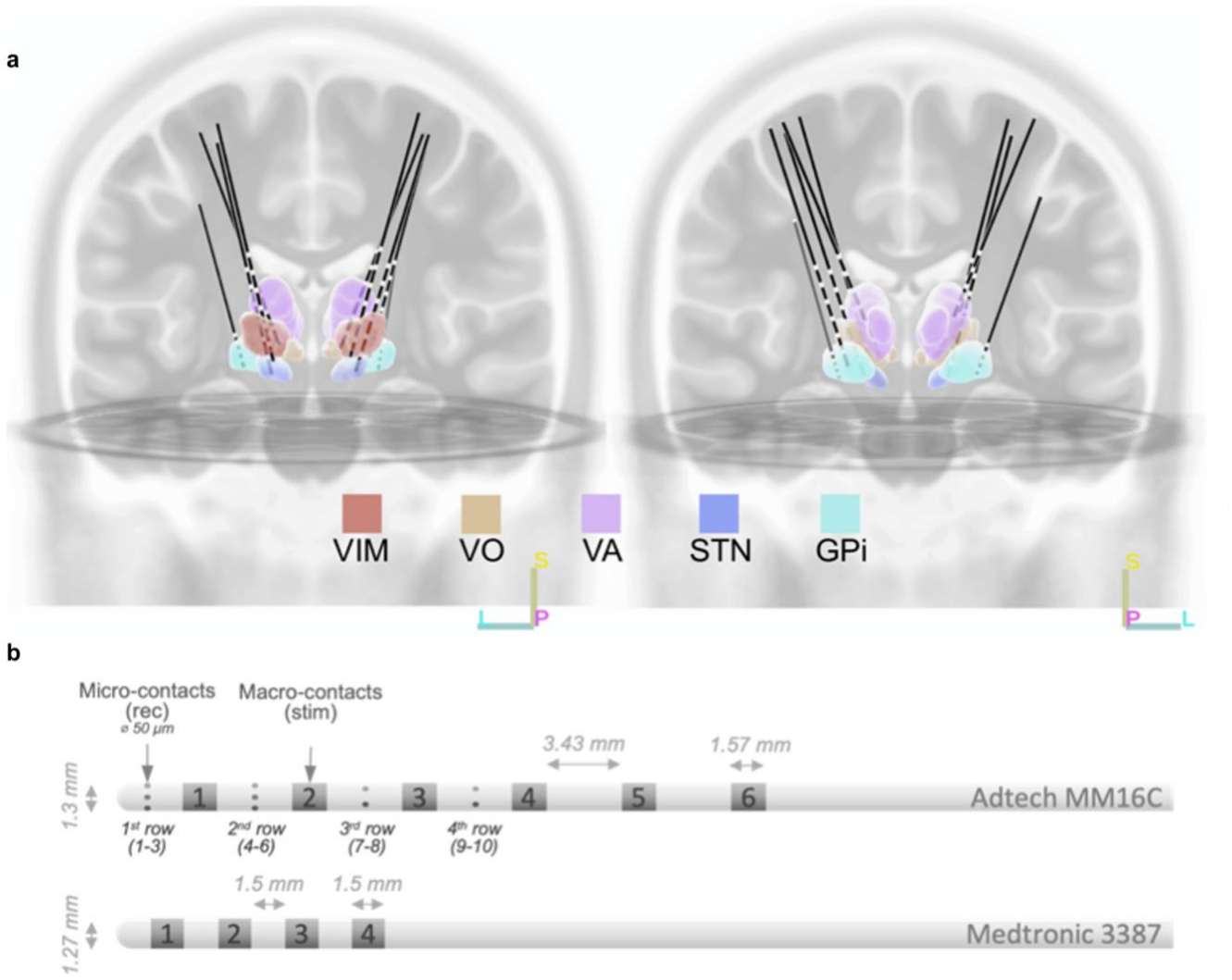

Figure 6.2. Visuals of the leads and the brain regions they were implanted in. (a) Front (left) and back (right) views of the DBS lead implant locations. White portions on the black leads represent the low-impedance macro-contacts (gray rectangles on leads in (b)). The image was generated by normalizing a postoperative computed tomography scan onto a preoperative magnetic resonance imaging scan, in combination with regions of interest from an adult template. Acronyms: globus pallidus interna (GPi), ventral intermediate (VIM), subthalamic nucleus (STN), ventral oralis anterior/posterior (VO). (b) Detailed schematic of the two types of electrodes implanted. Top: The Ad-Tech MM16C electrode, used as temporary leads (same as in Figure 12, General Methods). Bottom: The Medtronic 3387 electrode, previously implanted in the subject (permanent leads).

6.4.3 Stimulation parameters and data acquisition

Stimulations consisted of passive charge-balanced 3.5-V, 150-Hz pulses with 5-Hz burst frequency (100-ms stimulation periods separated by 100-ms intervals without stimulation). The stimulations were applied bilaterally, with 180-degree phase shift in timing, in the permanent GPi leads with 120-microsecond pulse width through contacts 1-2+ in the left hemisphere and 60-microsecond pulses through contacts 1-Case+ in the right hemisphere. Twenty seconds of concurrent bilateral stimulation were performed, generating approximately 100 stimulation bursts. The second stimulation protocol consisted of the same stimulation parameters, except with constant (non-bursting) 185-Hz stimulation; this data included 1000 cycles. All data were recorded concurrently during stimulation through all micro-contacts with a sampling frequency of 22 kHz, and subsequently bandpass filtered at 0.3-9 kHz.

6.4.4 Data post-processing

In this study, we analyzed the stimulation and responses from the right hemisphere. All ~100 segments were aligned and stimulus-triggered averaged, and the index mask (e.g., in Equation 6.4) was determined as the time span after an artifact until the index before the start of the subsequent pulse. Next, independent component analysis (ICA) was used for source separation. The ICA procedure was conducted independently for each electrode (eight bipolar channels per electrode were selected for ICA). After ICA, the signals were centered to have zero mean and were visually inspected, with the channel from the following electrodes chosen based on the amplitude and clarity of the response as the ground truth for the model training: GPi, VIM, and VO/STN (the VO/STN electrode spans both structures).

6.5 Results & discussion

After model optimization, the forward dynamic simulation provides a remarkably similar response when compared with the empirical data, as can been seen by comparing Figure 6.3 a & b with c & d. The model adequately captures the EONRs, including the "resonant" behavior, where the amplitude increases and sharpens with consecutive stimulation pulses, and captures the "ringing" effect after the last cycle. With an R-squared value of 0.8, our model explains a large portion of the variance within the original data. Using the same optimized model parameters, we simulated a second set of empirical data, where the stimulation was held constant (not bursting) at 185 Hz. The original data is shown in Figure 6.3 e & f, and the simulation is shown in Figure 6.3 g & h. Note that in neither the model nor the data is there an EONR apparent for the 185 Hz constant stimulation.

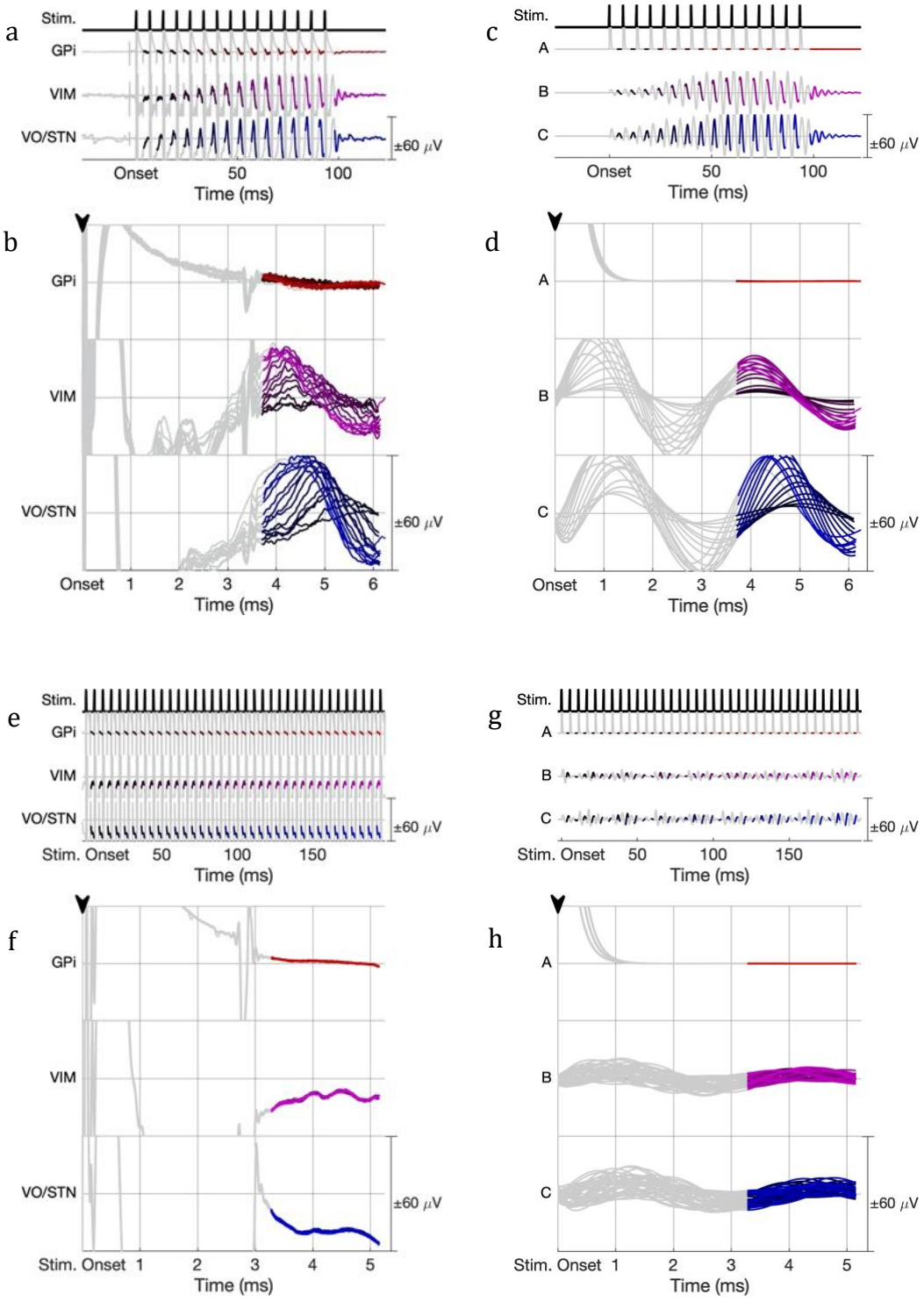

Figure 6.3. Comparison of the empirical data and simulations using the phase oscillator network model. (a) Empirical response during 150 Hz burst stimulation. Colored portions of the traces represent the time regions of interest, e.g., the EONRs. (b) Superimposed EONRs aligned to each pulse (time is encoded in trace shading, darker to lighter shades). (c)

Simulated response of the 150 Hz stimulation. (d) Simulated EONRs, superimposed and aligned to each pulse. (e) Empirical response during 185 Hz stimulation. (f) Superimposed responses aligned to pulse. (g) Simulated response of the 185 Hz stimulation. (h) Simulation responses, superimposed and aligned to each pulse. *Colored regions: time regions of interest. Red traces: GPi; pink traces: VIM; blue traces: VO/STN. Note: The stimulation artifact from the contralateral stimulations, which were phase shifted by 180 degrees relative to the ipsilateral stimulation, can be seen in the two empirical data sets, at the 3.33 millisecond mark in (b), and 2.70 millisecond mark in (f).*

6.6 Conclusions

We introduced a network phase oscillator model for dynamic simulations of DBS. Using empirical data, possibly related to a recently discovered biomarker, we showed that the parameters of the model could be optimized to produce a remarkably similar forward dynamic simulation, resulting in a good model fit to the empirical data (R-squared = 0.80). Using a second empirical data set, which was generated under different stimulation conditions, we showed that our model provides reasonable agreement with the data, arguing that the model captures important features of the individual neural network. Our results suggest that the phase oscillator model should be further investigated for potential applications in model-based DBS.

CHAPTER 7: DIFFUSION TENSOR IMAGING COEFFICIENTS CORRELATE WITH DEEP BRAIN STIMULATION EVOKED POTENTIAL AMPLITUDES AND DELAYS

This chapter presents preliminary results from our study of the relations between diffusion tensor imaging coefficients and evoked potential characteristics. The project was a collaboration among several lab members, and I will co-first-author the resulting paper. My main contributions are related to the DBS evoked potential data (peak-to-peak amplitude and time-to-first-peak delay) for all subjects, including all data processing leading up to it: investigation, data curation, software, formal analysis, validation, and visualization [37]. I also assisted in writing the paper, in particular playing a significant role in the editing of the paper.

7.1 Abstract

Background. Diffusion tensor imaging (DTI) is a quantitative analysis method for evaluating white matter integrity. Although both DBS EPs and DTI are valuable methods for studying neural connectivity between brain regions, the relationship between the characteristics gathered by the two approaches has not yet been studied. *Objective.* The objective of this study was to investigate the relations between DTI coefficients and DBS EP characteristics. *Methods.* Stimulations of 9 or 25 Hz were delivered through pairs of macro-contacts while simultaneously recording from micro-contacts. DTI was also conducted for each patient in order to study the correlation between DBS EP characteristics (amplitude and delay) and DTI coefficients: length, volume, and fractional anisotropy (FA) of the fiber tracts. Finally, we completed a linear regression to generate a generalized linear model (GLM), with the anatomical feature variables (calculated through the DTI analysis) as the inputs, and the EP characteristics as the outputs. *Results.* Our results show that

FA, tract length, and tract volume are significantly correlated with DBS EP characteristics. These results suggest that DBS signals travel across tracts to affect both local and distant brain regions, and the magnitude of the effect of DBS is, at least in part, determined by the integrity of the white matter tracts connecting the stimulation site to potential target regions. *Conclusion.* We have generated a model that validates DTI against ground truth electrophysiology. Our results provide crucial and novel confirmation that EPs are affected by the brain's white matter integrity and that this relationship can, at least crudely, be quantitatively demonstrated by a GLM. Such a mathematical model has the potential to predict DBS EP characteristics (e.g., amplitude and delay) using only DTI coefficients, which would open new possibilities for cases when intracranial deep brain recordings are not possible or available. Down the line, such a model may even be able to infer neurophysiological connectivity and possibly predict optimal DBS lead implant targets.

7.2 Introduction

A prerequisite for a beneficial outcome of DBS treatment is the accurate identification of the chosen brain target. Magnetic resonance imaging (MRI) can be used for stereotactic targeting in deep brain stimulation surgery; however, the accuracy of the electrode implantation in the target nuclei is not entirely reliable when only the anatomical image is used. To address this issue, standard brain atlases can be incorporated to predict the location relative to defined landmark coordinates, such as the anterior and posterior commissures. However, the accuracy of adult-based atlases in children with acquired brain injury is not assured, especially when considering the distortion and asymmetry of the injured brain.

With the development of multiple-contact leads for high-density recordings, and the growing capacity for streaming continuous data from multiple contacts simultaneously, the

popularity of local field potentials (LFPs), including EPs, has increased. These neural responses are transferred between brain regions through white matter tracts, which is why the loss of white matter integrity is often a major cause of neurological impairment [89], [90]. Diffusion tensor imaging (DTI) has been undisputedly praised as the best quantitative analysis method for evaluating such white matter integrity [91].

This project focuses on exploring the signal pathway of DBS treatment of patients with dystonia, a form of dyskinetic cerebral palsy (CP) that is associated with white matter injury [1]. If this relationship of signal transfer and white matter integrity can be described mathematically, this would be a leap forward in quantifying the relationship between cerebral neurophysiological signals and the underlying anatomical features of the brain.

7.3 Materials & methods

7.3.1 Subject selection

Twelve pediatric patients undergoing deep brain stimulation (DBS) implantation for the treatment of dystonia were recruited to participate in the present study (see Table 7.1 for patient demographics).

Table 7.1. Demographic characteristics of the 12 subjects included in the DTI-EP correlation study.

Subject	Etiology	Gender	Age [years]	Implanted regions
1	Cerebral Palsy	F	15	VA/VoaVop/VIM/GPi1
2	Cerebral Palsy	F	12	VA/VoaVop/VIM/GPi1
3	Cerebral Palsy	M	20	VoSTN/VIM/VPL/GPi
4	Cerebral Palsy	M	18	VA/VoaVop/VIM/GPi1
5	Cerebral Palsy	F	14	VA/VoaVop/VIM/GPi1
6	Cerebral Palsy	F	16	VA/VoaVop/VIM/GPi2/GPi1
7	Cerebral Palsy	F	12	GPi1/GPi2/VoaVop/VA/VIM
8	H-ABC (genetic)	M	13	Vo/Vo-VIM-STN/VIM/GPi1/GPi2
9	Kernicterus	M	15	VA/VoSTN/VIM/GPi1/GPi2
10	Cerebral Palsy (dyskinetic)	M	12	VA/VoSTN/VIM/GPi1/GPi2
11	Glutaric Aciduria Type I	M	13	VA/VoSTN/VIM/GPi1/GPi2
12	KMT2B (genetic)	M	10	VA/VoSTN/VIM/GPi1/GPi2

Abbreviations: F, female; M, male.

7.3.2 Stimulation protocol

Stimulations consisting of 90-us, 3-V pulses, at 9 or 25-Hz frequencies, were administered through two adjacent macro-contacts (anode and cathode) at a time.

7.3.3 Evoked potential detection

The ADPREP algorithm described in Chapter 3 was used to automate the detection of DBS EPs. Only EPs determined by this algorithm were included in the analysis of this project. Detected EPs were characterized by their peak-to-peak amplitude (P2P) and time-to-(first-)peak delay (T2P), and grouped within each micro-contact row for further analysis.

7.3.4 Image data acquisition

Preoperative T1-weighted structural MRI volumes were acquired from a MAGNETOM 3T MRI scanner (SIEMENS Medical System, Erlangen, Germany) for precise anatomical localization. The settings consisted of: repetition time (TR) 1800 ms, echo time (TE) 2.25 ms, flip angle 8°, voxel size 1 x 1 x 1 mm^3, and field of view (FOV) 240 x 240 mm^2. Preoperative diffusion-weighted imaging (DWI) sequences suitable for tractography were also acquired. Two echo planar imaging (EPI) sequences with opposite phase-encoded polarity calibration scans (anterior-posterior commissure, AC-PC, and posterior-anterior commissure, PC-AC) were acquired to correct the magnetic inhomogeneities. The parameters of the EPI sequence consisted of: TR 9000 ms, TE 113 ms, flip angle 90°, voxel size 2.5 × 2.5 × 2.5 mm^3, and FOV 250 x 250 mm^2. Two DTI scans were obtained with a b-value of 1000 s/mm^2 and 30 & 6 gradient directions in the anterior-to-posterior (AP) & posterior-to-anterior (PA) phase encodings, respectively, for future TOPUP distortion correction use. The entire brain was covered using 55 slices in each of the two scans. Postoperative computed tomography (CT) volumes were acquired from a GE (GENERAL ELECTRIC Healthcare, Milwaukee, WI, USA) scanner, providing images with a size of 512 x 512 x 320 mm to confirm electrode localization.

7.3.5 Image correction and registration

The phase-encoding direction is associated with two major artifacts: aliasing and motion. Aliasing occurs when the size of the anatomy exceeds the defined field-of-view (FOV) in the phase-encoding direction, which causes the anatomy outside the FOV to be folded in over the main part of the image. Although there are methods to remove artifacts such as phase-oversampling, sometimes additional phase-encoding measurements are required [92], [93]. To solve this

discrepancy, two diffusion MRI scans were acquired with AP and PA encoding directions for correction of phase encoding distortion. Although the distortions were improved when the EPI sequences were fitted between them, some distortions still remained and were further corrected with the TOP-UP algorithm [92], [94]. Furthermore, motion artifacts were corrected through Eddy-current corrections [95]. Once the distortions had been corrected, both CT and DWI volumes were realigned to the same plane, setting the origin of the image at the midpoint of the AC-PC line in the T1-weighted volumes.

7.3.6 Visualization of atlas

To visualize the atlas data with the electrode reconstruction results, the atlas data was read by the toolbox in standard nifti file format. Atlas data can be visualized as either 2D-slice views (sliced overlays on the MRI) or 3D-reconstructions. Here, we implemented the DISTAL atlas [96] in the DSI Studio visualization software. For the atlas visualization into individual or MNI space, we selected the nuclei of interest (such as GPi, STN, Voa/Vop, VA, VIM, and PPN) and thereafter applied a linear spatial transformation (Flirt tool from FSL). Through our work, we enabled the novel visualization of a binary atlas with data from children with injured brains, either in the DSI Studio package or FSLEYES, software programs that are widely used by the neuroimaging community (Figure 7.1).

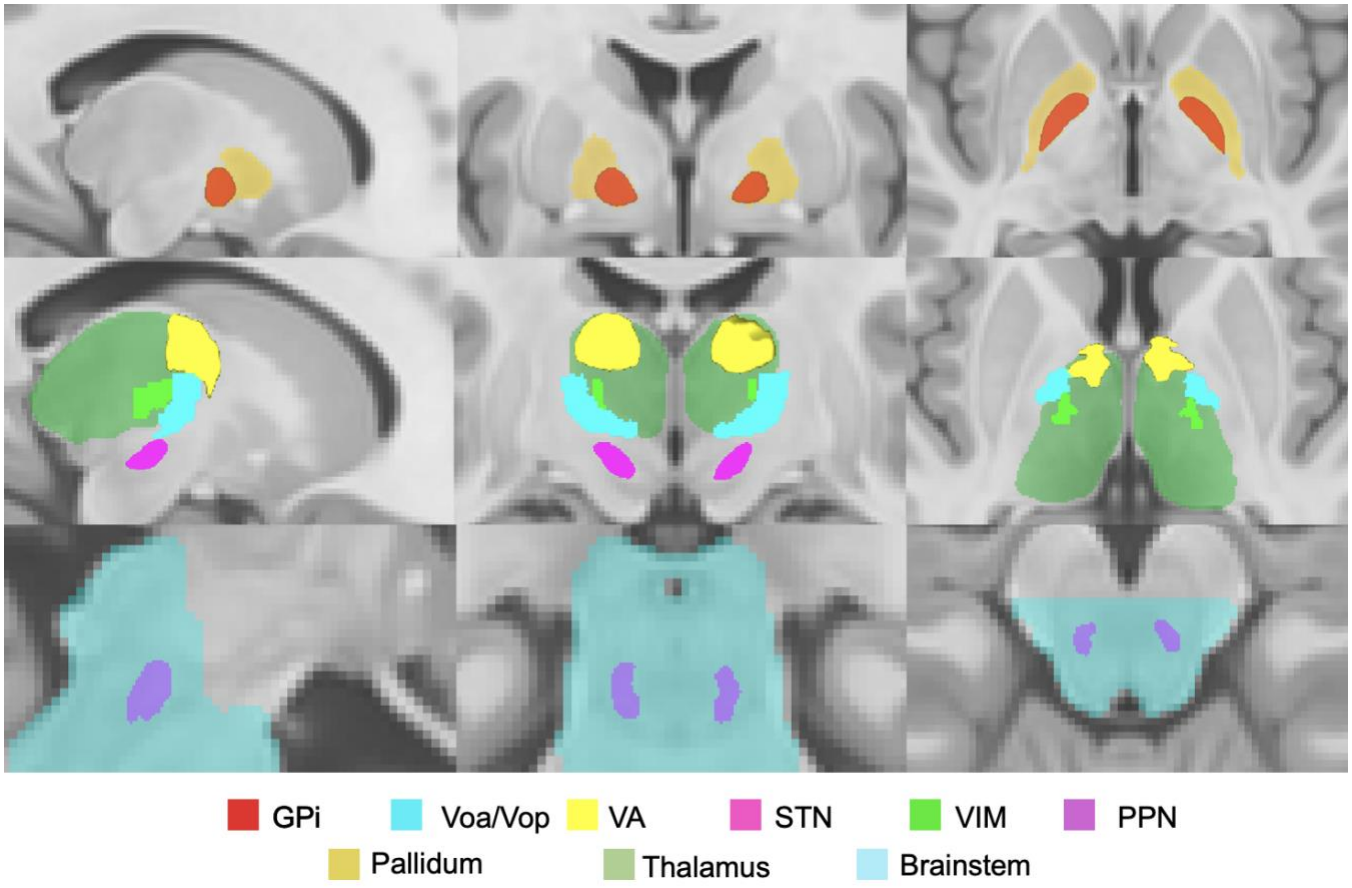

Figure 7.1. Deep brain structure atlas in MNI space. This image shows regions in the thalamus (VIM, Voa/Vop, and VA), basal ganglia (GPi [part of the pallidum] and STN), and brainstem (PPN).

7.3.7 DBS electrode trajectory reconstruction

To ensure optimal DBS treatment outcome, exact electrode placement is required. Moreover, to analyze the relationship between electrode location and clinical results, a precise reconstruction of electrode placement is necessary, posing specific challenges to the field of neuroimaging.

Once the CT scans were warped to the structural MRI volume and realigned to the AC-PC axis, the projection images were calculated. Due to the complexity of visualizing multiple DBS electrodes in the individual anatomy, we here introduce a new approach to place the electrode accurately based on projection images.

We calculated the maximum intensity projection (MIP), which consists of a projection of the voxel values – specifically, the highest attenuation value – onto a 2D image [97]. As a result, for each X-Y coordinate, only the pixel with the highest Hounsfield number along the Z-axis is represented, so that in a single bidimensional image, all dense structures in each volumetric area are observed. This approach generated a new semi-automatic method for localizing the DBS electrodes from the projection images, allowing us to obtain the spatial coordinates of the electrodes in a precise manner. Once the projection images were calculated to reconstruct the lead trajectory, the distal part (tip) of the electrodes could not be distinguished from contrast CT scans into structural MRI, so a linear interpolation was used to reconstruct the tip of the electrodes, corresponding to the first row of micro-contacts (Figure 7.2).

The volume of tissue activated (VTA) is a conceptual measure of tissue volume where the electrical stimulation of axons has elicited additional action potentials. Much work has been done in this field, and models with increasing sophistication have been introduced in recent years. In contrast, some more clinically oriented papers have aimed to use fast heuristics to determine the rough extent of the VTA based on stimulation parameters, without actually creating a spatial model. On a spectrum between a simple and highly sophisticated model, we used the metal artifacts of the macro-contacts to estimate the DTI source seeds (the sources of the upcoming tractography analysis). A histogram segmentation was applied in post-surgery CT scans with a threshold set to detect metal artifacts [98], in order to create the binary mask that finally provided the spatial localization of the macro-contacts of all DBS leads.

Since we also included electrophysiological data in the form of DBS EPs, we created target regions for the micro-contact rows as well. These regions were modeled as spheres around each micro-contact row in the area that we anticipated the micro-contacts to be recording from (Figure

7.2c). As the deep brain structures in children are smaller than in the adult brain, the diameter of these spheres was chosen to be 3 mm, according to the gray scales of CT volumes.

7.3.8 Seed selection

The macro-contact metal artifacts from the CT scans were visualized in DSI Studio and fused with the deep brain atlas. In order to select the seeds, we conducted a conjunction analysis between the deep brain atlas (normalized into MNI or individual structural MRI) and the metal artifacts. In this way, the macro-contact regions located within each nucleus were identified (Figure 7.3).

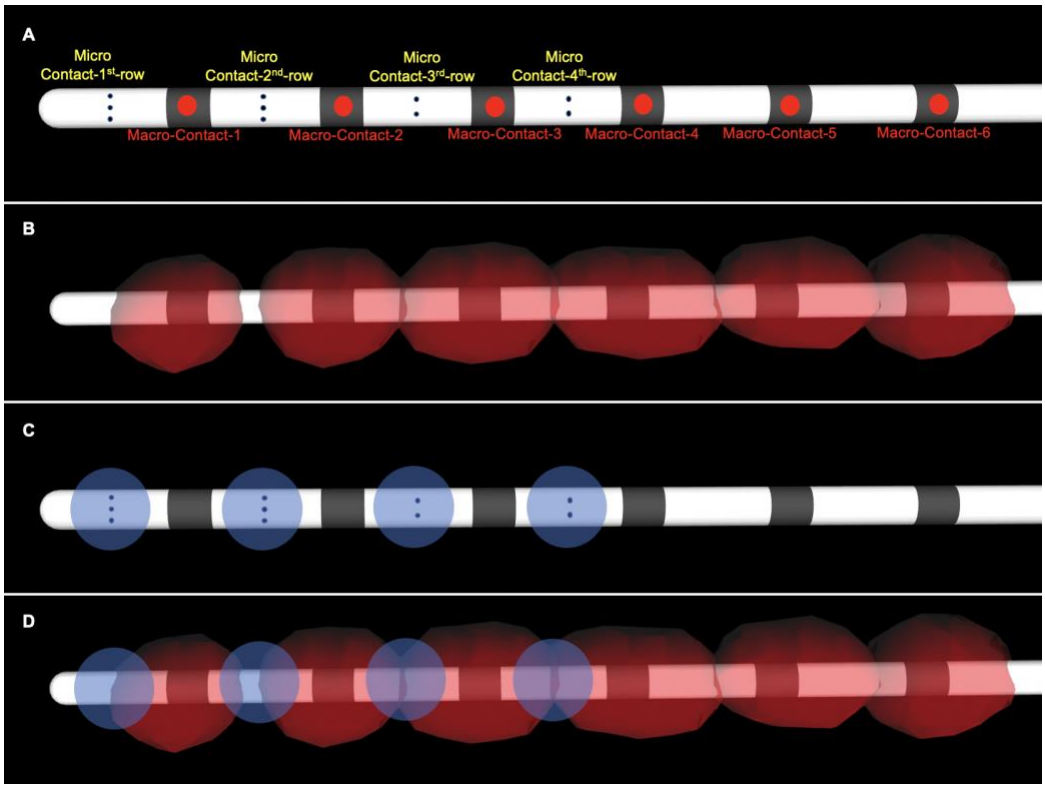

Figure 7.2. sEEG leads with sample macro-contact source regions and micro-contact target regions. The lead was reconstructed from CT scans using projection images and visualized in the DSI Studio package. (A) Lead specifications of the Ad-Tech MM16C sEEG lead. (B) Macro-contact source regions (red) detected from CT metal artifacts. (C) Micro-contact target regions (blue spheres) represent the estimated region that each micro-contact row can record from. (D) Representation of a reconstructed sEEG electrode with both macro- (red) and micro-contact regions (blue) visualized.

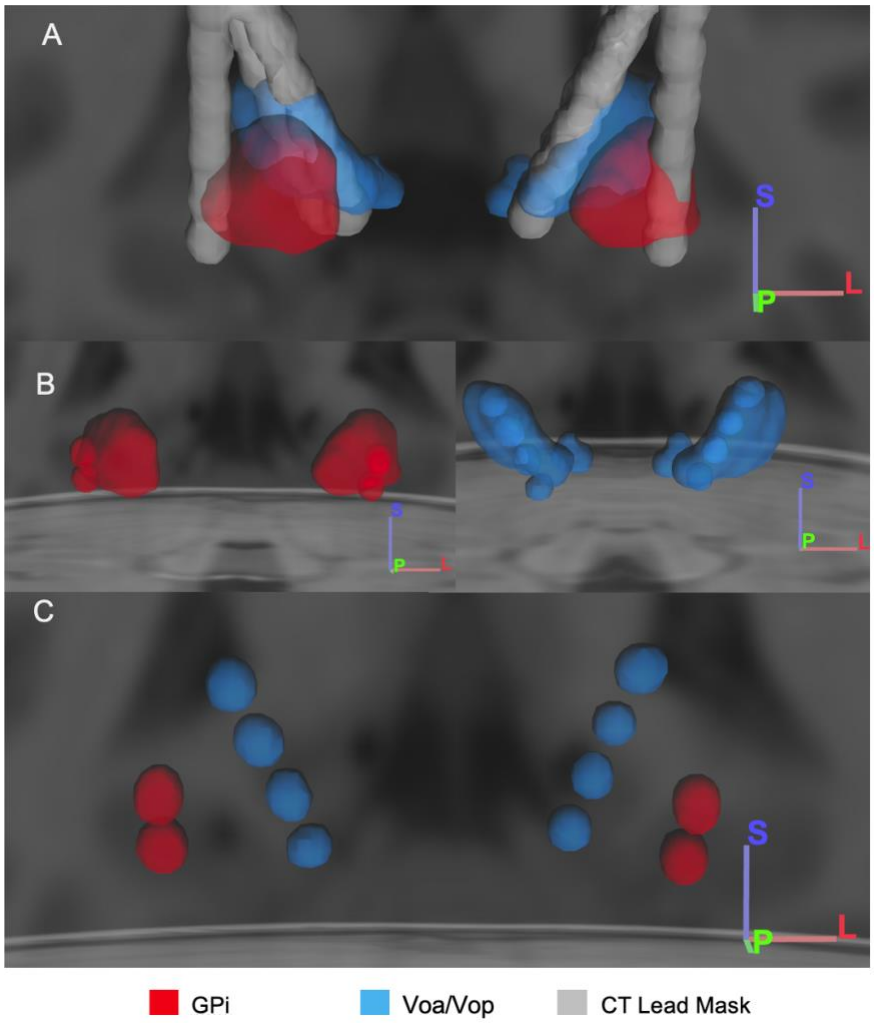

Figure 7.3. Visualization of the steps to determine source and target regions for tractography analysis. (A) DISTAL atlas normalized to individual anatomy, showing leads (gray) in deep brain regions corresponding to globus pallidus internus (GPi, red) and ventral oralis anterior/posterior (Voa/Vop, blue). (B) Spatial conjunction analysis between the CT scan and deep brain regions to determine which parts of the DBS electrode that are placed within GPi and Voa/Vop. (C) Source (red) and target (blue) region selection based on the conjunction analysis between the CT scan and atlas.

7.3.9 Diffusion tensor imaging

DWI was used to reconstruct the DTI [99], a method previously used to study fiber orientations and quantify diffusion characteristics. Q-space diffeomorphic reconstruction [100] was used for DTI fiber tracking in DSI Studio [101]. Quantitative anisotropy (QA) coefficients [102] were used

to determine the fiber tracking threshold. In each macro-contact region (Figure 7.2b), seeds were randomly generated with an average number of 1000 seeds per voxel, with a step size of 0 (1 mm^3 voxel distance), a turning angle of 10°, and QA > 0.0, in order to detect more fiber tracts.

Fiber tracking was performed between all stimulating and recording regions, for all subjects.

7.3.10 Generalized linear model

The characteristics of each fiber tract can be quantified by DTI coefficients (including tract length, tract volume, and FA), while EPs can be characterized by their peak-to-peak amplitude (P2P) and time-to-(first-)peak delay (T2P). We aimed to explain the relationship between these EP characteristics and DTI coefficients with generalized linear models (GLM). These linear models were defined as follows:

$$P2P = C_{FA} * DTI_{FA} + C_l * DTI_l + C_V * DTI_V + C_{\text{int}} \quad (7.1)$$

$$T2P = C_{FA} * DTI_{FA} + C_l * DTI_l + C_V * DTI_V + C_{\text{int}} \quad (7.2)$$

where, for each model, DTI_{FA}, DTI_l, and DTI_V are the DTI coefficients of FA value, tract length, and tract volume, respectively; C_{FA}, C_l, and C_V are the estimation coefficients relating these DTI coefficients to the EP characteristics (P2P amplitude and T2P delay); and C_{int} is the intercept of the model.

7.4 Results

To quantify the relationships between EPs and anatomical features, we calculated the averages of the DTI coefficients, including FA, fiber tract length, and fiber tract volume, using the tract analysis

tool provided by DSI Studio. All values were interpolated by a 3D linear model on the tract lines. (We did not use the number of tracts in our analysis, as this value is easily affected by the user-selected fiber tracking parameters.)

7.4.1 Individual analysis

For visualization purposes, individual analysis was performed on one subject prior to the group analysis (Figure 7.4), focusing on the connection between GPi and Voa/Vop, a neural connection that is important in the control of movement. In these individual results, we saw a clear relation between FA (a main marker of brain white matter integrity) and the T2P & P2P values. FA was found to be positively correlated with P2P amplitude, and negatively correlated with T2P, both statistically significant. This highlights how white matter integrity affects signal transfer: a high integrity neural pathway seems to enable a stronger and faster signal transmission, and vice versa.

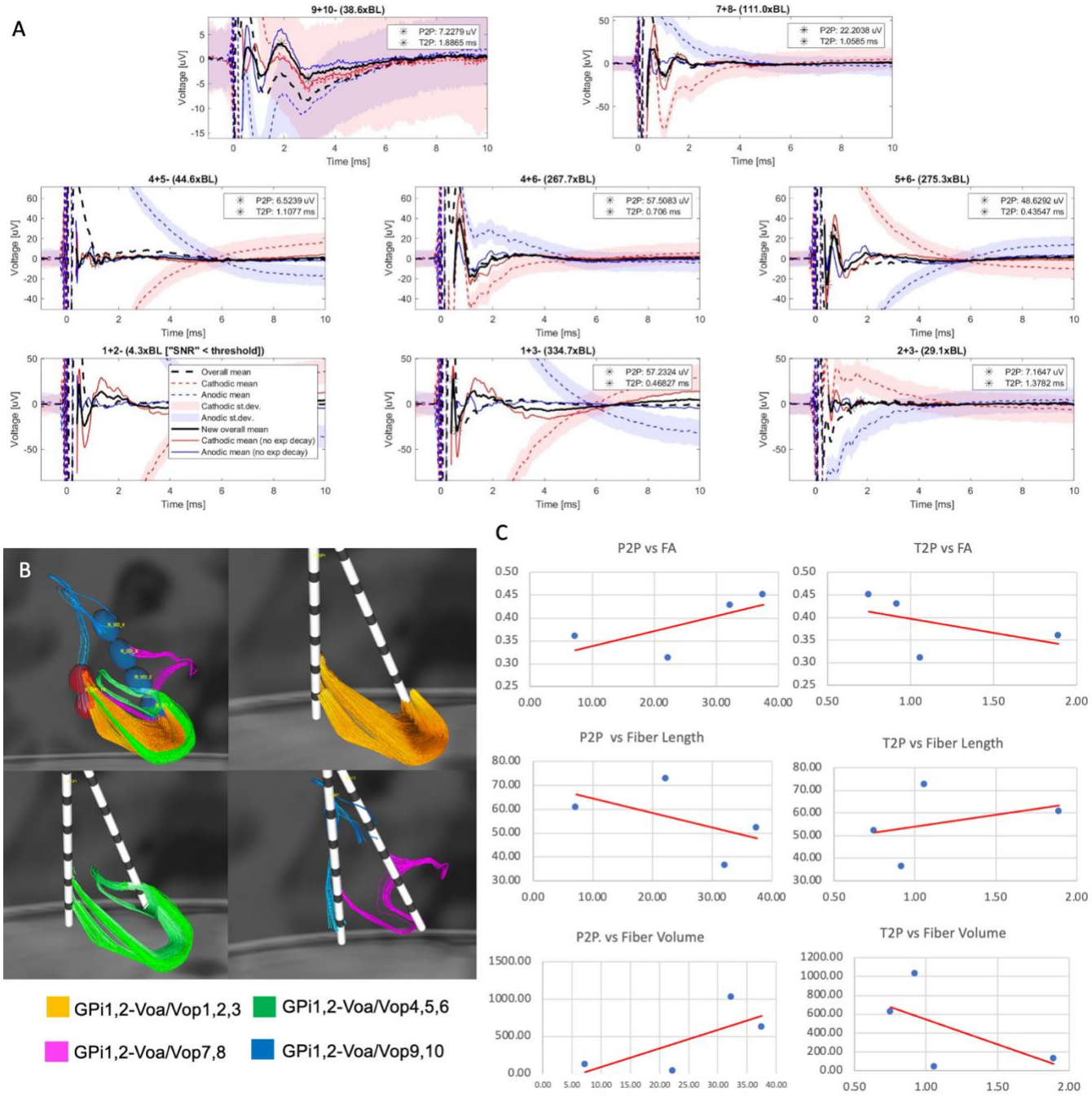

Figure 7.4. Sample results from the DTI-EP correlation analysis in one subject, between GPi and Voa/Vop. (A) Neural recordings from micro-contacts in Voa/Vop during 25-Hz GPi DBS. (B) Fiber tracking between macro-contacts in GPi (stimulation) and micro-contact rows in Voa/Vop (recording). Yellow, green, pink, and blue fibers correspond to tracts from macro-contacts 1 & 2 (the macro-contact pair closest to the tip of the lead) in GPi to micro-contacts 1-3 (first row from the tip of the lead), 4-6 (second row), 7-8 (third row), and 9-10 (fourth row), respectively, in Voa/Vop. (C) Scatter plots with trend lines showing correlations between EP characteristics (T2P & P2P; left & right columns, respectively)

and DTI coefficients (FA, length, and volume of fiber tracts, from top to bottom). Each data point represents one of the four different connections from the macro-contacts in GPi to the micro-contacts in Voa/Vop (different colored tracts in subplot B). Note how P2P amplitude seems to correlate positively with FA and fiber volume, but negatively with fiber length, while the opposite is true for T2P delay.

7.4.2 Group analysis

The group analysis results of the linear models relating DTI coefficients to EP amplitude (P2P) and delay (T2P) are displayed in Table 7.2. P2P displayed significant *positive* correlations with FA and tract volume, but a *negative* correlation with tract length (Table 7.2, left block). Conversely, T2P displayed significant *negative* correlations with FA and tract volume (Table 7.2, right block; no significant correlation with tract length).

Table 7.2. Generalized linear model results: EP amplitude (P2P, left block) and delay (T2P, right) vs. DTI coefficients.

	$P2P = C_{FA} * DTI_{FA} + C_l * DTI_l + C_V * DTI_V + C_{int}$				$T2P = C_{FA} * DTI_{FA} + C_l * DTI_l + C_V * DTI_V + C_{int}$			
	Estimate	*SE*	*tStat*	*p-value*	*Estimate*	*SE*	*tStat*	*p-value*
C_{FA}	**78.059**	10.057	7.762	< 0.001	**-1.0616**	0.20172	-5.2626	<0.001
C_l	**-0.24556**	0.036891	-6.6564	< 0.001	-0.0004514	0.00073997	-0.61005	0.54189
C_V	**0.010145**	0.0047645	2.1292	< 0.05	**-0.0003003**	9.56E-05	-3.1426	<0.05
C_{int}	2.4077	4.9727	0.48419	0.6283	**1.9435**	0.099744	19.485	<0.001

DTI_{FA}, DTI_l, DTI_V: DTI coefficients of FA value, tract length, and tract volume, respectively. C_{FA}, C_l, C_V: estimation coefficients relating DTI coefficients to EP characteristics (P2P amplitude and T2P delay). C_{int}: intercept of model. SE: Standard error. Significant estimates shown in bold. Distribution: normal. 2115 observations; 2111 error degrees of freedom. Estimated Dispersion: 3500 (P2P), 1410 (T2P). F-statistic vs. constant model: 42.4 (P2P), 11.6 (T2P); both p < 0.001.

7.5 Discussion

In this combined imaging and electrophysiology study, we determined the characteristic relationship between the anatomical features described by the tractography (DTI) and

electrophysiology (DBS EPs) of pediatric patients with dystonia. At present, for 12 patients undergoing DBS surgery, we not only continuously collected the in-vivo electrophysiological signals of the patients, but also used tractography to detect the signal conduction path, thereby determining the relationship between the evoked potentials and anatomical features.

The outcome of DBS treatment critically depends on the accurate localization of DBS target areas [103], such as GPi, STN, VIM, VA and Voa/Vop. The localization of these regions relies on indirect methods, which in turn may rely on standard coordinates (MNI), without considering individual differences in thalamic locations and structures [104]–[106]. This may lead to different – and non-optimized – outcomes after DBS surgery [107]–[109]; thus, there is an urgent need for reliable and precise methods for determining DBS targets. Although some techniques for MRI imaging have been proposed [106], [109], none of them have been applied to clinical procedures [108].

Typical DBS targets include sub-regions of globus pallidus and the thalamus, which can be complex to identify through structural MRI. We have solved this problem for the first time by segmenting the voxels of the pallidum and thalamus in grayscale in individual space, and thereafter normalizing them into MNI space. An entire pipeline has been presented here for the neuroimaging of pediatric brains in particular. We introduced a semi-automated procedure to reconstruct our leads based on projection images. Analysis of a group of patients (N = 12) showed that the procedure can improve the trajectory localization based on postoperative CT-images. Moreover, we used nonlinear and linear spatial transformations to warp the CT-image and DTI volumes into an individual structural MRI (which works for both T1 and T2 weighted images) and normalized them into MNI space without loss of information during the spatial transformation.

We presented a novel way to reconstruct and visualize multiple DBS electrodes in the well-known and widely used DSI Studio package, with DTI and structural MRI images. Furthermore, the atlas for deep brain regions was added to DSI Studio to obtain specific locations for each lead, for both macro-contacts and rows of micro-contacts. With these innovations, we are able to track the fibers from specific contacts for both individual as well MNI space, providing information about the fiber tracts in deep regions of children with brain injury, which has not been done before.

To test the reliability of our process, tracking between sEEG leads was performed for a group of 12 pediatric patients with dystonia. As a result of the tracking, values for FA, length and volume of tracts were calculated. The DTI coefficients were used to relate the tractography results with EPs recorded during 9- or 25-Hz intracranial DBS through a GLM.

As expected, the results showed a significant correlation between DTI coefficients and electrophysiological characteristics. The GLM showed that EP amplitude (P2P) was positively related to FA and tract volume; inversely, EP delay (T2P) was *negatively* related to both of these measures. Additionally, P2P was found to be negatively related to tract length (T2P showed no significant relation to tract length).

The inverse relations that P2P and T2P have to FA and tract volume (P2P showing positive relations to both while T2P showed negative relations to both) met some expectations set forth from the results presented in Chapter 4: when stimulation frequency increases, EP delay (T2P) tends to increase, while EP amplitude (P2P) decreases. This suggests some sort of inverse relation between T2P and P2P, at least in terms of stimulation frequency; as such, we may expect to see such an inverse relation with regard to physiological measurements as well.

FA is a measure of anisotropic movement of water molecules in fiber tracts, and is as such a good indicator of white matter integrity (with larger FA values representing good integrity) [110].

Hence, our results imply that the strength and time required for the transmission of the electrical signal are affected by the integrity of the white matter of the brain: high-quality white matter (characterized by large FA values) allows neural signals to arrive with shorter delays and larger amplitudes, and vice versa. It is also intuitive that fiber tracts with greater volume would lead to faster transmission, as this is in line with cable theory: larger diameter axons have less electrical resistance, and can as such transmit action potentials faster [111]. This decreased resistance may also lead to a reduction in potential data loss along the way, hence causing the retention of EP amplitude. Similarly, one could expect that data loss happens gradually throughout the transmission of the EP through the fiber tracts, resulting in smaller amplitudes the farther an EP must travel; as such, the negative relation between P2P and tract length could be expected.

The one *non*-significant relation between the EP characteristics and the DTI coefficients, EP delay (T2P) versus tract length, may be the one we had *first* expected to be significantly correlated. Namely, EP delay is related to fiber length and conduction velocity through the equation of *delay=length/velocity*; hence, longer fiber tracts should lead to longer EP delays. This should as such translate to a positive relation between T2P and tract length – but no significant relation was detected in our GLM models. However, this postulation assumes constant conduction velocity, which, as we have already discussed, is not a universally true assumption. It is hence possible that other factors such as variation in conduction velocity, sample size, and dystonic pathology in the subject group may explain why this relation was not noted in our analysis.

Apart from this, the significant results in this study could be logically explained based on physiological expectations, which makes us optimistic that these findings may be true not only for dystonic patients, but potentially also in healthy brains. However, as our methods to collect information about the intracranial EP delays and amplitudes are invasive, we are currently unable

to confirm this generalization. Nevertheless, we hope that non-invasive methods may be developed to allow us to do so in the future.

7.6 Conclusion

We have demonstrated that a quantification of the relationship between electrophysiological signals and white matter integrity is possible using techniques such as DTI and sEEG recordings during DBS. Through the development of GLMs, we validated the methods of tractography against ground truth electrophysiology, and discovered significant correlations between the characteristics of neural tracts and neural responses to electrical stimulation in deep brain structures.

Future work in this project involves increasing sample size, including additional model input variables, and incorporating models of machine learning and deep learning to investigate and understand these findings further. Improvements like these may provide a version of our mathematical model with the potential to predict DBS EP characteristics (e.g., amplitude and delay) using only DTI coefficients. Such an ability to infer DBS EPs from DTI coefficients of fiber tracts would open up new possibilities for cases when intracranial deep brain recordings are not possible or available. The proposed mathematical model may then be used not only to describe the relationship between DBS EPs and the connectivity of white matter, but potentially also indicate which of the DTI indices is most predictive of electrical connectivity, and noninvasively predict optimal DBS lead implant targets.

SUMMARY & CONCLUSION

This dissertation aimed to study signal flow and the effects of electrical stimulation in dystonic basal ganglia and thalamic nuclei. Each of these areas of increased knowledge will provide vital information for the development of ideal stimulation treatments for movement disorders. While further investigation is required, I have shed light onto signal flow in the human brain and the mechanism of dystonia by developing experimental and data-processing techniques with which to probe the human brain connectome.

Recordings were gathered from sEEG leads to detect neural responses evoked by intracranial and peripheral stimulation in the dystonic brain. In order to observe both the steady state and transient neural responses, stimulations were delivered both as continuous pulse trains (providing insight into the *average* neural response) and intermittent stimulation bursts (allowing us to study the initial *build-up* of the neural response throughout the bursts). Stimulations at different rates were also administered to determine the effect of stimulation frequency on connectivity.

Findings from burst stimulations showed that transient responses differ from steady state, revealing increasing EP correlations throughout peripheral bursts, and increasing amplitudes of oscillatory EPs throughout intracranial bursts. We hypothesized that these trends are the result of successive neural recruitment to repetitive stimulations, and developed a Kuramoto-based model to explain the latter finding on the basis of couplings between neural populations. While steady state responses from constant stimulation trains were found to evoke highly intricate and consistent neural responses, the delay, amplitude, and even shape of the response appears to be frequency dependent. Moreover, I found that DBS EPs are affected by the intake of medications in

a surprisingly heterogeneous pattern, and also noticed correlations between our invasive neurophysiological recordings and non-invasive imaging methods.

Through my extensive work developing codes, I have created methods to accurately process our data, remove noise and artifacts, and automate processes that could otherwise insert human bias and take valuable time that could be put to better use deciphering patterns and drawing conclusions from the data. This has allowed me to study the temporal and spatial electrophysiological effects of DBS in human deep brain structures in an in-depth and reliable manner that is unique in comparison to many other studies with limited experimental time and/or access to human data.

This dissertation research has provided insight into the neural response to electrical stimulation in patients with movement disorders, leading to a greater understanding of both the signal flow in deep brain regions and how electrical stimulation can modulate this flow. Both of these components are crucial in the development of more effective electrical stimulation treatments, not only for dystonic patients, but also for other diseases currently treated by such methods (including epilepsy, PD, and ET), as well as psychiatric disorders currently under investigation for DBS treatment (such as depression, Alzheimer's disease, and obsessive-compulsive disorder) [12]. Further understanding of the brain's response to electrical stimulation will also enable better use of closed-loop DBS, an area of increasing interest [12]. My new analytical methods, signal processing tools, and models, developed in order to answer these clinical questions, have hereby also added an important contribution to the signal processing and engineering fields.

Electrical stimulation has the potential to effectively treat brain disorders. However, as with any tool, it is only as useful as its operator is skilled, and for optimal use, the operator must

both know *what* to do, and *how* to do so. By studying the abnormal signal flow that causes dystonia, we can determine what needs to be fixed, and by studying the effects of electrical stimulation, we can learn how to control the response pattern to generate the desired effect for each individual patient. While this dissertation cannot not fully answer these questions, it has made significant progress to guide the development of new stimulation protocols to increase treatment efficacy for children with dystonia and other movement disorders.

BIBLIOGRAPHY

1. G. Buonocore *et al.*, “Cerebral Palsy-Trends in epidemiology and Recent Development in Prenatal Mechanisms of Disease, Treatment, and Prevention,” vol. 5, p. 1, 2017.

2. T. D. Sanger, “Toward a definition of childhood dystonia.,” *Curr. Opin. Pediatr.*, vol. 16, no. 6, pp. 623–627, Dec. 2004.

3. T. D. Sanger *et al.*, *Definition and classification of negative motor signs in childhood*, vol. 118, no. 5. Am Acad Pediatrics, 2006, pp. 2159–2167.

4. T. D. Sanger, “Basic and translational neuroscience of childhood-onset dystonia: A control-theory perspective,” *Annual Review of Neuroscience*, vol. 41. Annual Reviews, pp. 41–59, 2018.

5. J. W. Mink, “The basal ganglia: Focused selection and inhibition of competing motor programs,” *Prog. Neurobiol.*, vol. 50, no. 4, pp. 381–425, 1996.

6. T. D. Sanger, “Deep brain stimulation for cerebral palsy: where are we now?,” *Dev. Med. Child Neurol.*, vol. 62, no. 1, pp. 28–33, 2020.

7. E. E. Benarroch, “Effects of acetylcholine in the striatum,” *Neurology*, vol. 79, no. 3, pp. 274 LP – 281, Jul. 2012.

8. M. Kasiri, S. Javadzadeh, J. Nataraj, S. A. Seyyed Mousavi, and T. Sanger, “Correlated activity in globus pallidus and thalamus during voluntary reaching movement in three children with primary dystonia,” *Dystonia*, vol. 0, p. 7, Feb. 2023.

9. P. A. Starr *et al.*, “Microelectrode-guided implantation of deep brain stimulators into the

globus pallidus internus for dystonia: techniques, electrode locations, and outcomes," *J. Neurosurg.*, vol. 104, no. 4, pp. 488–501, Apr. 2006.

10. T. Schönecker *et al.*, "Postoperative MRI localisation of electrodes and clinical efficacy of pallidal deep brain stimulation in cervical dystonia," *J. Neurol. Neurosurg. Psychiatry*, vol. 86, no. 8, pp. 833 LP – 839, Aug. 2015.

11. T. Cheung, A. M. Noecker, R. L. Alterman, C. C. McIntyre, and M. Tagliati, "Defining a therapeutic target for pallidal deep brain stimulation for dystonia.," *Ann. Neurol.*, vol. 76, no. 1, pp. 22–30, Jul. 2014.

12. J. K. Krauss *et al.*, *Technology of deep brain stimulation: current status and future directions*, vol. 17, no. 2. 2021.

13. F. Klostermann, T. Funk, J. Vesper, and G. Curio, "Spatiotemporal characteristics of human intrathalamic high-frequency (> 400 Hz) SEP components," *Neuroreport*, vol. 10, no. 17, pp. 3627–3631, 1999.

14. J. Bending and L. Cleeves, "Effect of electrical nerve stimulation on dystonic tremor," *Lancet*, vol. 336, no. 8727, pp. 1385–1386, 1990.

15. M. Tinazzi *et al.*, "Effects of transcutaneous electrical nerve stimulation on motor cortex excitability in writer's cramp: neurophysiological and clinical correlations," *Mov. Disord. Off. J. Mov. Disord. Soc.*, vol. 21, no. 11, pp. 1908–1913, 2006.

16. E. Hernandez-Martin, E. Arguelles, Y. Zheng, R. Deshpande, and T. D. Sanger, "High-fidelity transmission of high-frequency burst stimuli from peripheral nerve to thalamic nuclei in children with dystonia," *Sci. Rep.*, vol. 11, no. 1, pp. 1–10, 2021.

17. R. Pahwa *et al.*, “An Acute Randomized Controlled Trial of Noninvasive Peripheral Nerve Stimulation in Essential Tremor,” *Neuromodulation*, vol. 22, no. 5, pp. 537–545, 2019.

18. M. A. Chalah, J.-P. Lefaucheur, and S. S. Ayache, “Non-invasive Central and Peripheral Stimulation: New Hope for Essential Tremor?,” *Front. Neurosci.*, vol. 9, p. 440, Nov. 2015.

19. E. Sandoval, “Cala Health Receives FDA Breakthrough Device Designation for Cala Trio™ Therapy to Treat Action Tremors in Parkinson’s Disease,” *Business Wire*, 22-Oct-2020.

20. T. D. Sanger *et al.*, “Pediatric deep brain stimulation using awake recording and stimulation for target selection in an inpatient neuromodulation monitoring unit,” *Brain Sci.*, vol. 8, no. 7, 2018.

21. T. D. Sanger, “Pathophysiology of pediatric movement disorders,” *J. Child Neurol.*, vol. 18, no. SUPPL. 1, pp. 9–24, 2003.

22. T. D. Sanger, “A Computational Model of Deep-Brain Stimulation for Acquired Dystonia in Children,” *Front. Comput. Neurosci.*, vol. 12, Sep. 2018.

23. T. Wichmann and J. O. Dostrovsky, “Pathological basal ganglia activity in movement disorders,” *Neuroscience*, vol. 198. pp. 232–244, 15-Dec-2011.

24. T. D. Sanger, D. Tarsy, and A. Pascual-Leone, “Abnormalities of spatial and temporal sensory discrimination in writer’s cramp,” *Mov. Disord.*, vol. 16, no. 1, pp. 94–99, 2001.

25. T. D. Sanger and S. N. Kukke, “Abnormalities of tactile sensory function in children with dystonic and diplegic cerebral palsy,” *J. Child Neurol.*, vol. 22, no. 3, pp. 289–293, 2007.

26. T. D. Sanger and M. M. Merzenich, “Computational model of the role of sensory

disorganization in focal task-specific dystonia," *J. Neurophysiol.*, vol. 84, no. 5, pp. 2458–2464, 2000.

27. L. Cif and P. Coubes, "Historical developments in children's deep brain stimulation," *Eur. J. Paediatr. Neurol.*, vol. 21, no. 1, pp. 109–117, 2017.

28. E. Hernandez-Martin, E. Arguelles, R. Deshpande, and T. D. Sanger, "Evoked Potentials During Peripheral Stimulation Confirm Electrode Location in Thalamic Subnuclei in Children With Secondary Dystonia," *J. Child Neurol.*, p. 0883073820931970, Jun. 2020.

29. F. Klostermann, R. Gobbele, H. Buchner, and G. Curio, "Dissociation of human thalamic and cortical SEP gating as revealed by intrathalamic recordings under muscle relaxation," *Brain Res.*, vol. 958, no. 1, pp. 146–151, 2002.

30. F. Shima, T. Morioka, S. Tobimatsu, O. Kavaklis, M. Kato, and M. Fukui, "Localization of stereotactic targets by microrecording of thalamic somatosensory evoked potentials," *Neurosurgery*, vol. 28, no. 2, pp. 223–230, 1991.

31. F. Klostermann, J. Vesper, and G. Curio, "Identification of target areas for deep brain stimulation in human basal ganglia substructures based on median nerve sensory evoked potential criteria," *J. Neurol. Neurosurg. Psychiatry*, vol. 74, no. 8, pp. 1031–1035, 2003.

32. D. Regan, "Some early uses of evoked brain responses in investigations of human visual function," *Vision Res.*, vol. 49, no. 9, pp. 882–897, May 2009.

33. V. Mäkinen, P. May, and H. Tiitinen, "Transient brain responses predict the temporal dynamics of sound detection in humans," *Neuroimage*, vol. 21, no. 2, pp. 701–706, Feb. 2004.

34. A. Capilla, P. Pazo-Alvarez, A. Darriba, P. Campo, and J. Gross, "Steady-State Visual Evoked

Potentials Can Be Explained by Temporal Superposition of Transient Event-Related Responses," *PLoS One*, vol. 6, no. 1, 2011.

35. D. Regan, *Human brain electrophysiology: Evoked potentials and evoked magnetic fields in science and medicine*. Elsevier C Publisher, 1989.

36. J. S. L. Vidmark, E. Hernandez-Martin, and T. D. Sanger, "Increasing Consistency of Evoked Response in Thalamic Nuclei During Repetitive Burst Stimulation of Peripheral Nerve in Humans," in *Medical Image Computing and Computer Assisted Intervention – MICCAI 2021*, vol. 12908, M. de Bruijne, P. C. Cattin, S. Cotin, N. Padoy, S. Speidel, Y. Zheng, and C. Essert, Eds. Cham, Switzerland: Springer International Publishing, 2021, pp. 238–247.

37. A. Brand, L. Allen, M. Altman, M. Hlava, and J. Scott, "Beyond authorship: Attribution, contribution, collaboration, and credit," *Learn. Publ.*, vol. 28, no. 2, pp. 151–155, 2015.

38. L. McLean, R. N. Scott, and P. A. Parker, "Stimulus Artifact Reduction in Evoked Potential Measurements," *Arch Phys Med Rehabil*, vol. 77, no. December, pp. 1286–1292, 1996.

39. Y. Hua, D. F. Lovely, and R. Doraiswami, "Factors affecting the stimulus artifact tail in surface-recorded somatosensory-evoked potentials," *Med. Biol. Eng. Comput.*, vol. 44, no. 3, pp. 226–241, 2006.

40. R. Hanajima *et al.*, "Very fast oscillations evoked by median nerve stimulation in the human thalamus and subthalamic nucleus," *J. Neurophysiol.*, vol. 92, no. 6, pp. 3171–3182, 2004.

41. T. Morioka, F. Shima, M. Kato, and M. Fukui, "Origin and distribution of thalamic somatosensory evoked potentials in humans," *Electroencephalogr. Clin. Neurophysiol.*, vol. 74, no. 3, pp. 186–193, 1989.

42. R. Hanajima, J. O. Dostrovsky, A. M. Lozano, and R. Chen, “Dissociation of thalamic high frequency oscillations and slow component of sensory evoked potentials following damage to ascending pathways,” *Clin. Neurophysiol.*, vol. 117, no. 4, pp. 906–911, 2006.

43. N. Kim *et al.*, “Activation of the thalamic parafascicular nucleus by electrical stimulation of the peripheral vestibular nerve in rats,” *Exp. Brain Res.*, vol. 235, no. 5, pp. 1617–1625, 2017.

44. N. C. Sinclair *et al.*, “Deep brain stimulation for Parkinson’s disease modulates high-frequency evoked and spontaneous neural activity,” *Neurobiol. Dis.*, vol. 130, pp. 384–388, 2019.

45. E. P. Casula *et al.*, “TMS-evoked long-lasting artefacts: A new adaptive algorithm for EEG signal correction,” *Clin. Neurophysiol.*, vol. 128, no. 9, pp. 1563–1574, 2017.

46. G. Arslan, “Exponential and Sinusoidal Signals,” 2009. [Online]. Available: http://www2.hawaii.edu/~gurdal/EE315/class2.pdf.

47. R. M. Hirsch and J. R. Slack, “A Nonparametric Trend Test for Seasonal Data With Serial Dependence,” *Water Resour.*, vol. 20, no. 6, pp. 727–732, 1984.

48. N. C. Sinclair *et al.*, “Subthalamic nucleus deep brain stimulation evokes resonant neural activity,” *Ann. Neurol.*, vol. 83, no. 5, pp. 1027–1031, 2018.

49. C. Chu Chen, A. A. Kühn, T. Trottenberg, A. Kupsch, G. H. Schneider, and P. Brown, “Neuronal activity in globus pallidus interna can be synchronized to local field potential activity over 3-12 Hz in patients with dystonia,” *Exp. Neurol.*, vol. 202, no. 2, pp. 480–486, 2006.

50. L. L. Rubchinsky, C. Park, and R. M. Worth, “Intermittent neural synchronization in Parkinson’s disease,” *Nonlinear Dyn.*, vol. 68, no. 3, pp. 329–346, 2012.

51. D. Nesterovich Anderson, A. D. Dorval, J. D. Rolston, S. M. Pulst, and C. J. Anderson, "Computational investigation of the impact of deep brain stimulation contact size and shape on neural selectivity," *J. Neural Eng*, vol. 18, p. 56004, 2021.

52. A. R. Kent and W. M. Grill, "Analysis of deep brain stimulation electrode characteristics for neural recording," *J. Neural Eng*, vol. 11, p. 12, 2014.

53. M. Zijlmans *et al.*, "How to record high-frequency oscillations in epilepsy: A practical guideline," *Epilepsia*, vol. 58, no. 8. pp. 1305–1315, 2017.

54. R. Hanajima *et al.*, "Somatosensory evoked potentials (SEPs) recorded from deep brain stimulation (DBS) electrodes in the thalamus and subthalamic nucleus (STN)," *Clin. Neurophysiol.*, vol. 115, no. 2, pp. 424–434, 2004.

55. A. R. Kent, B. D. Swan, D. T. Brocker, D. A. Turner, R. E. Gross, and W. M. Grill, "Measurement of evoked potentials during thalamic deep brain stimulation," *Brain Stimul.*, vol. 8, no. 1, pp. 42–56, 2015.

56. N. C. Sinclair, J. B. Fallon, K. J. Bulluss, W. Thevathasan, and H. J. McDermott, "On the neural basis of deep brain stimulation evoked resonant activity," *Biomed. Phys. Eng. Express*, vol. 5, no. 5, 2019.

57. S. L. Schmidt, D. T. Brocker, B. D. Swan, D. A. Turner, and W. M. Grill, "Evoked potentials reveal neural circuits engaged by human deep brain stimulation," *Brain Stimul.*, vol. 13, no. 6, pp. 1706–1718, 2020.

58. T. D. Sanger, A. Robison, E. Arguelles, D. Ferman, and M. Liker, "Case Report: Targeting for Deep Brain Stimulation Surgery Using Chronic Recording and Stimulation in an Inpatient

Neuromodulation Monitoring Unit, With Implantation of Electrodes in GPi and Vim in a 7-Year-Old Child With Progressive Generalized Dystonia," *J. Child Neurol.*, vol. 33, no. 12, pp. 776–783, 2018.

59. E. Arguelles, "On the Electrophysiology of Multielectrode Recordings of The Basal Ganglia and Thalamus to Improve DBS Therapy for Children with Secondary Dystonia by," 2020.

60. K. Kumaravelu, C. S. Oza, C. E. Behrend, and W. M. Grill, "Model-based deconstruction of cortical evoked potentials generated by subthalamic nucleus deep brain stimulation," *J. Neurophysiol.*, vol. 120, no. 2, pp. 662–680, Aug. 2018.

61. D. Freche, J. Naim-Feil, A. Peled, N. Levit-Binnun, and E. Moses, *A quantitative physical model of the TMS-induced discharge artifacts in EEG*, vol. 14, no. 7. 2018.

62. D. J. Mack, "movcorr(x, y, k, varargin): Compute windowed correlation coefficient," *MATLAB Central File Exchange*, 2023. [Online]. Available: https://www.mathworks.com/matlabcentral/fileexchange/65342-movcorr-x-y-k-varargin-compute-windowed-correlation-coefficient. [Accessed: 24-Jan-2023].

63. L. F. Berro, J. S. Overton, J. A. Reeves-Darby, and J. K. Rowlett, "Alprazolam-induced EEG spectral power changes in rhesus monkeys: a translational model for the evaluation of the behavioral effects of benzodiazepines," *Psychopharmacology (Berl).*, vol. 231, pp. 1373–1386, 2021.

64. H. Van Lier, W. H. I. M. Drinkenburg, Y. J. W. Van Eeten, and A. M. L. Coenen, "Effects of diazepam and zolpidem on EEG beta frequencies are behavior-specific in rats," *Neuropharmacology*, vol. 47, pp. 163–174, 2004.

65. C. H. Bastien, M. LeBlanc, J. Carrier, and C. M. Morin, “Sleep EEG power spectra, insomnia, and chronic use of benzodiazepines,” *Sleep*, vol. 26, no. 3, pp. 313–317, 2003.

66. S. G. Mallat, “Multiresolution approximations and wavelet orthonormal bases of L2(R),” *Trans. Am. Math. Soc. Am. Math. Soc.*, vol. 315, no. 1, 1989.

67. M. Frigo and S. G. Johnson, “FFTW: an adaptive software architecture for the FFT,” in *Proceedings of the 1998 IEEE International Conference on Acoustics, Speech and Signal Processing, ICASSP ’98 (Cat. No.98CH36181)*, 1998, vol. 3, pp. 1381–1384 vol.3.

68. J. L. Vitek, “Pathophysiology of dystonia: a neuronal model,” *Mov. Disord.*, vol. 17 Suppl 3, no. SUPPL. 3, 2002.

69. C. K. E Moll *et al.*, “Asymmetric pallidal neuronal activity in patients with cervical dystonia,” 2014.

70. W. J. Neumann *et al.*, “A localized pallidal physiomarker in cervical dystonia,” *Ann. Neurol.*, vol. 82, no. 6, pp. 912–924, Dec. 2017.

71. X. Geng *et al.*, “Comparison of oscillatory activity in subthalamic nucleus in Parkinson’s disease and dystonia,” *Neurobiol Dis*, vol. 98, pp. 100–107, 2017.

72. M. R. DeLong, “Primate models of movement disorders of basal ganglia origin,” *Trends Neurosci.*, vol. 13, no. 7, pp. 281–285, Jul. 1990.

73. R. L. Albin, A. B. Young, and J. B. Penney, “The functional anatomy of basal ganglia disorders,” *Trends Neurosci.*, vol. 12, no. 10, pp. 366–375, Jan. 1989.

74. J. Realmuto, J. S. L. Vidmark, and T. D. Sanger, “Modeling deep brain stimulation evoked

responses with phase oscillator networks (accepted)," in *IEEE EMBS International Conference on Neural Engineering (NER)*, 2023.

75. A. M. Lozano *et al.*, "Deep brain stimulation: current challenges and future directions," *Nat. Rev. Neurol.*, vol. 15, no. 3, pp. 148–160, Mar. 2019.

76. C. Wiest *et al.*, "Local field potential activity dynamics in response to deep brain stimulation of the subthalamic nucleus in Parkinson's disease," *Neurobiol. Dis.*, vol. 143, no. May, 2020.

77. W. Meissner *et al.*, "Subthalamic high frequency stimulation resets subthalamic firing and reduces abnormal oscillations," *Brain*, vol. 128, no. 10, pp. 2372–2382, 2005.

78. T. Hashimoto, C. M. Elder, M. S. Okun, S. K. Patrick, and J. L. Vitek, "Stimulation of the subthalamic nucleus changes the firing pattern of pallidal neurons," *J. Neurosci.*, vol. 23, no. 5, pp. 1916–1923, 2003.

79. G. Foffani and A. Priori, "Deep brain stimulation in Parkinson's disease can mimic the 300 Hz subthalamic rhythm," *Brain*, vol. 129, no. 12, 2006.

80. Y. Kuramoto, *Chemical Oscillations, Waves, and Turbulence*. New York, NY: Springer-Verlag, 1984.

81. S. H. Strogatz and R. E. Mirollo, "Stability of incoherence in a population of coupled oscillators," *J. Stat. Phys.*, vol. 63, no. 3–4, pp. 613–635, 1991.

82. E. Montbrió and D. Pazó, "Kuramoto Model for Excitation-Inhibition-Based Oscillations," *Phys. Rev. Lett.*, vol. 120, no. 24, p. 244101, 2018.

83. A. Franci, A. Chaillet, E. Panteley, and F. Lamnabhi-Lagarrigue, "Desynchronization and

inhibition of Kuramoto oscillators by scalar mean-field feedback," *Math. Control. Signals, Syst.*, vol. 24, no. 1, pp. 169–217, 2012.

84. G. Weerasinghe, B. Duchet, H. Cagnan, P. Brown, C. Bick, and R. Bogacz, "Predicting the effects of deep brain stimulation using a reduced coupled oscillator model," *PLoS Comput. Biol.*, vol. 15, no. 8, pp. e1006575–e1006575, Aug. 2019.

85. T. Menara, G. Baggio, D. Bassett, and F. Pasqualetti, "Functional control of oscillator networks," *Nat. Commun. 2022 131*, vol. 13, no. 1, pp. 1–13, Aug. 2022.

86. H. Hong and S. H. Strogatz, "Kuramoto model of coupled oscillators with positive and negative coupling parameters: An example of conformist and contrarian oscillators," *Phys. Rev. Lett.*, vol. 106, no. 5, pp. 1–4, 2011.

87. E. Fengler, J. F. Totz, P. Kaluza, and H. Engel, "Directed adaptation of synchronization levels in oscillator communities," *Chaos An Interdiscip. J. Nonlinear Sci.*, vol. 29, no. 6, p. 063101, Jun. 2019.

88. C. R. Laing, "The dynamics of chimera states in heterogeneous Kuramoto networks," *Phys. D Nonlinear Phenom.*, vol. 238, no. 16, pp. 1569–1588, Aug. 2009.

89. M. Berndt, Y. Li, G. Gora-Stahlberg, A. Jochim, and B. Haslinger, "Impaired white matter integrity between premotor cortex and basal ganglia in writer's cramp," *Brain Behav.*, vol. 8, 2018.

90. L. Bonilha *et al.*, "Structural white matter abnormalities in patients with idiopathic dystonia," *Mov. Disord.*, vol. 22, no. 8, pp. 1110–1116, Jun. 2007.

91. J. C. Timpe, K. C. Rowe, J. Matsui, V. A. Magnotta, and N. L. Denburg, "White matter integrity,

as measured by diffusion tensor imaging, distinguishes between impaired and unimpaired older adult decision-makers: A preliminary investigation," *J. Cogn. Psychol.*, vol. 23, no. 6, pp. 760–767, Sep. 2011.

92. S. M. Smith *et al.*, "Advances in functional and structural MR image analysis and implementation as FSL," *Neuroimage*, vol. 23 Suppl 1, no. SUPPL. 1, 2004.

93. J. L. R. Andersson, S. Skare, and J. Ashburner, "How to correct susceptibility distortions in spin-echo echo-planar images: Application to diffusion tensor imaging," *Neuroimage*, vol. 20, no. 2, pp. 870–888, 2003.

94. M. S. Graham, I. Drobnjak, M. Jenkinson, and H. Zhang, "Quantitative assessment of the susceptibility artefact and its interaction with motion in diffusion MRI," *PLoS One*, vol. 12, no. 10, 2017.

95. K. O'Brien *et al.*, "3-D residual eddy current field characterisation: applied to diffusion weighted magnetic resonance imaging," *IEEE Trans. Med. Imaging*, vol. 32, no. 8, pp. 1515–1525, 2013.

96. S. Ewert *et al.*, "Toward defining deep brain stimulation targets in MNI space: A subcortical atlas based on multimodal MRI, histology and structural connectivity," *Neuroimage*, vol. 170, pp. 271–282, Apr. 2018.

97. D. R. Ney, D. G. Heath, F. M. Corl, K. M. Horton, P. T. Johnson, and E. K. Fishman, "Volume Rendering versus Maximum Intensity Projection in CT Angiography: What Works Best, When, and Why.," *Radio Graph.*, vol. 26, 2006.

98. S. Karimi, P. Cosman, C. Wald, and H. Martz, "Segmentation of artifacts and anatomy in CT

metal artifact reduction," *Med. Phys.*, vol. 39, no. 10, pp. 5857–5868, 2012.

99. T. A. G. M. Huisman, "Diffusion-weighted and diffusion tensor imaging of the brain, made easy," *Cancer Imaging*, vol. 10, no. 1A, p. S163, 2010.

100. F. C. Yeh, V. J. Wedeen, and W. Y. I. Tseng, "Generalized q-sampling imaging," *IEEE Trans. Med. Imaging*, vol. 29, no. 9, pp. 1626–1635, Sep. 2010.

101. Z. T. Kincses *et al.*, "Target identification for stereotactic thalamotomy using diffusion tractography," *PLoS One*, vol. 7, no. 1, Jan. 2012.

102. F. C. Yeh, T. D. Verstynen, Y. Wang, J. C. Fernández-Miranda, and W. Y. I. Tseng, "Deterministic diffusion fiber tracking improved by quantitative anisotropy," *PLoS One*, vol. 8, no. 11, 2013.

103. C. G. Favilla, D. Ullman, A. Wagle Shukla, K. D. Foote, C. E. Jacobson, and M. S. Okun, "Worsening essential tremor following deep brain stimulation: Disease progression versus tolerance," *Brain*, vol. 135, no. 5, pp. 1455–1462, 2012.

104. L. C. Shih, K. LaFaver, C. Lim, E. Papavassiliou, and D. Tarsy, "Loss of benefit in VIM thalamic deep brain stimulation (DBS) for essential tremor(ET): How prevalent is it?," *Park. Relat. Disord.*, vol. 19, no. 7, pp. 676–679, 2013.

105. W. Byne *et al.*, "Magnetic Resonance Imaging of the Thalamic Mediodorsal Nucleus and Pulvinar in Schizophrenia and Schizotypal Personality Disorder," *Arch. Gen. Psychiatry*, vol. 58, no. 2, pp. 133–140, 2001.

106. C. R. Traynor, G. J. Barker, W. R. Crum, S. C. R. Williams, and M. P. Richardson, "Segmentation of the thalamus in MRI based on T1 and T2," *Neuroimage*, vol. 56, no. 3, pp. 939–950, 2011.

107. T. Gringel, W. Schulz-Schaeffer, E. Elolf, A. Frölich, P. Dechent, and G. Helms, “Optimized high-resolution mapping of magnetization transfer (MT) at 3 Tesla for direct visualization of substructures of the human thalamus in clinically feasible measurement time,” *J. Magn. Reson. Imaging*, vol. 29, no. 6, pp. 1285–1292, 2009.

108. N. K. K. King *et al.*, “Microelectrode recording findings within the tractography-defined ventral intermediate nucleus,” *J. Neurosurg.*, vol. 126, no. 5, pp. 1669–1675, 2017.

109. Y. Yovel and Y. Assaf, “Virtual definition of neuronal tissue by cluster analysis of multi-parametric imaging (virtual-dot-com imaging),” *Neuroimage*, vol. 35, no. 1, pp. 58–69, 2007.

110. N. D. DiProspero, S. Kim, and M. A. Yassa, “Magnetic resonance imaging biomarkers for cognitive decline in Down syndrome,” *Neurobiol. Aging Alzheimer Dis. Down Syndr.*, pp. 149–172, Jan. 2022.

111. S. S. Goldstein and W. Rall, “Changes of Action Potential Shape and Velocity for Changing Core Conductor Geometry,” *Biophys. J.*, vol. 14, no. 10, pp. 731–757, 1974.